Investigation of Magnetic Fields in a Cluster of Galaxies based on the Centimeter Wave Polarimetry

Takeaki Ozawa

Graduate School of Science & Engineering,
School of Natural Science,
Kagoshima University

A Dissertation submitted to the
Graduate School of Science and Engineering,
Kagoshima University for the degree of
Doctor of Philosophy (PhD),
March, 2016

Abstract

This thesis mainly aims at investigating the nature of cluster magnetic fields using the centimeter wave polarimetry. Cluster magnetic fields play an important role in a cluster of galaxies. They connect cosmic-ray particles with the intracluster medium, and convert the gravitational energy of cluster merger into the kinetic energy of the cosmic-ray particles. Accelerated cosmic-ray particles within the cluster magnetic fields carry out synchrotron emission, called diffuse and extended radio emission, in the whole region of the cluster. Hence, cluster magnetic fields is a key to understanding the physical process of cluster merger. Depolarization and Faraday tomography are very useful techniques, which enabled us to measure the structure of cluster magnetic fields along the line of sight. In order to reveal the magnetic field structures of a merging cluster of galaxies, we carried out the multiple frequency polarimetry of the merging cluster Abell 2256 and analyses with both techniques. The observations were carried out with the Karl G. Jansky very large array at S band (2051–3947 MHz) and X band (8051–9947 MHz) in the C array configuration. We detected significant polarized radio emission from the radio relic, Source A, and Source B in Abell 2256. The fractional polarization of the radio relic decreases from $\sim$ 35 to $\sim$ 20 % around 3 GHz as the frequency decreases, and remains $\sim$20 % between 1.37 and 3 GHz. Since the fractional polarization observed with the Westerbork synthesis radio telescope indicates a value less than 1 % at 0.3 GHz, we found that the radio relic has a step-like variation of the fractional polarization. We analyzed the step-like variation with the depolarization models and Faraday tomography. Both analyses suggest two depolarization components and existence of turbulent magnetic fields along the line of sight toward the radio relic. We concluded that the two depolarization components would be the radio relic component, and the intracluster space or Milky Way galaxy component, respectively. We also calculated the equipartition magnetic field strengths toward the radio relic, which is 1.8–5.0 μG. With the standard deviation of the rotation measure, the magnetic field strengths toward Source A and Source B are estimated to be 0.63–1.26 μG and 0.11–0.21 μG, respectively.

Contents

List of Figures

List of Tables

1. Introduction

Clusters of galaxies are the largest gravitational boundary systems among the hierarchical structures in the Universe. They include several hundreds member galaxies, and the typical diameter[1] and dynamical mass are several Mpc and $\sim 10^{15}$ M_{sun}, respectively. Clusters of galaxies mainly consist of three components, member galaxies, diffuse hot gas, and dark matter. The diffuse hot gas, called intracluster medium (ICM), consists of particles which have the energy of $\sim 10^7$ K with the density of $n_e \sim 10^{-3}$ cm^{-3}, and emits X-ray through the thermal bremsstrahlung. The mass occupancy of each component is estimated to be ∼3–5 %, ∼15–17 %, and ∼80 %, respectively (Feretti et al., 2012).

Clusters of galaxies would evolve through cluster mergers, which are the most energetic events ($\sim 10^{64}$ ergs) in the Universe since the Big Bang (Sarazin, 2002). The gravitational energy is converted into the energies of the shock wave, turbulence, and heating of the ICM (Govoni & Feretti, 2004). Cosmic-ray particles injected into the ICM from active galactic nuclei (AGN) activities, star formations of galaxies, and structure formations (Brunetti et al., 2001) can be re-accelerated by the shock wave (Takizawa & Naito, 2000; Vazza et al., 2009) and turbulence (Brunetti et al., 2001; Petrosian, 2001; Brunetti et al., 2004; Ohno et al., 2002; Fujita et al., 2003; Cassano & Brunetti, 2005; Donnert et al., 2013). The relativistic cosmic-ray electrons re-accelerated by merger events and magnetic fields in the ICM are the origin of diffuse and extended radio emission detected in clusters.

In this chapter, we will firstly introduce the general properties of diffuse and extended radio emission detected in clusters of galaxies, which is an evidence of the existence of large scale magnetic fields in clusters of galaxies. Secondary, we will summarize the theoretical background for the cluster magnetic fields, and review the knowledge of cluster magnetic fields. Lastly, we will introduce the aim of this thesis.

1.1. Diffuse and Extended Radio Emission

At the centimeter and meter wave radio observations of clusters of galaxies, we often detect diffuse and extended radio emission, which has a scale of several hundreds kpc to a few Mpc. Large et al. (1959) found the diffuse radio emission in Coma cluster for the first time, and Willson (1970) found that the diffuse radio emission in Coma cluster was not associated with any member galaxies. Thanks to the high sensitivity radio observations,

[1] Abell et al. (1989) defined typical radius $1.5h^{-1}$Mpc, called Abell radius. Most of clusters contain the member galaxies of 70% within the Abell radius.

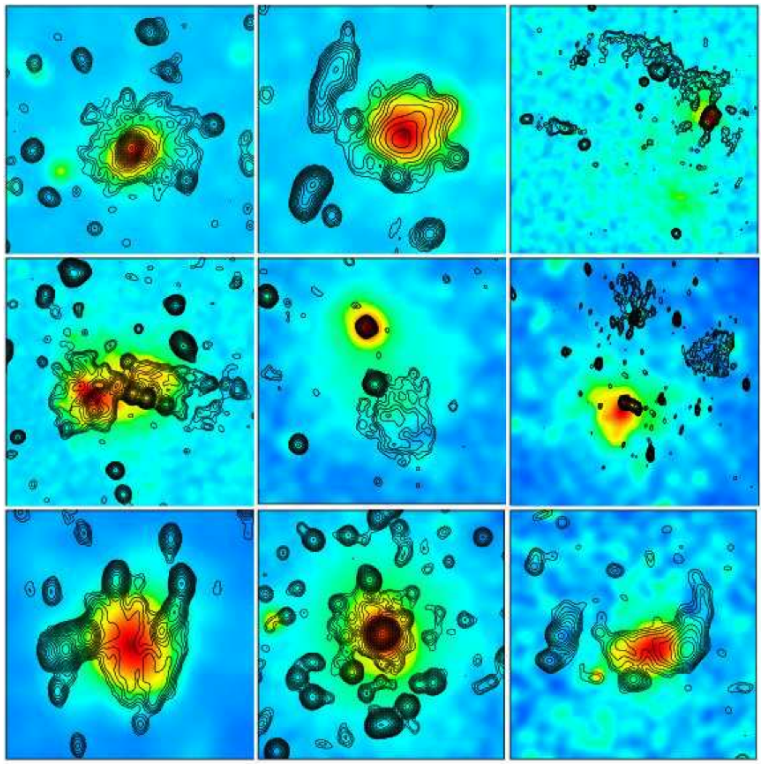

Figure 1: Sample images of the radio halo, radio relic, and radio mini-halo (from Feretti et al., 2012). Contours and colors represent the radio emission and X-ray emission, respectively. *Top left*: Abell 2219 (halo). *Top center*: Abell 2744 (halo + relic). *Top right*: Abell 115 (relic). *Middle left*: Abell 754 (complex, halo + relic). *Middle center*: Abell 1664 (relic). *Middle right*: Abell 548b (relic). *Bottom left*: Abell 520 (halo). *Bottom center*: Abell 2029 (mini-halo). *Bottom right*: RXCJ1314.4-2515 (halo + double relics).

over 100 diffuse radio emission are detected as of 2011, and are associated with the ICMs (Feretti et al., 2012). The spectral energy distribution (SED) of diffuse radio emission indicates the synchrotron radio emission (e.g. Vacca et al., 2014), and suggests the existence of cluster magnetic fields (~ 0.1–$1\ \mu$G) and relativistic cosmic-ray electrons (Lorentz factor $\gamma \gg 1000$) within the whole region of the cluster (Ferrari et al., 2008). Since diffuse radio emission is imprinted in the nature of magnetic fields and cosmic-ray electrons in clusters of galaxies, most of what we know about cluster magnetic fields are obtained from the studies of diffuse radio emission and Faraday rotation measure (Govoni et al., 2013).

Diffuse radio emission is classified into three types, radio halo, radio relic, and radio

mini-halo, according to their locations and the type of the host cluster (see Figure 1). Feretti et al. (2012) anticipated that radio halos are hosted in merging clusters and located in the cluster center, radio relics are hosted in merging and relaxed clusters and located in the cluster out skirts, and radio mini-halos are hosted in relaxed cool-core clusters and located in the cluster center. In the following sections, we will introduce the details of the radio halo, radio relic, and radio mini-halo, respectively.

1.1.1. Radio Halo

Radio halos are diffuse and extended radio emissions located in the cluster center of merging clusters. The size of the emitting region is over Mpc. The surface brightness is too low ($\sim$ μJy arcsec^{-2} at 1.4 GHz), and is not polarized probably due to the depolarization. The spectral index of radio halos show a steep spectral index ($\alpha > 1$). As of 2011, 42 radio halos have been detected (Feretti et al., 2012).

The spectral index of radio halos is very important because it reflects the energy distribution of the cosmic-ray electrons and magnetic field strengths in the ICM. As of 2011, the spectral index of the radio halos has been measured in 22 clusters, but most of the spectral index were measured with the flux density only at two frequencies due to the low surface brightness of radio halos (Feretti et al., 2012).

The spatial distribution of the spectral index of the radio halo is measured in some clusters. The first spectral distribution was created in Coma cluster, indicating radial spectral index steepening from the cluster center to the peripheral region (Giovannini et al., 1993). Feretti et al. (2004) found that the radial steepening also exists in the undisturbed halo region in Abell 665 and 2163 (see Figure 2). Orrú et al. (2007) reported that the spectral indexes of Abell 2744 and Abell 2219 do not show radial steepening, but have the patchy structure of the spectral index distribution. In Abell 2744, they also found that the regions where the spectral index is flattened tend to have the high temperature ICM. Feretti et al. (2012) reported that the clusters which have the high-temperature ICM show the flattened spectral index, whereas the clusters which have the low-temperature ICM show the steepened spectral index. This tendency would be the evidence that the cluster merger induce the radio halo, and the energy of the cluster merger would be converted into the radiative cosmic-ray electrons and cluster magnetic fields.

The steep spectral index suggests that the cosmic-ray electrons were injected energies in the past. The radiative cosmic-ray electrons are affected by the energy losses from the synchrotron emission, inverse Compton scattering (interaction between the electron and cosmic microwave background (CMB) photons), and Coulomb loss (interaction between

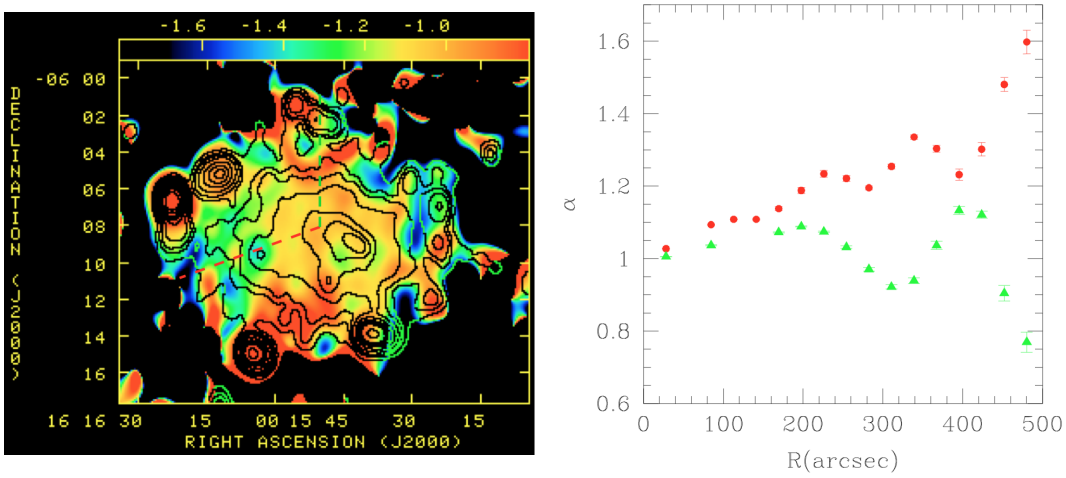

Figure 2: Spectral index distribution and radial profiles of the radio halo in Abell 2163 (from Feretti et al., 2004). *Left panel*: the spectral index distribution of the radio halo in Abell 2163. Color represents the spectral index, calculated from the surface brightness between 0.3 and 1.4 GHz. Contours are drawn at 0.2, 0.5, 0.8, 1.5, 3.0, 5.0, 7.0, 9.0, 15.0, 25.0 mJy beam^{-1}. The telescope beam size is $60'' \times 45''$. *Right panel*: the radial profiles of the spectral index along the two directions drawn in the left panel. Red points represent the spectral index toward the southeast (red dashed line). Green points represent the spectral index toward the north (green dashed line).

the electron and ICM). The main loss process is the synchrotron emission and inverse Compton scattering (Ferrari et al., 2008). The radiative lifetime of a relativistic cosmic-ray electron with a Lorentz factor $\gamma < 10^8$ is given by

$$\tau \sim 2 \times 10^{12} \gamma^{-1} \left[(1+z)^4 + \left(\frac{B}{3.3_{[\mu\mathrm{G}]}} \right)^2 \right]^{-1} \quad [\mathrm{years}], \tag{1}$$

where τ is the radiative lifetime, γ is the Lorentz factor, and z is the red shift, respectively (Meisenheimer et al., 1989; Ferrari et al., 2008). Hence, the radiative lifetime is in the order of $\sim 10^8$ years. Since the expected diffusive velocity of the cosmic-ray electrons is ~ 100 km s^{-1} (Alfvén Speed), the radiative cosmic-ray electrons cannot diffuse over the Mpc scale within the electron lifetime. Therefore, the radiative cosmic-ray electrons are not produced by individual sources such as AGN activities in clusters. As for the acceleration process of the radiative cosmic-ray electrons, two hypotheses, primary and

secondary models, are proposed. We will introduce the cosmic-ray acceleration processes in Section 1.1.4.

1.1.2. Radio Relic

Radio relics are diffuse and extended radio emissions located in the peripheral region of merging and relaxed clusters. The size of the emitting region is over the Mpc scale. The surface brightness is low, and is polarized strongly ($\sim$ 30 %). The spectral index of radio relics shows a steep spectral index ($\alpha > 1$). Radio relics are classified into two types, elongated and roundish relics, from its structure. As of 2011, 50 radio relics have been detected, which are made up of 35 elongated relics and 15 roundish relics (Feretti et al., 2012).

Elongated relics have a narrow structure, and the major axis is roughly directed toward the direction perpendicular to the radial direction of the cluster (e.g. CIZAJ2242.8+5301, van Weeren et al., 2010). They are highly polarized, and show the different radio profiles between the inner edge and outer edge region (see Figure 3). In some clusters, the double relics (two elongated relics which have a point symmetry structure) are detected (e.g. Abell 3667, Abell 3376, CIZAJ2242.8+5301, Roettiger et al., 1999; Bagchi et al., 2006; van Weeren et al., 2010).

Roundish relics have a roundish structure, and are detected off-center in the clusters (e.g. Abell 1664, Govoni et al., 2001). They consist of diffuse components and filamentary structures (e.g. Abell 2256, Owen et al., 2014).

As for the interpretation of roundish relics, two hypotheses are proposed. On the one hand, roundish relics are interpreted as elongated relics affected by the projection effect. In the cosmological magnetohydrodynamic (MHD) simulation performed by Skillman et al. (2013), the viewing angle of the cluster may have significant impact on the classification of the radio relic, and it seems that the roundish like emission is produced by the projection effect. On the other hand, roundish relics are interpreted as old radio lobes originated from previous AGN activities (Feretti et al., 2012) because, in some cases, roundish relics are located near the First Ranked Galaxy (FRG), and FRG is usually a cD galaxy (Giovannini & Feretti, 2004). AGN activity could inject the energy into roundish relics within a short time period.

The spectral index of radio relics are very important as with that of radio halos because it refracts the energy distribution of the cosmic-ray electrons and magnetic fields strengths in the relic region. As of 2011, the spectral index of radio relics have been measured in 38 clusters (Feretti et al., 2012). In contrast to spectral indexes of radio halos, the spectral indexes of radio relics are measured in multiple frequencies

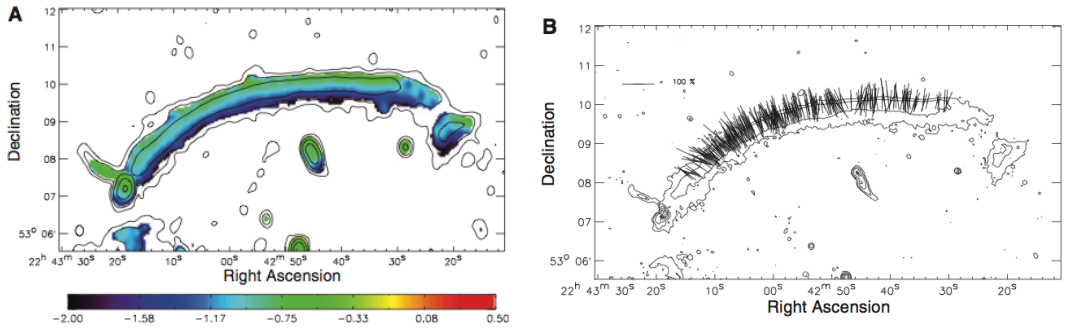

Figure 3: Spectral index distribution and polarization vector maps of the radio relic in CIZA J2242.8+5301 (from van Weeren et al., 2010). *Left panel*: The spectral index distribution obtained with the VLA at 2.3, 1.7, 1.4, 1.2, and 0.61 GHz. Contours are obtained with GMRT at 1.4 GHz, and drawn at 1, 4, 16, ... × 36 μJy. Colors represent the value of the spectral index. *Right panel*: The polarization vector maps obtained with the VLA at 4.9 GHz. Contours are obtained with the GMRT at 610 MHz, and drawn at 1, 4, 16, ... × 70 μJy. The length of the polarization vector is proportional to the fractional polarization.

because radio relics are slightly brighter than radio halos.

The typical spectral indexes of elongated and roundish radio relics are $\alpha = 1 - 1.6$ and $\alpha = 1.1 - 2.9$, respectively. Feretti et al. (2012) reported that radio relics have a correlation between the spectral index and projected distance from the cluster center. The radio relics with short distance and long distance have steep and flat spectral indexes, respectively. The correlation between the spectral index and radio power of radio relics was also reported. The roundish relics with low radio power and high radio power show the steep and flat spectral indexes, respectively. They argued that the correlations reflect the hypothesis that the roundish relic is produced by the AGN activity.

The spectral index distribution of radio relics is unique. It is measured in both elongated and roundish relics. In figure 3, we show the spectral index distribution of the elongated radio relic in CIZA J2242.8+5301. The cluster center exists toward the south direction from the radio relic. This radio relic shows the steepness of the spectral index between the inner edge and outer edge region. Same spectral index distribution of radio relics are reported in 1RXS J0603.3+4214 (van Weeren et al., 2012). van Weeren et al. (2011) reported that simulated radio relics can create such a spectral index distribution, and cosmic-ray electrons are re-accelerated by the shock wave associated with the cluster

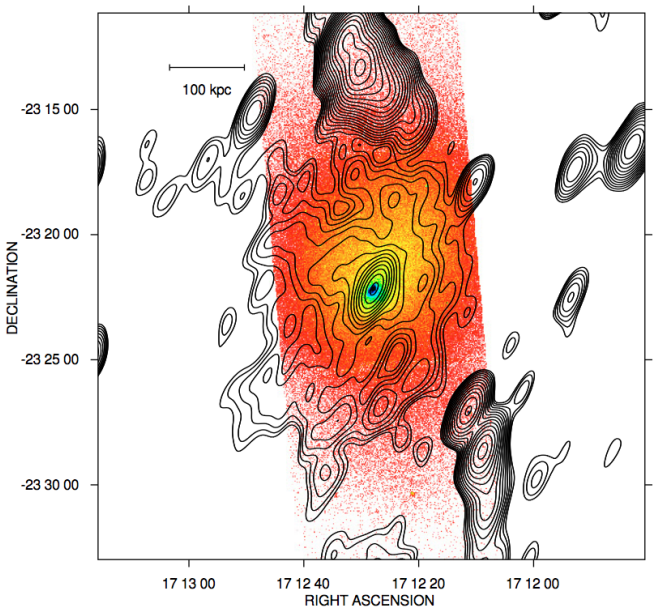

Figure 4: Mini-halo in Ophiuchus cluster obtained with the VLA 1.4 GHz (contours) overlaid on the Chandra X-ray image in the 0.5–4 kev band (from Govoni et al., 2009).

merger. The spectral index of the roundish radio relic is measured only in Abell 2256 (Clarke & Ensslin, 2006; Feretti et al., 2012), and the relic shows a steepening from the northwest to southeast.

1.1.3. Radio Mini-Halo

Radio mini-halos are diffuse and extended radio emissions located in the center of relaxed and cool-core clusters. The size of the emitting region of mini-halos is several hundreds kpc. We show a sample image of a mini-halo in figure 4. As of 2011, 11 mini-halos are detected (Feretti et al., 2012).

The origin of mini-halos are magnetic fields and relativistic cosmic-ray electrons, which are considered to be mixed with the ICM. This consideration is used to divide the mini-halo and synchrotron emission associated with AGN activities in the cluster. The AGN activities create the synchrotron emission with the hole in the X-ray emission of the ICM (e.g. A2052, Blanton et al., 2011). In this case, the synchrotron emission is not defined as the mini-halo. In addition, the combination of a mini-halo and the emission of radio galaxies in the cluster center make it difficult to classify mini-halos (Feretti et al., 2012).

The origin of the radiative cosmic-ray electrons in mini-halos are poorly understood. Gitti et al. (2002) proposed that the radiative cosmic-ray electrons are re-accelerated by the MHD turbulence in the ICM of the cool-core region. Ferrari et al. (2011) argued that minor merger, which does not destroy the cool-core, provides the energy for the re-acceleration of the cosmic-ray electrons. Indeed, the peculiar X-ray features in the cluster center of Abell 2029, Abell 1835, and Ophiuchus cluster are found with the mini-halos, indicating the relation between mini-halos and minor merger (Govoni et al., 2009).

1.1.4. Acceleration Processes of the Radiative Cosmic-ray Electrons

Radio halos suggest that radiative cosmic-ray electrons must be re-accelerated in the whole region of a cluster at the same time. As a solution, two cosmic-ray acceleration models, primary and secondary models, are proposed.

primary electron model In the primary electron model, cosmic-ray electrons, injected by AGN activities, star formation of galaxies, and structure formation (Govoni & Feretti, 2004), are re-accelerated by the shock wave (Takizawa & Naito, 2000; Vazza et al., 2009) and turbulence (Brunetti et al., 2001; Petrosian, 2001; Brunetti et al., 2004; Ohno et al., 2002; Fujita et al., 2003; Cassano & Brunetti, 2005; Donnert et al., 2013) associated with cluster mergers. Recently, cosmological MHD simulations show that cluster mergers induce the turbulence in the ICM over the Mpc scale, and the energy of the ICM is converted into the energy of the cosmic-ray electrons through the Fermi-II process or MHD wave (Brunetti et al., 2001; Petrosian, 2001; Fujita et al., 2003; Cassano & Brunetti, 2005; Brunetti et al., 2004; Xu et al., 2009, 2010; Feretti et al., 2012). Then, cosmic-ray electrons can be re-accelerated at the same time. In this case, we can predict that radio halos induced by the primary cosmic-ray electrons within magnetic fields relate to cluster mergers. Actually, Brunetti et al. (2009) reported that the power of the radio halo and X-ray luminosity of the ICM have a correlation (see Figure 5), and this would be an evidence of the relation between radio halos and cluster mergers.

Shocks associated with cluster mergers can also re-accelerate cosmic-ray electrons in clusters. Simulated radio relic associated with the cluster merger show the radio properties corresponding to the observed radio relic (van Weeren et al., 2011).

secondary electron model In the secondary model, radiative cosmic-ray electrons are produced by inelastic nuclear collision between cosmic-ray protons and nuclei of the ICM (Dennison, 1980; Blasi & Colafrancesco, 1999; Dolag & Enßlin, 2000; Keshet & Loeb,

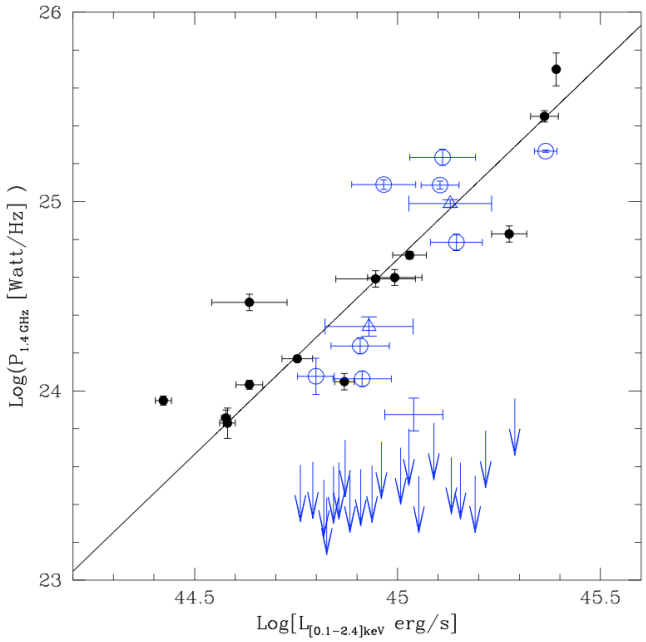

Figure 5: The distribution of the radio halos in the $P_{1.4} - L_X$ plane (from Brunetti et al., 2009). Blue and black circle marks represent the giant radio halos. Arrow marks represent upper limits for GMRT clusters with no evidence of the radio halo. The solid line represents the best fit to the distribution of the giant radio halos.

2010; Feretti et al., 2012). A cosmic-ray proton hardly losses its energy because the mass of a proton is heavier than that of an electron. If cosmic-ray protons are injected by individual sources in clusters, the cosmic-ray protons can diffuse over the Mpc scale. Hence, the cosmic-ray protons can continuously produce cosmic-ray electrons in the whole region of the cluster. Since the density of the ICM at the peripheral region of clusters is low, the origin of radiative cosmic-ray electrons of radio relics does not agree with the secondary model. If cosmic-ray electrons produced by the secondary model are the origin of radio halos, the spectral index of the synchrotron emission should be independent of the cluster location, and the value of the spectral index is predicted as $\alpha < 1.5$ (Brunetti, 2004). Since the secondary model does not relate to cluster mergers, radio halos should not be related to the cluster merger. However, the correlation between radio halos and cluster mergers (X-ray luminosity of the ICM) have been found (Brunetti et al., 2009). In addition, nuclear collision also produce γ-ray emission, but the γ-ray emission produced by secondary model have not been detected (Ackermann et al., 2014).

1.2. Theoretical Background for the Cluster Magnetic Fields

We will summarize the theoretical background for cluster magnetic fields. Synchrotron emission is a key to know the magnetic fields in clusters of galaxies. We firstly introduce the property of the synchrotron emission. After that, we will introduce the measuring methods of the magnetic fields: equipartition formula, Faraday rotation measure, interpretation of the cluster rotation measure, depolarization, and Faraday tomography. In order to understand the measuring methods of the magnetic fields, we must understand the polarization and Stokes parameter, and we therefore describe the details of polarization and Stokes parameters in Appendix A.1 and A.2, respectively.

1.2.1. Synchrotron Emission

Synchrotron emission is electromagnetic waves produced by relativistic cosmic-ray electrons within magnetic fields, and is linear polarized perpendicular to the ordered magnetic fields without Faraday rotation. If we consider an electron of energy $E = \gamma m_{\rm e} c^2$ (where $\gamma \equiv \left[1 - (v^2/c^2)\right]^{-1/2}$ is the Lorentz factor) and magnetic fields $\mathbf{B}$, the electron within the magnetic fields performing uniform linear motion parallel to the magnetic fields while rotating around magnetic fields due to Lorentz force of $-e/c\ \mathbf{v}_{\rm e} \times \mathbf{B}$ emits the radio wave into a cone of half angle $\sim \gamma^{-1}$ toward the $\mathbf{E} = \mathbf{v}_{\rm e} \times \mathbf{B}$. Then, the observed radio wave is pulse train since the emitted radio wave is affected by the beaming effect, and the rotating frequency of the electron $\nu_{\rm s}$, called cyclotron frequency, and the pulse interval τ are given by

$$\nu_{\rm s} = \frac{eB \sin\theta}{2\pi\gamma m_{\rm e} c}, \tag{2}$$

and

$$\tau = \frac{1}{\nu_{\rm s}} = \frac{2\pi\gamma m_{\rm e} c}{eB \sin\theta}, \tag{3}$$

respectively, where e is the elementary charge, m_e is the electron mass, c is the speed of light, and θ is the pitch angle between the electron velocity and the magnetic field direction, respectively. Dividing the angular width of the beam $2\gamma^{-1}$ by the angular velocity of the electron $2\pi\nu_{\rm s}$, the pulse width Δt is given by

$$\Delta t = \frac{2\gamma^{-1}}{2\pi\nu_{\rm s}} = \frac{1}{\pi\gamma\nu_{\rm s}}. \tag{4}$$

However, since the electron emitting the radio wave toward the observer is moving toward the observer, the distance from the electron to the observer is varied. The difference

between the shortest and longest distance Δs is given by

$$\Delta s \sim v_{\rm e}\Delta t = \frac{v_{\rm e}}{\pi\gamma\nu_{\rm s}}, \tag{5}$$

where $v_{\rm e}$ is the rotation velocity of the electron. The observed pulse width $\Delta t'$ is shorter than Δt by $\Delta t_{\rm s} = \Delta {\rm s}/c$, and is given by

$$\begin{aligned}
\Delta t' &= \Delta t - \Delta t_{\rm s} \\
&= \frac{1}{\pi\gamma\nu_{\rm s}} - \frac{\left(\frac{v_{\rm e}}{\pi\gamma\nu_{\rm s}}\right)}{c} \\
&= \frac{1}{\pi\gamma\nu_{\rm s}}\left(1 - \frac{v_{\rm e}}{c}\right) \\
&= \frac{1}{2\pi\nu_{\rm s}\gamma^3},
\end{aligned} \tag{6}$$

where we took into account $1 - (v/c) = 1/2\gamma^2$ from $\gamma \gg 1$. Substituting equation (2) into equation (6) gives

$$\Delta t' \sim \frac{m_{\rm e}c}{eB\sin\theta\gamma^2}. \tag{7}$$

The power spectrum of the synchrotron emission with a relativistic electron is obtained from Fourier transformation of equation (7) as

$$P(\nu) = \frac{\sqrt{3}e^3 B\sin\theta}{m_{\rm e}c^2}\left(\frac{\nu}{\nu_{\rm c}}\right)\int_{\nu/\nu_{\rm c}}^{\infty} K_{5/3}(\xi)d\xi, \tag{8}$$

where $K_{5/3}$ is the modified Bessel function. The synchrotron critical density $\nu_{\rm c}$ is defined as

$$\nu_{\rm c} \equiv c_1(B\sin\theta)E^2, \tag{9}$$

where c_1 is

$$c_1 = \frac{3e}{4\pi m_{\rm e}^3 c^5}. \tag{10}$$

Note that, the peak of the intensity of the synchrotron emission with an electron is at $0.29\nu_{\rm c}$.

Usually, many relativistic electrons within magnetic fields emit the synchrotron emission from radio sources. The energy spectrum of the electrons in a unit volume is empirically expressed as

$$N(E)dE = CE^{-p_e}dE \tag{11}$$

or

$$N(\gamma)d\gamma = C\gamma^{-p_e}d\gamma, \tag{12}$$

where $N(E)$ and $N(\gamma)$ are the number of electrons in the energy range between E_1 and E_2 and between γ_1 and γ_2, respectively, p_e is the spectral index of the energy spectrum of cosmic-ray electrons, and C is the constant, respectively. Here, we rewrite the equation (8) as

$$P(\nu) = \frac{\sqrt{3}e^3 B\sin\theta}{m_{\rm e}c^2}F(\nu/\nu_{\rm c}), \tag{13}$$

where we do not know what the function $F(\nu/\nu_{\rm c})$ is. Then, the total power of the synchrotron emission $P_{\rm t}(\nu)$ is given by

$$\begin{aligned} P_{\rm t}(\nu) &= C\int_{\gamma_1}^{\gamma_2} P(\nu)\gamma^{-p_e}d\gamma \\ &= C(B\sin\theta)\int_{\gamma_1}^{\gamma_2} F\left(\frac{\nu}{\nu_{\rm c}}\right)\gamma^{-p_e}d\gamma. \end{aligned} \tag{14}$$

Changing variables of the integration to $x = \nu/\nu_c$, and $\nu_{\rm c} \propto \gamma^2$ gives

$$P_{\rm t}(\nu) \propto \nu^{-(p_e-1)/2}\int_{x_1}^{x_2} F(x)x^{(p_e-3)/2}dx. \tag{15}$$

The integration range x_1 and x_2 corresponds to the range of γ_1 and γ_2, and depends on the frequency ν. If we assume $x_1 = 0$ and $x_2 = \infty$, then we obtain

$$P_t(\nu) \propto \nu^{-(p_{\rm e}-1)/2} = \nu^{-\alpha}, \tag{16}$$

where $\alpha = (p_{\rm e}-1)/2$ is the spectral index of the energy spectrum of the synchrotron emission. Hence, the SED of the synchrotron emission is the power law spectrum.

1.2.2. Equipartition Magnetic Fields

We can estimate the magnetic field strengths from the luminosity of the synchrotron emission. Since we do not know the energy of the relativistic cosmic-ray electrons, we cannot know the true magnetic field strengths. Usually, an assumption that the total energy of a radio source takes a condition of minimum energy is used.

Total energy of the synchrotron emission $U_{\rm t}$ is written as

$$U_{\rm t} = U_{\rm B} + U_{\rm e} + U_{\rm p}, \tag{17}$$

where $U_{\rm B}$ is the energy of the magnetic fields, $U_{\rm e}$ is the energy of the relativistic cosmic-ray electrons, and $U_{\rm p}$ is the energy of the relativistic heavy cosmic-ray particles, respectively. The energy of the magnetic fields in the source volume V is given by

$$U_{\rm B} = \frac{B^2}{8\pi} V, \tag{18}$$

The energy of the relativistic electrons in the source volume V is given by

$$\begin{aligned} U_{\rm e} &= V \int_{E_1}^{E_2} N(E) E dE \\ &= V N_0 \int_{E_1}^{E_2} E^{-p_{\rm e}+1} dE. \end{aligned} \tag{19}$$

In order to obtain the luminosity of the synchrotron emission, we consider the total power of the synchrotron emission in the frequency range between ν and $\nu + d\nu$, expressed as

$$P_t(\nu) d\nu = -\frac{dE}{dt} N(E) dE, \tag{20}$$

where $-\frac{dE}{dt}$ is radiative energy loss of an electron, and integrating equation (8) in the entire frequency range gives

$$\begin{aligned} -\frac{dE}{dt} &= \int_0^\infty P(\nu) d\nu \\ &= \frac{\sqrt{3} e^3 B \sin\theta}{m_{\rm e} c^2} \int_0^\infty F\left(\frac{\nu}{\nu_{\rm c}}\right) d\nu \\ &= \frac{\sqrt{3} e^3 B \sin\theta}{m_{\rm e} c^2} \nu_{\rm c} \int_0^\infty F(x) dx \\ &= \frac{\sqrt{3} e^3 B \sin\theta}{m_{\rm e} c^2} \nu_{\rm c} \frac{8\pi}{9\sqrt{3}} \\ &= c_2 (B \sin\theta)^2 E^2, \end{aligned} \tag{21}$$

where c_2 is

$$c_2 = \frac{2e^4}{3 m_{\rm e}^4 c^7}. \tag{22}$$

Hence, the synchrotron luminosity L is given by

$$\begin{aligned} L &= V \int_{E_1}^{E_2} \left(-\frac{dE}{dt}\right) N(E) dE \\ &= c_2 (B \sin\theta)^2 V N_0 \int_{E_1}^{E_2} E^{-p_\mathrm{e}+2} dE. \end{aligned} \tag{23}$$

Eliminating VN_0 from equation (23) and rewriting E_1 and E_2 in terms of ν_1 and ν_2 using equation (9), the energy of the electrons U_e can be expressed as a function of the synchrotron emission as

$$\begin{aligned} U_\mathrm{e} &= c_2^{-1} c_1^{1/2} \tilde{C} L B^{-3/2} \\ &= c_{12} L B^{-3/2}, \end{aligned} \tag{24}$$

where we assumed $\sin\theta = 1$ and

$$\tilde{C} = \left(\frac{2\alpha - 2}{2\alpha - 1}\right) \frac{\nu_1^{(1-2\alpha)/2} - \nu_2^{(1-2\alpha)/2}}{\nu_1^{(1-\alpha)} - \nu_2^{(1-\alpha)}}. \tag{25}$$

The energy of the heavy particles U_p is considered to be related to the energy of the electrons as

$$U_\mathrm{p} = \mathcal{K} U_\mathrm{e}, \tag{26}$$

where $\mathcal{K}$ depends on the re-acceleration process of the electrons. As a result, the total energy is expressed as a function of the magnetic fields as

$$U_\mathrm{t} = (1 + \mathcal{K}) c_{12} L B^{-3/2} + \frac{B^2}{8\pi} V. \tag{27}$$

If we assume that the total energy of the radio source U_t takes the condition of minimum energy, then the relation of the energy between the magnetic fields and relativistic electrons is approximately equal to

$$U_\mathrm{B} = \frac{3}{4}(1 + \mathcal{K}) U_\mathrm{e}. \tag{28}$$

This relation is called classical equipartition assumption, and we can calculate the equipartition magnetic field strength:

$$B_\mathrm{eq} = (6\pi(1 + \mathcal{K}) c_{12} \frac{L}{V})^{2/7}. \tag{29}$$

(Govoni & Feretti, 2004; Ferrari et al., 2008).

In the classical minimum energy formula of equation (29), the luminosity of the synchrotron emission is based on the integration of the intensity between the two fixed frequencies ν_1 and ν_2 (Govoni & Feretti, 2004); usually, the integration interval of 10 MHz–10 GHz is used. From equation (24), the electron energy at ν_1 and ν_2 depend on the magnetic field strengths. In the fixed integration range of the frequencies, the integration range of the electron energies are variable, and Beck & Krause (2005) pointed out that the index of 2/7 in equation (29) should be replaced by $1/(3+\alpha)$.

Moreover, it is hard to know $\mathcal{K}$ which is the value of the ratio of the total energies of the cosmic-ray protons and electrons because the spectra of the cosmic-ray proton and electron have not been measured over the whole energy range. Instead of $\mathcal{K}$, Beck & Krause (2005) proposed to use the ratio of the number densities $\mathbf{K}$ of the cosmic-ray protons and electrons per particle energy interval within the energy range traced by the observed synchrotron emission. We can not only observe $\mathbf{K}$ near the sun directly, but also predict it because $\mathbf{K}$ is constant $\mathbf{K_0}$ in the particle energy range $E_\mathrm{p} < E < E_\mathrm{syn}$ (E_p is the proton rest energy and E_syn is the upper energy point where synchrotron or inverse Compton loss of the cosmic-ray electrons become dominant), and $\mathbf{K_0}$ depends only on the transition energies from the non-relativistic to the relativistic and the cosmic-ray particle injection spectral index. For more details of the revised equipartition formula, see Beck & Krause (2005).

The revised equipartition formula and the total magnetic field strength B_t is given by

$$B_\mathrm{t} = \left\{ \frac{4\pi(2\alpha+1)(\mathbf{K_0}+1) I_\nu E_\mathrm{p}^{1-2\alpha} (\nu/2c_1)^\alpha}{(2\alpha-1)c_2(\alpha) l c_4(i)} \right\}^{1/(\alpha+3)}, \tag{30}$$

where α is the synchrotron spectral index, $\mathbf{K_0}$ is the ratio of the number densities of the cosmic-ray protons and electrons, I_ν is the synchrotron intensity at frequency ν, E_p is the proton rest energy, and l is the path length. The c_1, c_2, c_3, and c_4 are written as

$$\begin{aligned}
c_1 &= \frac{3e}{4\pi m_\mathrm{e}^3 c^5} = 6.26428 \times 10^{18}\ [\mathrm{erg}^{-2}\ \mathrm{s}^{-1}\ \mathrm{G}^{-1}] \\
c_2 &= \frac{1}{4} c_3 \frac{(p_\mathrm{e}+7/3)}{(p_\mathrm{e}+1)} \Gamma\left[\frac{3p_\mathrm{e}-1}{12}\right] \Gamma\left[\frac{3p_\mathrm{e}+7}{12}\right] \\
c_3 &= \frac{\sqrt{3}e^3}{(4\pi m_\mathrm{e} c^2)} = 1.86558 \times 10^{-23}\ [\mathrm{erg}\ \mathrm{G}^{-1}\ \mathrm{sr}^{-1}] \\
c_4 &= [\cos(i)]^{(p_\mathrm{e}+1)/2},
\end{aligned}$$

where e is the elementary charge, m_e is the electron mass, c is the speed of light, p_e is

the spectral index of the energy spectrum, and i is the inclination of the magnetic fields with respect to the sky plane (Beck & Krause, 2005).

1.2.3. Faraday Rotation Measure

The linearly polarized radio emission propagating in magneto-ionic plasm (composed magnetic fields and thermal electrons) suffers the rotation of the polarization angle, called Faraday rotation. The variation of the polarization angle is given by

$$\chi = \chi_0 + \chi_{\rm F}, \tag{31}$$

where χ is the observed polarization angle, χ_0 is the intrinsic polarization angle, and $\chi_{\rm F}$ is the rotation angle due to Faraday rotation. The rotation angle is given by

$$\chi_{\rm F} = RM\lambda^2, \tag{32}$$

where RM is the rotation measure (RM) in rad m^{-2}, and λ is the wavelength in m. Furthermore, the RM is given by

$$\begin{aligned} RM &= \frac{e^3}{2\pi m_{\rm e}^2 c^4}\int_0^d n_{\rm e} B_{\parallel} dl \\ &\sim 812\int_0^d n_{\rm e} B_{\parallel} dl, \end{aligned} \tag{33}$$

where e is the elementary charge, $m_{\rm e}$ is the electron mass, c is the speed of light, $n_{\rm e}$ is the thermal electron density in cm^{-3}, $B_{\parallel}$ is the magnetic field strength parallel to the line of sight in μG, l is the path length in kpc, and d is the integration distance from observer to the polarized radio source. When the direction of the magnetic field is directed toward us, we obtain a positive value of the RM. If we put a suitable electron density into equation (33) from observations or models, we can infer the averaged value of the magnetic field strengths parallel to the line of sight (Burn, 1966; Sofue et al., 1986; Widrow, 2002).

In order to measure RMs, we have to observe polarization angles of a target source at least two frequencies. If we observe the polarization angles of χ_1 with wavelength of λ_1 and χ_2 with λ_2, the RM is given by

$$RM = \frac{\chi_2 - \chi_1}{\lambda_2^2 - \lambda_1^2}, \tag{34}$$

where λ_2 is longer than λ_1. For observing polarization angles, the centimeter wave

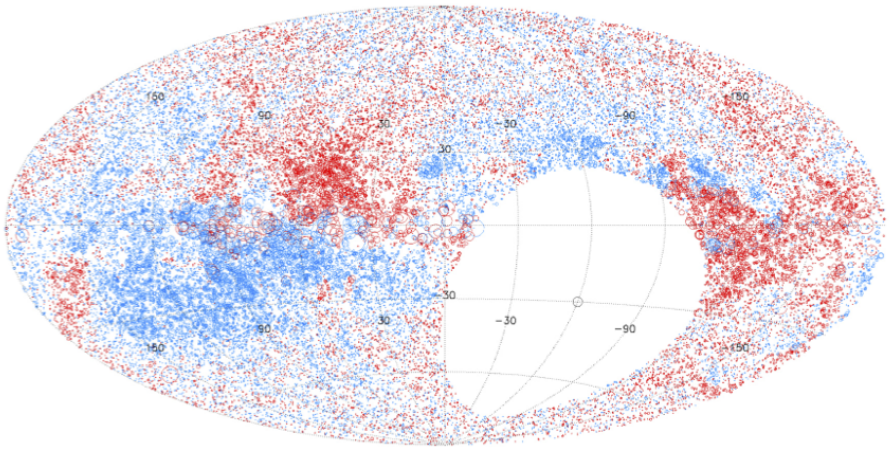

Figure 6: RM distribution over the sky north of δ =40°(from Taylor et al., 2009). Red and blue circles are positive and negative values of the RM, respectively. The size of the circle scales proportional to the magnitude of the rotation measure.

bands ($\sim$ 0.1–1 GHz) are very useful because its rotation angle is several to several tens degrees. For instance, typical values of the interstellar RM of $\sim$ 50 rad m^{-2} (Beck, 2001) lead to 3° at 3 cm ($\sim$ 10GHz), 126° at 21 cm ($\sim$ 1.4GHz), and 3672° at 85 cm ($\sim$ 0.35GHz). The observed polarization angles could have a nπ ambiguity because we cannot discriminate between the polarization angle of 0° and 180°. It complicates to decide the accurate value of the RM. In order to avoid the nπ ambiguity, we must observe polarization angles in at least three or more frequencies.

Figure 6 shows the RM distribution over the sky north of δ =−40° (Taylor et al., 2009), which includes 37, 543 galactic and extragalactic polarized radio sources. Red and blue circles represent the positive and negative values of the RM, respectively. We can see the quadrupole RM distribution in figure 6, suggesting the existence of an anti-symmetric halo field in the Milky Way galaxy. Even if there are magnetic fields without relativistic cosmic-ray electrons and the synchrotron emission, we can infer the magnetic filed strengths parallel to the line of sight through Faraday rotation of the linear polarization emitted from the sources beyond the target magnetic fields. Hence, RM of polarized radio sources located beyond the target magnetic fields are very useful for measuring the magnetic field strengths.

1.2.4. Interpretation of the Cluster RM

We can estimate the cluster magnetic field strengths from the standard deviation of the RM of a polarized radio source located beyond the magnetic fields. If we consider the simplest ideal case where the magneto-ionic plasma consist of the uniform electron densities, and uniform magnetic field strengths with a single scale and random direction, then the RM distribution of the polarized radio source becomes a Gaussian with zero mean and the variance of the RM is given by

$$\sigma^2_{\rm RM} = \frac{812^2 \Lambda_{\rm B}}{3} \int (n_{\rm e} B)^2 dl, \tag{35}$$

where $\Lambda_{\rm B}$ is the coherent length of the magnetic fields and $1/3$ indicates an assumption of the isotropic fields. For the thermal electron density distribution, we used a β-model, which is given by

$$n_{\rm e} = n_0 (1 + \frac{r^2}{r_{\rm c}^2})^{-3\beta/2}, \tag{36}$$

where n_0 is the central electron density in $\rm cm^{-3}$, r is the distance from the X-ray center in kpc, and $r_{\rm c}$ is the core radius of the ICM in kpc. Integrating and adopting equation (36) into equation (35) gives

$$\sigma_{\rm RM} = \frac{K B n_0 r_{\rm c}^{1/2} \Lambda_{\rm B}^{1/2}}{(1 + r^2/r_{\rm c}^2)^{(6\beta-1)/4}} \sqrt{\frac{\Gamma(3\beta - 0.5)}{\Gamma(3\beta)}}, \tag{37}$$

where $B = \sqrt{3 B_{\parallel}}$ and Γ is the Gamma function. K is the constant which depends on the position of a polarized radio source along the line of sight; $K = 624$ if the source is located beyond the cluster and $K = 441$ if the source is located at a halfway of the cluster (Lawler & Dennison, 1982; Tribble, 1991; Feretti et al., 1995; Felten, 1996; Govoni et al., 2010).

Hence, we can estimate the cluster magnetic field strengths from the observed standard deviation of the RM of the polarized radio source located beyond the cluster if the density profile of the ICM is known.

1.2.5. Depolarization

Depolarization is a phenomenon where the observed polarization intensity gets weaker than the intrinsic polarization intensity. It takes place in a situation where linear polarizations which have different polarization angles are detected within the telescope beam. If we assume a complex plane of Stokes Q and U with $V = 0$, then the complexed linear

polarization is given by

$$\begin{aligned} P &= \int p_0 \epsilon e^{2i\chi} dl & (38)\\ &= |P| e^{2i\chi} & (39)\\ &= Q + iU, & (40) \end{aligned}$$

where P is the complexed linear polarization intensity, p_0 is the intrinsic fractional polarization, ϵ is the synchrotron emissivity, χ is the polarization angle, and l is the path length of the emitting region (Burn, 1966; Gardner & Whiteoak, 1966; Sokoloff et al., 1998). If we consider a situation where we detect two polarizations which have different polarization angles, χ_1 and χ_2, within the telescope beam, and assume $p_0 = 1$ and $\epsilon = 1$ for simplicity, then the polarization intensity is given by

$$\begin{aligned} |P| &= \left| e^{2i\chi_1} + e^{2i\chi_2} \right| \\ &= \left| (\cos 2\chi_1 + \cos 2\chi_2) + i(\sin \chi_1 + \sin \chi_2) \right|, & (41) \end{aligned}$$

and the square of the $|P|$ is given by

$$\begin{aligned} |P|^2 &= \left[\sqrt{(\cos 2\chi_1 + \cos 2\chi_2)^2 + i(\sin \chi_1 + \sin \chi_2)^2} \right]^2 \\ &= 2 + 2\left[\cos 2(\chi_1 - \chi_2)\right]. & (42) \end{aligned}$$

We therefore get the reduced polarization intensity which is weaker than the intrinsic polarization intensity. For instance, if the difference of the polarization angles between χ_1 and χ_2 is 90°, we get the polarization intensity $|P| = 0$.

Depolarization is mainly classified into two types, wavelength-dependent depolarization and wavelength-independent depolarization. Wavelength-independent depolarization occurs in a situation where the direction of the magnetic fields are non-uniform in the telescope beam. In this case, the polarization angles of the linear polarizations emitted from the cosmic-ray electrons within the non-uniform magnetic fields are distinct from each other, and the integrated polarization intensity is reduced (Figure 7a).

Wavelength-dependent depolarization is caused by Faraday rotation, and classified into 3 types, differential Faraday rotation (DFR), internal Faraday dispersion (IFD), and external Faraday dispersion (EFD). DFR occurs in a region where the relativistic cosmic-ray electrons, thermal electrons, and uniform magnetic fields exist. The linear polarization emitted from backside of the magnet-ionic plasma viewed from the observer suffers Faraday rotation more than that from foreside of the magneto-ionic plasma. We

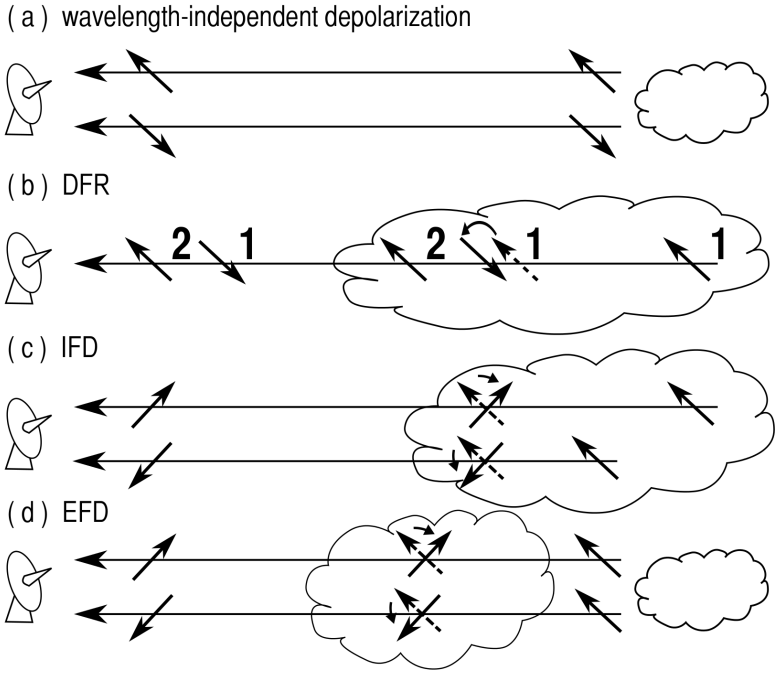

Figure 7: Schematic illustration of the depolarizations. (a) The wavelength-independent depolarization. (b) The differential Faraday rotation. (c) The internal Faraday dispersion. (d) The external Faraday dispersion. Long allows represent the linear polarization and short arrows represent the orientation of the polarization angle.

therefore detect the polarization which have the different polarization angles, and the integrated polarization intensity is reduced (Figure 7b). IFD occurs in a region where the relativistic cosmic-ray electrons, thermal electrons, and random magnetic fields exist. The random magnetic fields lead to different RM at the different location in the telescope beam, and the linear polarizations emitted from the magneto-ionic plasma suffer different Faraday rotation in each location in the telescope beam. We therefore detect the different polarization angles in the telescope beam, and the integrated polarization intensity is reduced (Figure 7c). EFD occurs in a region where the thermal electrons and random magnetic fields exist. Depolarization process is similar to IFD, but the linear polarization is emitted from the independent polarized sources beyond the magneto-ionic plasma (Figure 7d). IFD and EFD depolarizations depend on the telescope beam size and coherent length of the random magnetic fields. Hence, IFD and EFD depolarizations are called beam depolarization (Burn, 1966; Sokoloff et al., 1998).

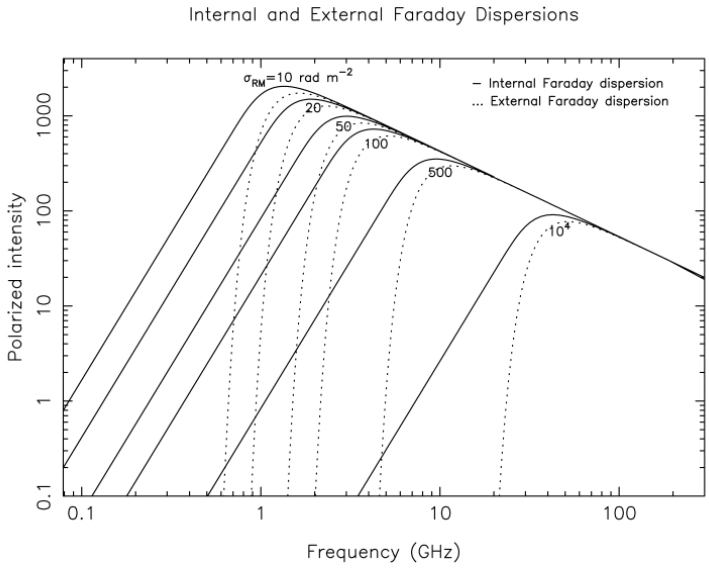

Figure 8: Spectral energy distribution of polarization intensity depolarized by internal (solid line) and external (dashed line) Faraday dispersion at different levels of $\sigma_{\rm RM}$ (from Arshakian & Beck, 2011).

The dependencies of DFR, IFD, and EFD are analytically investigated by Burn (1966); it is called Burn's law. The fractional polarization of the DFR, IFD, and EFD can be written as

$$p_{\rm DFR} = p_0 \frac{\left|\sin(2RM\lambda^2)\right|}{|2RM\lambda^2|}, \tag{43}$$

$$p_{\rm IFD} = p_0 \frac{1-e^{-S}}{S}, \tag{44}$$

and

$$p_{\rm EFD} = p_0 e^{-S}, \tag{45}$$

respectively, where p_0 is the intrinsic fractional polarization, RM is the rotation measure, and λ is the observation wavelength. The parameter S is defined as

$$S = 2\sigma_{\rm RM}^2 \lambda^2, \tag{46}$$

where $\sigma_{\rm RM}$ is the standard deviation of the RM within the region of consideration. DFR depends on the RM, and IFD and EFD depend on the standard deviation of the RM within the telescope beam.

Figure 8 shows the dependencies of the IFD and EFD (Arshakian & Beck, 2011). The solid and dashed lines represent the polarization intensity of the IFD and EFD, respectively. We can see the break points which depend on the $\sigma_{\rm RM}$. If we measure the polarization intensity (or fractional polarization) and find the break point, we can derive the standard deviation of the RM and infer the nature of the magnetic fields in the region where the depolarization occur.

1.2.6. Faraday Tomography

Faraday tomography is a method used to interpret polarization spectra. Fourier transformation of the polarization spectra gives a function called Faraday dispersion function, which provides us information of the polarized sources along the line of sight (Burn, 1966; Ideguchi et al., 2014). We introduce a fundamental theory of Faraday tomography.

At first, we define Faraday depth of a source as

$$\phi(l) = \int_{l}^{0} n_{\rm e}(l') B_{\parallel}(l') dl', \tag{47}$$

where l' is the physical distance and l is the distance from the observer to the position l. Faraday depth $\phi(l)$ is roughly same as the RM (equation 33), but Faraday depths is the integrated value from the observer to the position l, whereas the RM is the integrated value from the observer to the source. In the Faraday depth space, the sources are separated into Faraday thin or Faraday thick. If the source is $\lambda^2 \Delta\phi \ll 1$, it is called Faraday thin. If the source is $\lambda^2 \Delta\phi \gg 1$, it is called Faraday thick (Brentjens & de Bruyn, 2005). From the Faraday depth as a function of the physical distance l, the polarization angle χ is also rewritten as

$$\chi(l) = \chi_0(l) + \phi(l)\lambda^2, \tag{48}$$

where χ_0 is the intrinsic polarization angle and λ is the wavelength.

Burn (1966) found that the complexed linear polarization is given by

$$P(\lambda^2) = \int_{-\infty}^{\infty} F(\phi) e^{2i\phi\lambda^2} d\phi, \tag{49}$$

where $F(\phi)$ is the Faraday dispersion function (FDF) defined as

$$F(\phi) \equiv \epsilon(\phi) e^{2i\chi_0(\phi)}, \tag{50}$$

which represent the distribution of the polarization intensity at different Faraday depth. The FDF can be reconstructed from the inverse Fourier transformation of equation (49) as

$$F(\phi) = \int_{-\infty}^{\infty} P(\lambda^2) e^{-2i\phi\lambda^2} d\lambda^2. \tag{51}$$

The Fourier transformation is called Faraday tomography. Although the FDF does not directly provide us the physical space distribution of the polarized radio emissions, the FDF is imprinted in the distribution of the magnetic fields, thermal electrons, and relativistic cosmic-ray electrons along the line of sight. Hence, we can derive information of the distribution from the FDF (Beck et al., 2012).

However, we can only measure the positive and limited λ^2, and it yields the uncompleted reconstruction of the FDF. Brentjens & de Bruyn (2005) reported that, with a window function $W(\lambda^2)$, the limited observed polarization intensity $\tilde{P}$ is written as

$$\tilde{P} = W(\lambda^2) P(\lambda^2), \tag{52}$$

and we obtain

$$\tilde{P} = W(\lambda^2) \int_{-\infty}^{\infty} F(\phi) e^{2i\phi\lambda^2} d\phi. \tag{53}$$

Substituting $\lambda^2 = \pi u$ into equation (53), we define a function called rotation measure spread function (RMSF)

$$R(\phi) = \frac{\int_{-\infty}^{\infty} W(\pi u) e^{-2i\pi\phi u} du}{\int_{-\infty}^{\infty} W(\pi u) du}. \tag{54}$$

From equation (54), the window function $W(\pi u)$ is expressed as

$$W(\pi u) = \left(\int_{-\infty}^{\infty} W(\pi u) du \right) \int_{-\infty}^{\infty} R(\phi) e^{2\pi i\phi u} d\phi, \tag{55}$$

and the convolution theorem leads

$$F(\phi) ** R(\phi) = \frac{\int_{-\infty}^{\infty} \tilde{P}(\pi u) e^{-2i\pi\phi u} du}{\int_{-\infty}^{\infty} W(n\pi) du}, \tag{56}$$

where $**$ represents the convolution. Hence, the FDF with the window function $\tilde{F}$ is

given by

$$\tilde{F} = K^{-1}R(\phi) * *F(\phi), \tag{57}$$

$$R(\phi) = K\int_{-\infty}^{\infty} W(\lambda^2)e^{2i\phi\lambda^2}d\lambda^2 \tag{58}$$

$$K = \left(\int_{-\infty}^{\infty} W(\lambda^2)d\lambda^2\right)^{-1} \tag{59}$$

(Brentjens & de Bruyn, 2005; Heald et al., 2009). The RMSF constrains the quality of the FDF, and its role is equivalent to the synthesized beam of the dirty map in the radio interferometry.

1.3. Magnetic Fields in the Clusters of Galaxies

The magnetic fields in the clusters of galaxies play an important role in cluster physics. They connect cosmic-ray particles with ICM, inhibit the heat conduction, affect the motion of comic-ray particles, and accelerate the cosmic-ray particles. The accelerated relativistic cosmic-ray electrons within the cluster magnetic fields generate the diffuse and extended radio emission. Most of the information of the cluster magnetic fields are measured through the observations of the diffuse radio emissions and RM of the polarized radio source located inside or behind the cluster of galaxies.

The diffuse synchrotron radio emission revealed the existence of cluster magnetic fields occupying the whole region of the cluster. From the polarization observations, radio relics are highly polarized, and there are ordered magnetic fields over the several hundreds kpc scale in the relic region (see Figure 8). In contrast, radio halos are unpolarized. This would be the results of the beam depolarization (IFD or EFD) and wavelength independent-depolarization, suggesting the existence of the turbulent magnetic fields smaller than the telescope beam size. Actually, Cho & Ryu (2009) reported that if we assume the typical cluster core size of $\sim$ 100 kpc, the coherent length of the cluster magnetic fields is $\sim$ 20 kpc in their MHD simulation, and the results is inconsistent with the existence of the depolarization.

The key of the magnetic field measurements is Faraday rotation measure. Although RM must need the polarized radio sources inside or behind the cluster, RM allow us to measure the cluster magnetic fields without diffuse synchrotron radio emissions. Strong polarized radio sources are often located in cluster core region (Carilli & Taylor, 2002). The polarization emitted from the polarized source is affected by the Faraday rotation in the cluster magnetic fields.

The first study of the cluster magnetic fields with the background polarized radio sources was performed by Kim et al. (1990). They used RM of 18 polarized radio sources in Coma cluster, and found the significant contribution to the RM of the polarized radio sources. From the electron density model estimated by X-ray data, they found the cluster magnetic fields with the strength of 2 μG. After that, they again estimated the magnetic field strength in Coma cluster using 106 polarized radio sources, and improved the strengths as 1 μG (Kim et al., 1991). Recently, Govoni et al. (2010) estimated the cluster magnetic field strengths (Abell 401, Abell 2142, Abell 2065, Ophiuchus cluster) using the standard deviation of RM (equation 37) of the individual polarized sources observed with the VLA. They show that the cluster magnetic field strengths are micro Gauss order, and the RM distribution within the individual polarized radio source have patchy structure, indicating the turbulent magnetic fields with a few kpc scale. The consensus of these study (Lawler & Dennison, 1982; Kim et al., 1990, 1991; Tribble, 1991; Feretti et al., 1995; Felten, 1996; Govoni et al., 2010) is that the cluster magnetic field strengths and coherent lengths are micro Gauss order and kpc scale, respectively.

The cluster magnetic field strengths are considered to decline with the cluster radius because the field strengths would depend on the density of the ICM and mass distribution of the member galaxies in the cluster (Jaffe, 1980). The radial profile of the cluster magnetic fields would be predicted from the observations of the radio halos, which cover the whole region of the cluster. The spectral index distribution of the radio halo is created in few clusters such as Coma cluster, and have the radial steepening (Giovannini et al., 1993). If we assume that the radiative cosmic-ray electrons within the radio halo are re-accelerated by the primary electron model, then the observed spectral index distribution reflects the distribution of the combination between the magnetic field strengths and efficiency of the re-acceleration, and we can constrain the radial profile of the cluster magnetic fields. Brunetti et al. (2001) estimated the radial profile of the magnetic fields strengths in Coma cluster, assuming an electron re-accelerated model. As the result, the field strength decrease from $0.5 - 1.5$ μG at the cluster center to $0.03 - 0.05$ μG at 1.3 Mpc radius with the trend similar to that of the ICM (Govoni & Feretti, 2004)

The amplification process of the cluster magnetic fields have been debated. Ryu et al. (2008) proposed the scenario that the turbulent-flow motions are induced via the cascade of the vorticity generated at cosmological shocks during the formation of the large scale structure, and the turbulence amplify the seed magnetic fields. As the results of their MHD simulations, they found that the energy of the turbulence are converted

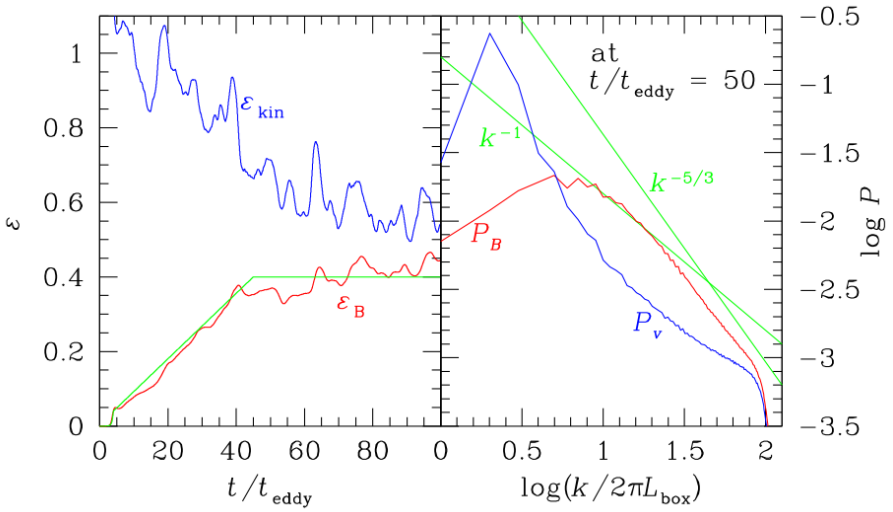

Figure 9: *Left panel*: Time evolution of the kinetic and magnetic energies in a three dimensional MHD simulation (from Ryu et al., 2008). Blue line represents the kinetic energy density, red line represents the energy density of the magnetic fields, and green line represents the fitting results for the magnetic field energy, respectively. *Right panel*: Power spectra for flow velocity and magnetic fields at a time of saturation. Blue line represent the power for the flow velocity, red line represents the power for the magnetic fields, and green lines represent the sample line with the index of $-5/3$ and -1, respectively.

into the magnetic fields energy as

$$\epsilon_{\rm B} = \phi(\frac{t}{t_{\rm eddy}})\epsilon_{\rm turb}, \tag{60}$$

and intergalactic magnetic fields are given by

$$B = [8\pi\epsilon_{\rm turb}\phi(\omega t_{\rm age})]^{1/2}\,, \tag{61}$$

where $\epsilon_{\rm B}$ is the energy density of the magnetic fields, $\phi(t/t_{\rm eddy})$ is the conversion factor, and $t_{\rm eddy}$ is the eddy turnover time, respectively. The energy of the turbulence is assumed to be $\epsilon_{\rm turb} = (1/2)\rho v_{\rm curl}^2$, where $v_{\rm curl}$ is the component of the velocity constituting vorticity, and eddy turnover time is defined as the vorticity at driving scales: $t_{\rm eddy} \equiv 1/\omega_{\rm driving}$. The number of eddy turnovers in the age of the universe at a given z is estimated as $\omega t_{\rm age}$, where ω is the age of universe and $t_{\rm age}$ is the magnitude of the local vorticity, respectively (Ryu et al., 2008, 2010).

Figure 9 shows the time evolution of the kinetic and magnetic field energy, and power spectra for flow velocity and magnetic fields in the MHD simulation (Ryu et al., 2008). In left panel, the energy of the magnetic fields are increased as time proceeds against decreasing kinetic energy, suggesting the turbulence amplification of the magnetic fields. In right panel, the amplified magnetic fields show the Kolmogorov like power spectra with the index of $-5/3$.

Although the simulation assume that the turbulence is induced by the formation of the large scale structure, the turbulence would also be induced in the ICM through the cluster merger. Cluster magnetic fields could be amplified by the turbulence of the ICM in the merging cluster. Guidetti et al. (2008) simulated the three dimensional magnetic fields model of the cluster (Abell 2382) with the power spectra of the magnetic fields. They calculated the RM of the model, and compared the model and observed values of polarization properties of the polarized radio sources. As a result of the model fitting, they found that the cluster magnetic fields indicate the Kolmogorov index of 11/3, suggesting the existence of the turbulence and amplification of the cluster magnetic fields by turbulence.

1.4. Aim of this thesis

The cluster magnetic fields are a key to understanding the physical process of clusters of galaxies. We must understand the nature of the magnetic fields in merging clusters because a lot of phenomena introduced above originate from cluster mergers. Depolarization and Faraday tomography are enable to reveal the structure of the cluster magnetic fields along the line of sight, and we thus study the nature of the magnetic fields in the merging cluster using the depolarization and Faraday tomography. We chose the merging cluster of galaxies Abell 2256 because the cluster have the polarized radio sources and radio relic, which enable to carry out the depolarization modeling and Faraday tomography. In order to obtain the total intensity, fractional polarization, and RM, we carried out the multiple frequency polarimetry with the JVLA, and created the images of Stokes I, Q, and U. After that, we performed depolarization modeling and Faraday tomography. The layout of this thesis is as follows. In section 2, we will introduce the target cluster Abell 2256. In section 3, we will describe our JVLA observations and data reduction procedure. In section 4, we will show the observation results. In section 5, we will discuss the nature of the magnetic fields in Abell2256.

Throughout this paper, we assume the following cosmological parameters: $H_0 = 70.5$ km s^{-1} Mpc^{-1}, $\Omega_{\rm m0} = 0.27$, and $\Omega_{\Lambda 0} = 0.73$. The angular size of $1'$ corresponds to ~ 67 kpc at the red shift of Abell 2256, $z = 0.0581$, corresponding to $D = 247$ Mpc.

2. Merging Cluster Abell 2256

Abell 2256 is a nearby ($z = 0.0581$, Ebeling et al., 1998) cluster of galaxies with richness class 2 (Abell, 1958) located at (RA, Dec: $17^{\rm h}04^{\rm m}2\overset{\rm s}{.}3$, $+78°37'55\overset{''}{.}2$, Ebeling et al., 1998). Abell 2256 has been observed with the optical, X-ray, and radio.

Optical observations identified that Abell 2256 is a cluster just carrying out the cluster merger. Faber & Dressler (1977) measured the radial velocities of 14 member galaxies, and found the velocity dispersion of 1274 km s^{-1}. Fabricant et al. (1989) measured the radial velocities of 87 member galaxies, and found the flat velocity histogram, suggesting the existence of a velocity substructure of the member galaxies and cluster merger. More recently, Berrington et al. (2002) investigated the radial velocities of 277 member galaxies, and found the three velocity substructures of the member galaxies. They interpreted that the third velocity substructure is just now beginning to merge.

X-ray observations have also suggested the cluster merger of Abell 2256. The first X-ray image is obtained with the imaging proportional counter (IPC) aboard the Einstein Observatory, and Fabricant et al. (1984) found that the X-ray morphology is not symmetric. From the observation of the Roentgen satellite (ROSAT), Briel et al. (1991) found that the ICM has two separated peaks of the X-ray emission, suggesting the cluster merger (see the X-ray emission of Figure 10). More recently, Tamura et al. (2011) reported the radial velocity difference of ~ 1500 km s^{-1} in gas bulk motions of the substructures using the X-ray satellite Suzaku. Each temperature of two distinct ICM is estimated to be ~ 7 keV and ~ 4.5 keV, respectively (Sun et al., 2002). Abell 2256 is obviously a merging cluster of galaxies.

Radio observations discovered the existence of the radio halo, radio relic, and several radio sources in Abell 2256 (Bridle & Fomalont, 1976; Bridle et al., 1979; Rottgering et al., 1994; Miller et al., 2003; Clarke & Ensslin, 2006; Brentjens, 2008; van Weeren et al., 2009; Kale & Dwarakanath, 2010; van Weeren et al., 2012; Owen et al., 2014; Trasatti et al., 2015; Ozawa et al., 2015). The radio halo is located in the cluster center. The radius and flux density of the radio halo is estimated to be ~ 406 kpc and ~ 103 mJy at 1369 MHz, respectively (Clarke & Ensslin, 2006). The spectral index of the radio halo is estimated to be $\alpha = 1.5$ at 63–350 MHz and $\alpha = 1.1$ at 350–1369 MHz (van Weeren et al., 2012). The radio relic is located at the ~ 440 kpc north-west from the cluster center. It covers an area of $16\overset{'}{.}9 \times 7\overset{'}{.}8$, corresponding to 1125 kpc $\times$ 520 kpc (Clarke & Ensslin, 2006). The flux density is estimated to be ~ 462 mJy (Clarke & Ensslin, 2006), and the spectral index is $\alpha = 0.81$ (van Weeren et al., 2012). The high resolution and sensitivity observations revealed the filamentary structures within the radio relic (Clarke & Ensslin,

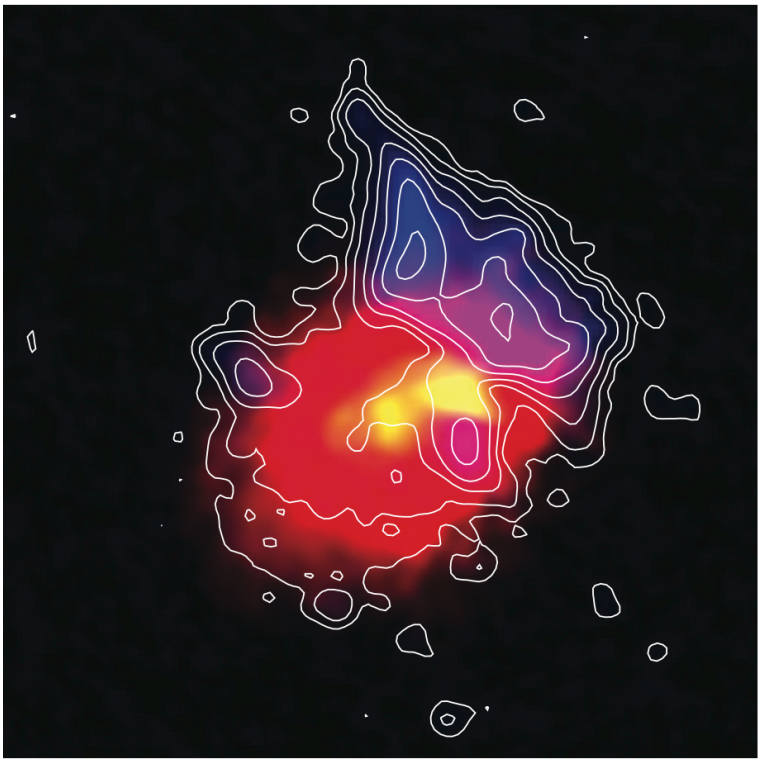

Figure 10: The total 1369 MHz intensity image of Abell 2256 in the VLA C and D array configurations (contours) overlaid on the Chandra X-ray image (colors) (from Clarke & Ensslin, 2006).

2006; Brentjens, 2008; Owen et al., 2014). Several radio sources are also found in Abell 2256. These radio sources are labeled with alphabets (Bridle & Fomalont, 1976; Bridle et al., 1979; Rottgering et al., 1994), and identification of the radio sources associated with the member galaxies of Abell 2256 are carried out by Miller et al. (2003). Few radio sources are confirmed to have a head-tail radio structure. Especially, the head-tail structure of Source C is elongated at least 480 kpc at 1.4 GHz and with a width of 2.5 kpc (Rottgering et al., 1994). Significant linearly polarized emission is detected from the radio relic, Source A, and Source B (Clarke & Ensslin, 2006), and these sources are suitable sources for measuring the RM.

The magnetic field strengths are estimated using the minimum and hadronic minimum energy condition with the emission of the radio halo, which are $B = 1.5$–3.2 μG and $B = 3.3$–8.9 μG, respectively (Clarke & Ensslin, 2006). Brentjens (2008) reported that the strength toward the relic filament G is estimated to be $B = 0.02$–2 μG.

3. Polarimetry with the JVLA

We will describe the details of the polarization observations with the JVLA. In order to measure the accurate RM, and perform the depolarization modeling and Faraday tomography, multiple frequency polarization observation data must be required. The JVLA is an ideal instrument for this purpose because it has wide frequency range, high resolution, and high sensitivity. At first, we will introduce the specifications of the JVLA, and our observations of Abell 2256. After that, we will introduce the reduction procedures of the JVLA polarization observation data. We summarized the reduction results of our JVLA visibility data in Section 3.3.9.

3.1. The Karl G. Jansky Very Large Array

The Karl G. Jansky Very Large Array (JVLA) is a radio interferometer located at an elevation of 2100 m on the Plains of San Agustin in New Mexico (Lat, Long: $34°04'43\overset{''}{.}497$N, $107°37'03\overset{''}{.}819$E), operated by the National Radio Astronomy Observatory (NRAO). The JVLA consist of 27 antennas of 25 m diameter in a Y-shaped array configuration. The antennas are put on rails, and the array configurations are changed four times a year. Usually, the JVLA composes four standard array configurations, called A, B, C and D array configurations, and the maximum and minimum baselines of each array configuration are 36.4, 11.1, 3.4, and 1.03 km, and 0.68, 0.21, 0.035, and 0.035 km, respectively. The frequency range is 0.058–50 GHz, which is separated into following bands: 4 band (0.054–0.086 GHz), P band (0.23–0.47 GHz), L band (1.0–2.0 GHz), S band (2.0–4.0 GHz), C band (4.0–8.0 GHz), X band (8.0–12.0 GHz), Ku band (12.0–18.0 GHz), K band (18.0–26.5), Ka band (26.5–40.0 GHz), and Q band (40.0–50.0 GHz).

The receiver can receive two different frequencies within the same band. At each frequency, RHCP and LHCP are received. Hence, the JVLA has 4 data streams, which are named Intermediate Frequency (IF). IF A and B, and IF C and D provide RHCP and LHCP, respectively, and IF A and C, and IF B and D are same frequency, respectively. Under the 8 bit sampler systems, the IF pairs are named A0/C0 pair and B0/C0 pair. Each pair can treat 1.024 GHz, and the total bandwidth is 2.048 GHz. The total bandwidth is separated into 16 bands with 128 MHz wide, called spectral window, and each spectral window separated into 64 channels with 2 MHz frequency resolution. With WIDAR correlator, we can derive the full polarization products of RR, RL, LR, and LL[2]. Therefore, the JVLA provides us the observations with wide frequency range, high resolution, and high sensitivity for extended radio sources at centimeter wavelength

[2]We referred the web page of the NRAO: `http://www.nrao.edu`

Figure 11: A photograph of the VLA in the D array configuration (from Perley et al., 2011).

(Perley et al., 2011).

3.2. Observations

We carried out the polarization observations of Abell 2256 with the JVLA at S (2–4 GHz) and X (8–10 GHz) bands in the C array configuration in August 2013. The bands were separated into 16 spectral windows, and each spectral window had a 128 MHz bandwidth and was separated into 64 frequency channels. We obtained the correlations of RR, RL, LR, and LL. The details of our JVLA observations are summarized in Table 1. Since the aim of our JVLA observations was to obtain the RMs toward the polarized radio sources, Source A and Source B, embedded in Abell 2256, the pointing center was Source A (RA, Dec: $17^{\rm h}03^{\rm m}31\overset{\rm s}{.}9$, $+78^\circ37'44\overset{''}{.}4$). The flux calibrator was 3C286, and the phase calibrator was 1803+784. The observed data are divided into five data for each observation date.

Table 1: Details of the VLA & JVLA observations of Abell 2256 (Ozawa et al., 2015).

	Frequency* (MHz)	Bandwidth* (MHz)	Config.*	Date	Time* (h)	Project*
VLA	1369/1417	25/25	D	1999-Apr-28	5.9, 5.9	AC0522
	1513/1703	12.5/25	D	1999-Apr-29	3.5, 5.5	
VLA	1369/1417	25/25	C	2000-May-29	2.5, 2.5	AC0545
	1513/1703	12.5/12.5	C	2000-May-29	3.6, 3.6	
	1369/1417	25/25	C	2000-Jun-18	2.5, 2.5	
	1513/1703	12.5/25	C	2000-Jun-18	4.1, 3.5	
JVLA	S-band 16 windows†	128	C	2013-Aug-25	1.2	13A-131
				2013-Aug-26	1.2	(this work)
				2013-Aug-29	1.2	
JVLA	X-band 16 windows‡	128	C	2013-Aug-18	1.3	13A-131
				2013-Aug-19	1.3	(this work)

* Column 2: observing frequency; Column 3: observing bandwidth; Column 4: array configuration; Column 5: dates of observation; Column 6: time on source; Column 7: NRAO project code.

† 2051/2179/2307/2435/2563/2691/2819/2947/3051/3179/3307/3435/3563/3691/3819/3947.

‡ 8051/8179/8307/8435/8563/8691/8819/8947/9051/9179/9307/9435/9563/9691/9819/9947.

3.3. Data Reductions

We introduce reduction procedures of the JVLA polarimetry data. In order to obtain the accurate RMs of the Source A and Source B from the brightness distributions of Stokes I, Q, and U, we must carry out the reduction of our JVLA data, which is the visibility. We must calibrate the amplitude, phase, D-term, and R−L phase difference in the JVLA visibility data. The reductions are performed with the common astronomy software applications (CASA), which is being developed in order to reduce the visibility data of the Atacama Large Millimeter/submillimeter Array (ALMA) and JVLA, but also useful for the data reduction of other radio telescopes[3]. However, we mainly used the NRAO astronomical image processing system (AIPS) because we would like to perform multi-scale CLEAN algorithm (MS-CLEAN), which is a deconvolving method. AIPS requires the format of flexible image transport system (FITS), but the original JVLA visibility data is a format of measurement sets (MS). We therefore performed the pre-reduction and conversion of the MS into the FITS using CASA. Subsequently, we carried out the reduction of the FITS using AIPS. Before introducing the reduction procedures, we firstly explain a visibility in Section 3.3.1. After that, we introduce the reduction procedures of the JVLA visibility data. The standard reduction procedure of the JVLA

[3] `http://casa.nrao.edu/docs/cookbook/`

polarimetry data is shown in Figure 12, and we summarize the result of the reduction in Section 3.3.9.

3.3.1. Observables in Interferometers

Interferometers measure the visibility which is defined as

$$V(u,v,w) = \int_{-\infty}^{\infty}\int_{-\infty}^{\infty} A(l,m)I(l,m)e^{[-2\pi i\{ul+um+w(\sqrt{1-l^2-m^2}-1)\}]}\frac{dldm}{\sqrt{1-l^2-m^2}}, \quad (62)$$

where V is the visibility, (l,m,n) is the cartesian coordinate system on the sky plane satisfying $l^2+m^2+n^2=1$ with the origin at pointing center $\mathbf{s}_0$ (each axis represent the north direction, east direction, and direction parallel to the $\mathbf{s}_0$, respectively), $A(l,m)$ is the normalized antenna reception pattern, $I(l,m)$ is the intensity of the source, and (u,v,w) is the spatial frequency defined as

$$(u,v,w) = (\frac{\mathbf{D}\cdot\mathbf{e}_l}{\lambda}, \frac{\mathbf{D}\cdot\mathbf{e}_m}{\lambda}, \frac{\mathbf{D}\cdot\mathbf{e}_n}{\lambda}), \quad (63)$$

where $\mathbf{D}$ is the baseline vector, $(\mathbf{e}_l, \mathbf{e}_m, \mathbf{e}_n)$ is the unit vector for the (l,m,n) coordinate system, and λ is the wavelength (Thompson et al., 2001). The phase term of equation (62) is the fringe phase $\phi_{\rm f}$, defined as

$$\phi_{\rm f} = 2\pi\nu(\tau-\tau_{\rm i}) = 2\pi\frac{\mathbf{D}\cdot(\mathbf{s}-\mathbf{s_0})}{\lambda} = 2\pi i\{ul+um+w(\sqrt{1-l^2-m^2}-1)\}, \quad (64)$$

where $\mathbf{s}$ is the arbitrary directional vector, $\tau = (\mathbf{D}\cdot\mathbf{s})/c$ is the geometrical time delay, and $\tau_i = (\mathbf{D}\cdot\mathbf{s}_0)/c$ is the instrumental time delay, which corrects the geometrical time delay. Therefore, the phase of the visibility includes the information of source positions. For instance, the radiation from the direction of the (l,m) origin gives $\tau=0$.

If we consider that the mapping region is sufficiently small ($l^2+m^2 \ll$), then $n = \sqrt{1-l^2-m^2} \sim 1$ rewrites equation (62) as

$$V(u,v) = \int_{-\infty}^{\infty}\int_{-\infty}^{\infty} A(l,m)I(l,m)e^{\{-2\pi i(ul+um)\}}dldm. \quad (65)$$

Performing the inverse Fourier transformation gives

$$A(l,m)I(l,m) = \int_{-\infty}^{\infty}\int_{-\infty}^{\infty} V(u,v)e^{\{2\pi i(ul+um)\}}dudv. \quad (66)$$

The relationship between the intensity and visibility is called van Cittert-Zernike theo-

rem. We can reconstruct the brightness distribution on the sky plane, integrating the visibilities from negative infinity to positive infinity. However, we can obtain the visibilities only in the finite region because we have finite antennas and baselines, and it is a cause of incompleteness of the reconstructed brightness distribution. If we represent the true visibility as $V(u, v)$, then the observed visibility $V'(u, v)$ can be written as

$$V'(u, v) = V(u, v)U(u, v), \tag{67}$$

where $U(u, v)$ is the weighting function called uv coverage. The inverse Fourier transformation of equation (67) is given by

$$\begin{aligned} \mathrm{FT}\{V'(u, v)\} &= \mathrm{FT}\{V(u, v)\} * *\mathrm{FT}\{U(u, v)\} \\ &= I(l, m) * *B(l, m), \end{aligned} \tag{68}$$

where $**$ represents the convolution, and $B(l, m)$ is the synthesized beam. If we obtain the brightness distribution from interferometers, the obtained brightness distribution is the convolution of true brightness distribution and synthesized beam, which is called dirty map, and we must deconvolve the brightness distribution from the dirty map.

Hereafter, we will explain the reduction process of our JVLA visibility data. The reduction of the amplitude (intensity) and phase included in the visibility are important for the reconstruction of the brightness distributions, and the deconvolution process is needed to remove the synthesized beam from the dirty map. For the brightness distributions of Stokes Q and U, the polarization calibrations are needed, and we will introduce that in Section 3.3.6.

3.3.2. Pre-reduction with CASA

With CASA, we have to perform the VLA calibration pipeline and conversion of the MS into the FITS. The VLA calibration pipeline performs the basic flagging and calibration[4], and we must perform it because the MS is a raw data. In order to succeed with the pipeline processes, the JVLA visibility data must contain a flux density calibrator, and a gain and phase calibrator. In our JVLA observations, 3C286 is the flux density calibrator, 1803+784 is the gain and phase calibrator, and Abell 2256 is the target source. The script of the VLA calibration pipeline is distributed on the website of the NRAO, and work on CASA. The conversion of the MS into the FITS is needed to carry out the reduction with AIPS. We would like to perform MS-CLEAN within AIPS in order to

[4] `https://science.nrao.edu/facilities/vla/data-processing/pipeline`

deconvolve the brightness distribution.

At first, we have to start CASA at the directory on your computer where you stored the MS. When we start CASA, there are two windows, the main terminal and log messages window. Following procedures, we type commands into the main terminal. For performing the pipeline, we type `EXECFILE('***/EVLA_PIPELINE.PY')`, and apply hanning smoothing as `hanning smoothing => y`, which reduce the Gibbs phenomenon. Several hours later, the pipeline processes should be finished. After that, we convert the MS into the FITS, typing `EXPORTUVFITS(VIS='***.MS',FITSFILE= '***.FITS')`. We have to move the converted FITS into the AIPS directory, for instance `/USR/LOCAL/AIPS/FITS`.

3.3.3. Loading the Data

With AIPS, we carry out the reduction of the JVLA visibility data in the FITS. At first, we start AIPS using terminal. When we start AIPS, there are three windows, the main terminal, message window, and TV window. Following procedures, we type commands into the main terminal. Message window shows you the results of task you executed, and TV window shows you the results of any plots you executed.

For loading the FITS, we use `TASK 'FITLD'`. Before executing the task, we should type `DEFAULT`, which is the verb to initialize the states of the task parameters, and must input the task parameters. We input the parameter `DATAIN 'FITS:***.FITS'`, and type `GO`. Then, the `TASK 'FITLD'` should be started. If the `TASK 'FITLD'` is finished without any troubles, "Appears to have ended successfully" is displayed in the message window. If you have any troubles, "Purports to die of UNNATURAL causes" is displayed in the message window. Since our JVLA observations were carried out for five days (see Table 1), we have five FITS converted from five MSs, and must execute the `TASK 'FITLD'` five times. The loaded FITS is called a catalogue, which have some information in the form of table, for instance, SU table has the information of the flux density, FG table has the information of the flagging.

If we have the archival data observed with the VLA, we have to use `task 'FILLM'` with the parameter `DATAIN 'FITS:***.XP'` (not `.XP1`) in order to load the archival data which have the extension of `.XP1`. Note that, if the extension is not `.XP1`, such as `.XP2` and `.XP3`, we have to rewrite the extension to `.XP1`.

3.3.4. Checking and Flagging the Data

We have to check the visibility data after loading the data. We can see the header of the FITS, using `'IMH'`. If you want to see more details of the visibility data, `TASK 'LISTR'`

with the parameter OPTYPE='SCAN' shows you a scan information. However, we must make a NX table before executing the TASK 'LISTR' because our JVLA visibility data does not contain the NX table, which is required to execute the TASK 'LISTR'. In order to create the NX table, we have to execute TASK 'INDXR' with default parameter states. TASK 'UVPLOT' graphically shows you the visibility information on the TV window. Especially, the plot of the amplitude versus time is very useful to find radio frequency interference (RFI). However, it is too heavy to perform the TASK 'UVPLOT' and following reduction processes. In our JVLA visibility data, each spectral window was separated into 64 frequency channels. We therefore averaged the data of 64 channels in the frequency domain using TASK 'AVSPC' with the default parameter states.

If you find RFI components in the visibility data, you must remove it using tasks such as 'UVFLG', 'CLIP', 'TVFLG', and 'QUACK'. When we execute these tasks, AIPS creates and updates a FG (flag) table, which store the information of the flagging. We should use the TASK 'QUACK' with the parameters PARM=0,1/6,0 and OPCODE='BEG' because the task can remove the first time of the scan, which are affected by the oscillation of the antennas. TASK 'UVFLG' and TASK 'CLIP' remove the RFIs in the time domain. If one of the antennas have some problems, then the baselines containing that one would also show artificial effects. In that case, we should remove the baseline containing that one using the TASK 'TVFLG'.

3.3.5. Amplitude and Phase Calibration

We carry out the calibration of the amplitude and phase of the observed sources. We execute the tasks in order of TASK 'SETJY', VLACALIB, TASK 'GETJY', and VLACLCAL. AIPS reflects the reduction results to the observed sources, applying CL (calibration) table to the original visibility data. We therefore have to create and renew the CL table through the reduction tasks.

Firstly, we write a true flux density of the flux calibrator into SU (source) table using the TASK 'SETJY' with the parameters SOURCES='flux cal.', and OPTYPE='CALC'. From the extrapolation of the known flux density of the flux calibrator, we obtain the true flux density of the flux calibrator at observed frequency. This task is needed for obtaining the gain of the flux density of the observed flux calibrator.

The flux calibrators (e.g. 3C48 and 3C286) have the models of the structure. We can determine the gain and phase solutions of the observed flux calibrator using the VLACALIB with the parameter CALSOUR='flux cal.','phase cal.''. We also determine the phase solutions of the phase calibrator which is regarded as a point source. Obtained gain and phase solutions are written in SN (solution) table. Before executing

the VLACALIB, we must to type RESTORE 0 and RUN VLAPROCS to define a number of procedures used in the VLACALIB and VLACLCAL. After that, typing VLACALIB, the process will be started, and new SN table should be created.

The flux density of the phase calibrator is determined using TASK 'GETJY' with the parameters 'SOURCES='phase cal.'', and CALSOUR='flux cal.''. TASK 'GETJY' can determine the flux density of the phase calibrator from the flux calibrator based on the flux density of the SU table and the gain solution of the SN table. The corrected values of the phase calibrator are reflected into the SU and SN tables.

Finally, we apply the SN table, which have the solutions of the amplitude and phase, to the CL table using VLACLCAL. Created CL table enable to show you the corrected visibility of the target source. The parameters are SOURCES='phase cal.', 'flux cal.', 'target source'', CALSOUR='phase cal.', OPCODE='CALI', and INTERPOL='2PT'. When you type VLACLCAL, the process will be started, and new CL table should be created.

3.3.6. Polarization Calibration

In order to obtain accurate information of the polarization, we must carry out polarization calibrations, D-term and Right−Left (R–L) phase difference correction. Firstly, we carry out D-term correction.

If we observe unpolarized sources, we ideally detect unpolarized radio emission. However, the non-ideal characteristics of the antennas yield the polarized emission from the unpolarized sources. We can interpret the effect of the non-ideal characteristics of the antennas as the instrumental polarization leakage called D-term. If we receive the orthogonal signal $V'_{\rm x}$ and $V'_{\rm y}$, the polarization leakage can be written as

$$V'_{\rm x} = V_{\rm x} + D_{\rm x} V_{\rm y} \tag{69}$$

$$V'_{\rm y} = V_{\rm y} + D_{\rm y} V_{\rm x}, \tag{70}$$

where $D_{\rm x}$ and $D_{\rm y}$ are the D-terms, and $V_{\rm x}$ and $V_{\rm y}$ are the received signal with an ideally antenna. For more details of D-term, see Thompson et al. (2001).

TASK 'PCAL' estimates the instrumental polarization leakage using phase calibrators observed with a wide range of parallactic angles. Derived source polarizations are put in the SU table, and the polarization leakage terms are put in AN (antenna) table. The parameters are CALSOUR='phase cal.', DOCALIB=1, GAINUSE=0, PMODEL=0, SOLINT=2, SOLTYPE='APPR', and PRTLEV=1.

After the D-term correction, we have to correct the R–L phase difference of the polar-

Table 2: Right−Left phase differences (degrees) and fractional polarization (%) of the polarization calibrators. [5]

Source	20cm		6cm		3.7cm		2cm		1.3cm		0.7cm	
3C48	−60	0.4	−148	4.1	−138	5.6	−134	7.0	−146	8.2	−172	8.8
3C138	−15	8.0	−20	11.4	−22	11.7	−24	11.7	−30	11.6	28	12.2
3C147	N/A	< 0.1	16	0.4	−54	0.7	109	2.9	147	4.5	170	6.5
3C286	66	9.4	66	11.2	66	11.6	66	12.1	66	12.4	66	13.3

ization calibrator. R–L phase difference is the phase difference between the RHCP and LHCP. We have the accurate R–L phase differences for some polarized sources, which are shown in Table 2. Especially, 3C286 is the best source for the calibration because it is not only the polarization calibrator but also the flux calibrator. Moreover, the R–L phase difference of 3C286 is 66° within the range of the wavelengths between 0.7 and 20 cm.

`TASK RLDIF` determines the R–L phase difference of the phase calibrator. The parameters are `CALSOUR='polarization cal'`, `DOCALIB=1`, `DOPOL=1`, `DOAPPLY=1`, and `GAINUSE=0`. When we execute the task, the CL table is updated. After that, we should confirm the R–L phase difference with `DOAPPLY=-1`. If the task is succeeded, we should be able to confirm the corrected RL phase difference as in Table 2.

3.3.7. Concatenating the Visibility Data

Sometimes, we have several visibility data which consist of same frequency band with the different observation dates and/or different array configurations. Then, we can concatenate the data with `TASK 'DBCON'`, and the uv coverage is further improved. Before executing the task, we have to carry out `TASK 'SPLIT'` to separate the multi-sources data into the single source data because the `TASK 'DBCON'` require the single source data. The parameters of the `TASK 'SPLIT'` is `DOCALIB=1`, `DOPOL=1`, `GAINUSE=0`, and `Sources='target source'`, and we apply the `TASK 'DBCON'` to SPLITEed data with default parameter states. Note that, the DBCONed data include the calibrated amplitude, phase, and polarization information without CL table. Hence, if we use the DBCONed data, then we have to set the parameters `DOCALIB=0` and `DOPOL=0` in the following tasks.

[5] `https://science.nrao.edu/facilities/vla/docs/manuals/obsguide/modes/calibration`

3.3.8. Imaging

As we have introduced in Section 3.3.1, we have to carry out the Fourier transformation of the visibilities in order to obtain the brightness distribution of the sources. Firstly, we create dirty map which is a convolution of the true brightness distribution of the sources and the synthesized beam using `TASK 'IMAGR'`. For the Fourier transformation of the visibilities, we can adjust the weighting function of the visibility using parameters `UVWTFN` and `UVTAPER`. If we choose `UVWTFN='NA'`, then we get natural weighting, which indicates that the visibilities with short baseline are treated as significant because the amount of the visibilities with shorter baseline are larger than that of the visibilities with longer baseline. `UVTAPER` controls the width in u and v directions of the Gaussian weighting function. We also have to determine the suitable values for the image quality. A pixel size is determined by the parameter `CELLSIZE`, and it should be one fourth of the telescope beam size. An amount of the pixels is determined by the parameter `IMSIZE`, and it must be the nth power of two. Using the parameter `STOKES=I,Q,` and `U`, we can choose Stokes parameters of the creating dirty maps.

After creating the dirty maps of Stokes I, Q, and U, we should obtain RMS levels of the dirty maps using `TVALL` and `IMSTAT`. When we measure the RMS of the dirty maps, we should choose small box in order to avoid the effect of the synthesized beam pattern. The obtained RMS levels constrain the number of iterations of the CLEAN process.

Next, we carry out the CLEAN, and create CLEANed maps of Stokes I, Q, and U. CLEAN is a process which deconvolves the true brightness distribution of the sources from the uv data convolving the synthesized beam. Standard CLEAN algorithm is also executed with `TASK 'IMAGR'`. However, the standard CLEAN algorithm create negative values of the flux density around the extended sources such as the radio relic, which is called negative bawl, because the standard CLEAN algorithm assume that the sky contain the only point sources. Since our JVLA visibility data contain the radio relic, we used multi-scale CLEAN (MS-CLEAN) algorithm, which assume that the sky includes extended sources. The process of the MS-CLEAN is as follows (Rich et al., 2008).

1 Assuming several CLEAN beams, and convolving the dirty maps with each CLEAN beam size.

2 Finding a peak, among the dirty maps.

3 Subtracting the convolved flux density of the dirty map where the peak was found from all the dirty maps.

4 AIPS store the subtracted component and the beam size in a table.

5 Repeating above process until all the emission has been removed.

Hence, the standard CLEAN algorithm carry out the process with a single CLEAN beam. In contrast, MS-CLEAN algorithm carry out the process with several CLEAN beams. In order to execute the MS-CLEAN algorithm, we referred to Rich et al. (2008) and Hunter et al. (2012).

`TASK 'IMAGR'` can also carry out the MS-CLEAN. We have to input the following parameters: `UVWTFN`, `UVTAPER`, `CELLSIZE`, `IMSIZE`, `DOTV`, `NITER`, `BMAJ`, `BMIN`, `BPA` , `NGAUSS`, `WGAUSS=`, `IMAGRPRM(11)`, `FGAUSS`, and `Stokes`. We have introduced `UVWTFN`, `UVTAPER`, `CELLSIZE`, and `IMSIZE` in the above sentence. If `DOTV=1`, the CLEAN is performed. `NITER` is the iteration limit of the CLEAN. `BMAJ`, `BMIN`, and `BPA` are the major and minor axes, and position angles of the original CLEAN beams in each frequency. Here, the `NGAUSS`, `WGAUSS`, `IMAGRPRM(11)`, and `FGAUSS` are the characteristic parameters of the MS-CLEAN. Each parameter determines the number of CLEAN beams, the sizes of the CLEAN beams, weight of the flux measured in each beam size, and RMS levels of the iteration limits, respectively. Rich et al. (2008) reported that the most important choice is the choice of the largest CLEAN beam size, that is the maximum value of `WGAUSS`. They found that the optimum results were obtained when they chose the largest CLEAN beam size which roughly corresponds to the size of the largest coherent structures visible in the dirty map. In our JVLA visibility data of Abell 2256, the largest structure is the radio relic. Since the coherent size of the radio relic is roughly $200''$, we decided the largest CLEAN beam size of $200''$. Although we decided the CLEAN beams as `FGAUS=0,40,65,90,200`, these are not the best values. We note that the best parameters of MS-CLEAN are still not revealed, and we have to search the best values.

After creating the images of Stoke I, Q and U, we must adjust the synthesized beam size (resolution) of the CLEANed maps with the same size in order to calculate the RMs. `TASK 'CONVL'` with the parameters `OPCODE='GAUS'`, `BMAJ`, and `BMIN` convolves the arbitrary Gaussian function with the images.

3.3.9. Summary of Data Reductions

We summarize the reduction results of our JVLA visibility data. From the JVLA observations of Abell 2256, we obtained the visibility data of the S and X bands, which contain 16 spectral windows. We checked the visibility data, and found the effect of RFIs at 2179, 2307, 3691, 3819, and 3947 MHz in the S band. We confirmed that there are satellite downlink and digital audio radio service in 2080–2290 MHz and 3700–4200

Table 3: Image qualities of total intensity and polarization at L, S, and X bands.

	Frequency* (MHz)	Beam* ($''\times''$)	$\sigma_{\rm I}$*	$\sigma_{\rm Q}$*	$\sigma_{\rm U}$*	$\sigma_{\rm p}$*
			(mJy beam^{-1})			
VLA	1369	47×47	0.163	0.028	0.022	0.017
	1417	47×47	0.152	0.031	0.020	0.017
	1513	47×47	0.183	0.041	0.028	0.032
	1703	47×47	0.259	0.046	0.095	0.063
JVLA	S-band 11 windows†	47×47	0.159	0.029	0.029	0.019
	S-band 11 windows†	15.1×15.1	0.151	0.013	0.014	0.009
	X-band 16 windows‡	15.1×15.1	0.053	0.027	0.028	0.018

* Column 2: observing frequency; Column 3: telescope beam size; Columns 4, 5, 6, and 7: RMS noise of the Stokes I, Q, U, and polarization intensity. We show the averaged RMS noise in the JVLA S-band 11 windows and X-band 16 windows.
† 2051/2435/2563/2691/2819/2947/3051/3179/3307/3435/3563.
‡ 8051/8179/8307/8435/8563/8691/8819/8947/9051/9179/9307/9435/9563/9691/9819/9947.

MHz, respectively[6]. We therefore removed five data, and we carried out the reduction with above reduction procedures.

Additionally, we also carried out the reduction of the VLA visibility data. The data is observed with the VLA in the C and D array configurations at L band (see Table 1). The reduction procedure is same as the JVLA, excepting Section 3.3.2.

As the results, we obtained Stokes I, Q, and U images of L, S, and X bands. In order to resolve the individual polarized sources, and detect the radio relic, we created the images of $15\farcs1$ resolution for the S and X bands, and the images of $47\farcs0$ resolution for the L and S bands. We did not create the images of $15\farcs1$ resolution for the L band, and the images of $47\farcs0$ resolution for the X band because of low resolution and also because of the radio relics which are outside the fields of view, respectively. The size of the images are 136×136 pixels for $15\farcs1$ resolution images, and 87×87 pixels for $47\farcs0$ resolution images. We show the image qualities of the VLA and JVLA observations in Table 3.

[6] `https://science.nrao.edu/facilities/vla/docs/manuals/oss/performance/rfi`

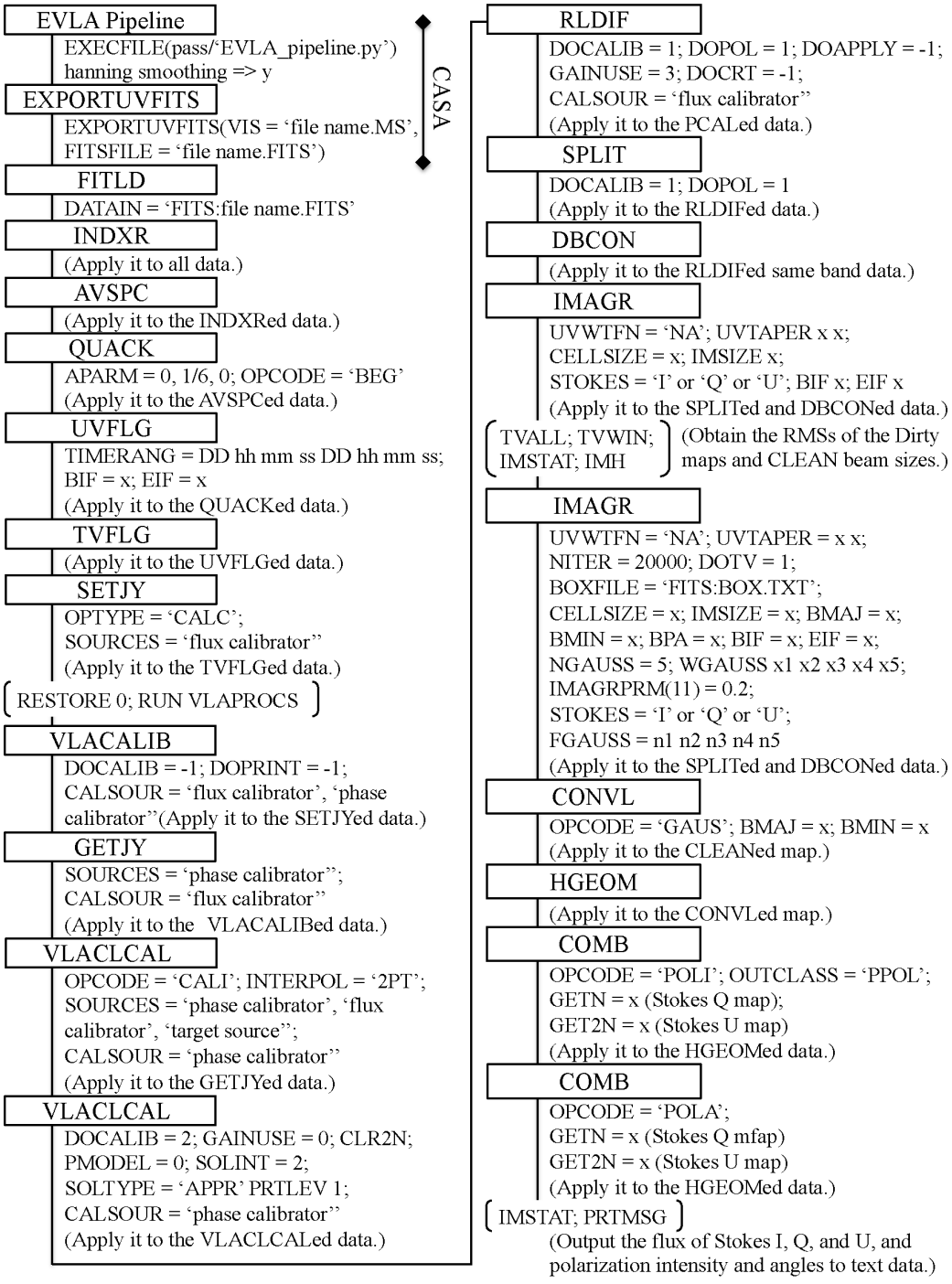

Figure 12: The standard reduction procedure of the JVLA polarization data. The framed characters represent the name of the TASK. The characters outside the frame represent the parameters for the TASK.

4. Results

In this chapter, we show the results of our reduction and analyses for the data of the merging cluster Abell 2256 observed with the JVLA. We obtained the total intensity, fractional polarization, and Faraday rotation measure in order to measure the magnetic fields in Abell 2256. As we have shown in Section 1.2, we can lead the information of the cluster magnetic fields from these obtained values; the total intensity leads the total magnetic field strengths of the emitting region, the fractional polarization (or polarized intensity) allow us to perform the depolarization modeling and Faraday tomography, the standard deviation of the Faraday rotation measure leads the magnetic field strengths along the line of sight toward the polarized radio sources. We note that the different measurement methods of the magnetic fields allow us to obtain the different spatial position information of the cosmic magnetic fields.

4.1. Radio Images

In Figure 13, we show the total 2051 MHz intensity image of Abell 2256 in the JVLA C array configuration. The radio relic and several radio sources are detected above $3\sigma_{\rm I}$ significance at 2051 MHz. In contrast, the radio halo detected in VLA and different observational instrument (e.g. Clarke & Ensslin, 2006; Brentjens, 2008; Kale & Dwarakanath, 2010; van Weeren et al., 2012) is not detected above $3\sigma_{\rm I}$ significance at 2051 MHz.

In the top left and top right panels in Figure 14, we show the total 2051 MHz and 3563 MHz intensity images of Abell 2256 with the polarization vectors, respectively. We drew the polarization vectors when the polarization intensity is larger than $3\sigma_{\rm P}$. Significant polarized radio emission is detected from the radio relic, Source A, and Source B in the S-band. In the S-band images except the data affected a by RFIs, the radio relic is detected in the Stokes I above $3\sigma_{\rm I}$ significance but the emitting region at 3563 MHz is smaller than that at 2051 MHz by a factor of ~ 0.37 (top right panel). Approximately, the full width at half power of the primary beam is $\theta_{\rm PB} = 45/\nu^7$ in the JVLA, where $\theta_{\rm PB}$ is in arcminutes and ν is the frequency in GHz. When we adopt $\nu = 3.5$ GHz, we have $\theta_{\rm PB} \sim 12\farcm9$. Since the distance from the Source A, which is the central position for the JVLA observations, to the outermost of the radio relic is over $10'$ in the image of 2051 MHz, a part of the radio relic could be the outside the field of views in the image of 3563 MHz.

[7] https://science.nrao.edu/facilities/vla/docs/manuals/oss2013b/performance/fov/referencemanual-all-pages

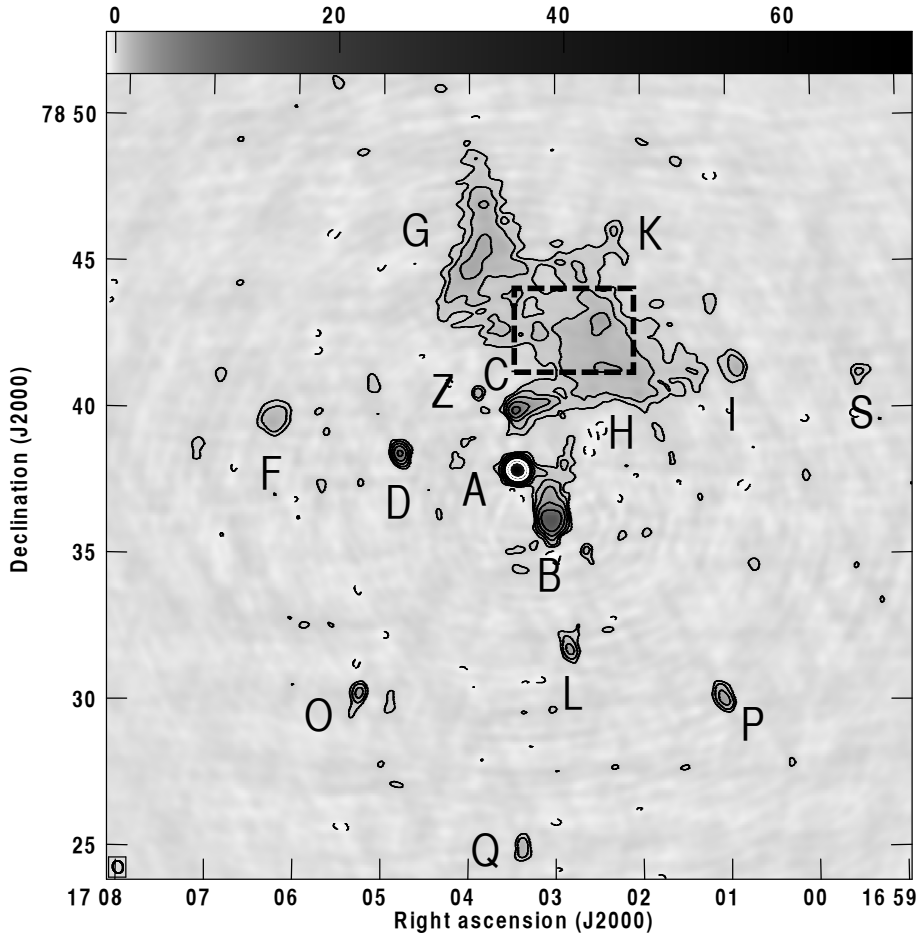

Figure 13: The total 2051 MHz intensity image of Abell 2256 in the JVLA C array configuration (from Ozawa et al., 2015). Contours are drawn at $(-3, 3, 6, 12, 24, 48, 96, 192) \times 140$ μJy beam^{-1}, corresponding to a surface brightness of 9.702×10^{-23} W m^{-2} Hz^{-1} sr^{-1}. The telescope beam size is shown in bottom left corner and is $25\overset{''}{.}8 \times 25\overset{''}{.}0$. Each alphabet represents the name of radio source labeled by Bridle & Fomalont (1976), Bridle et al. (1979), and Rottgering et al. (1994). Dashed frame region represents the region where the fractional polarization of the radio relic was measured (see Section 4.3).

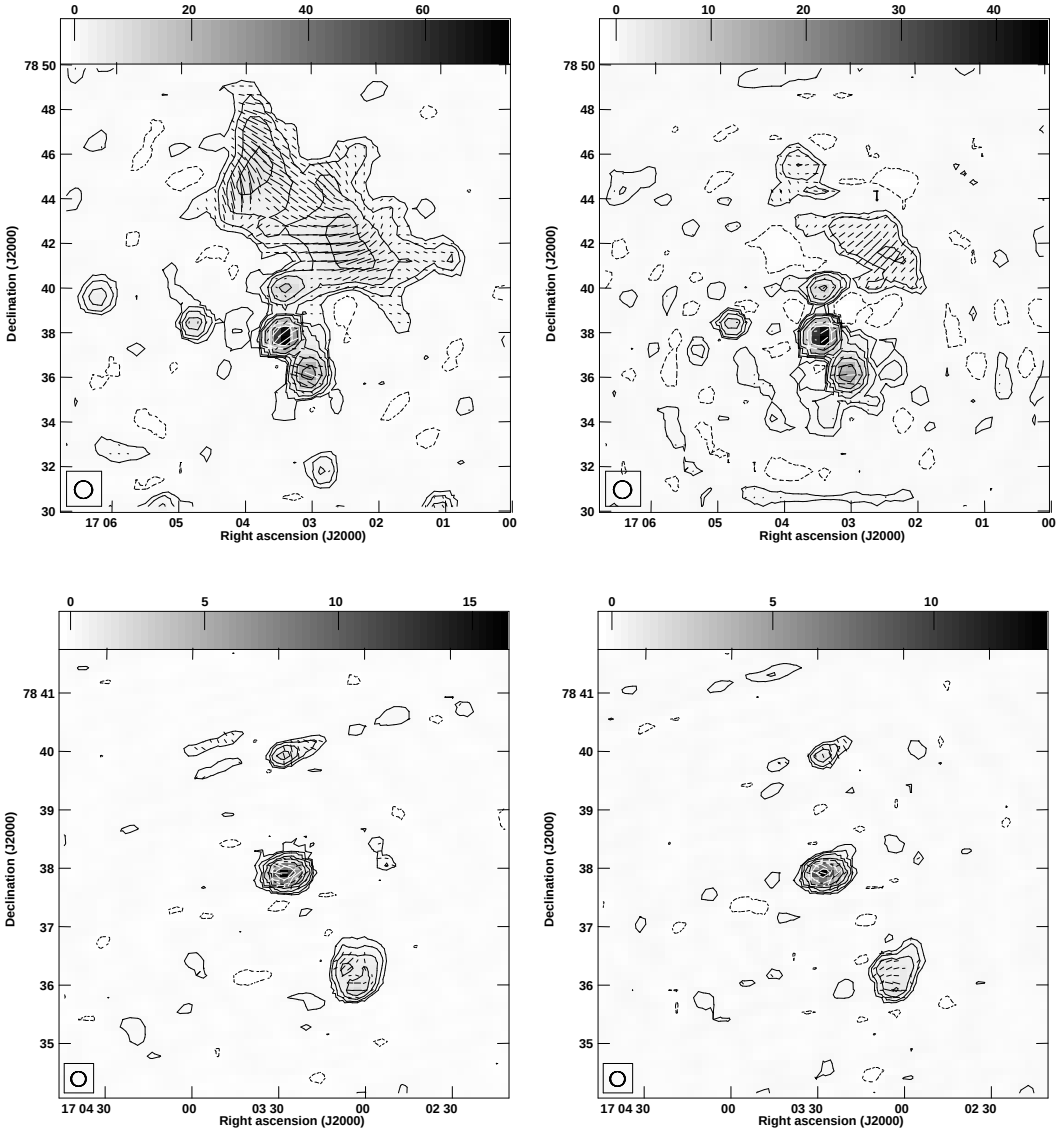

Figure 14: The total intensity images of Abell 2256 with the polarization vectors. All contours are drawn at $(-3, 3, 6, 12, 24, 48, 96, 192)$ times the rms level. *Top left*: The image of 2051 MHz. The rms level is 201.9 μJy beam^{-1}, and the telescope beam size is $47\overset{''}{.}0 \times 47\overset{''}{.}0$. *Top right*: The image of 3563 MHz. The rms level is 111.9 μJy beam^{-1}, and the telescope beam size is $47\overset{''}{.}0 \times 47\overset{''}{.}0$. *Bottom left*: The image of Source A, Source B, and Source C in Abell 2256 at 8051 MHz. The rms level is 48.4 μJy beam^{-1}, and the telescope beam size is $15\overset{''}{.}1 \times 15\overset{''}{.}1$. *Bottom right*: The image of Source A, Source B, and Source C in Abell 2256 at 9947 MHz. The rms level is 50.3 μJy beam^{-1}, and the telescope beam size is $15\overset{''}{.}1 \times 15\overset{''}{.}1$.

In the bottom left and bottom right panels in Figure 14, we show the total 8051 MHz and 9947 MHz intensity images of Sources A, Source B, and Source C in Abell 2256 with the polarization vectors, respectively. We drew the polarization vectors when the polarization intensity is larger than $3\sigma_{\rm P}$. Significant polarized radio emission is detected from Source A. We also see the polarization vectors in the Source B and Source C but this polarization intensity is not accurate because of insufficient sensitivity. For instance, the polarized intensity (0.152 mJy beam^{-1}) is smaller than $3\sigma_{\rm I}$ significance (0.159 mJy beam^{-1}) for a pixel (RA, Dec: $17^{\rm h}03^{\rm m}07\overset{\rm s}{.}8$, $78^\circ36'17\overset{''}{.}8$) in the Source B, and the polarized intensity (0.126 mJy beam^{-1}) is smaller than $3\sigma_I$ significance (0.145 mJy beam^{-1}) for a pixel (RA, Dec: $17^{\rm h}03^{\rm m}28\overset{\rm s}{.}1$, $78^\circ39'56\overset{''}{.}2$) in the Source C at 8051 MHz. In other X-band images, the Source A, Source B, and Source C are detected in the Stokes I above $3\sigma_{\rm I}$ significance but the radio relic is outside the field of views.

4.2. Total Intensity of the Radio Relic

We estimated the total 2051 MHz flux density in the whole region of the radio relic, which is 286 mJy. For estimating the total 2051 MHz flux density, we used the image of the Stokes I at 2051 MHz convolved with the telescope beam size of $47\overset{''}{.}0$. In this image, we integrated the pixels where the surface brightness is above $3\sigma_{\rm I}$ significance on the radio relic. If we consider that the total 1369 MHz flux density of the radio relic is 462 mJy (Clarke & Ensslin, 2006) and adopt the spectral index of $\alpha = -0.81$ (van Weeren et al., 2012), the total 2051 MHz flux density in the whole region of the radio relic should be 330 mJy. Therefore, the total 2051 MHz flux density of 286 mJy observed with JVLA C array configuration is smaller than the expected total 2051 MHz flux density by ~ 13 %. We note that the total 2051 MHz flux density of 286 mJy is not subtracted from the flux density of other radio sources such as the tail of Source C, whereas the total 1369 MHz flux density of 462 mJy which was used in predicting the total flux density of 2051 MHz is subtracted from the flux of other radio sources, so that the total 2051 MHz flux density of the radio relic observed with JVLA C array configuration is smaller than 286 mJy.

We also estimated the upper limit of the total 2051MHz flux density in the whole region of the radio halo, which is ~ 49 mJy. As we have shown in Figure 13, we did not detect the emission from the radio halo above $3\sigma_{\rm I}$ significance at 2051 MHz in our JVLA observations. For estimating the upper limit to the total 2051 MHz flux density, we assumed that the radius of the radio halo emission is $\sim 6\overset{'}{.}1$ (Clarke & Ensslin, 2006) and the upper limit of the surface brightness is 606 μJy beam^{-1} (10.296×10^{-23} W m^{-2} Hz^{-1} sr^{-1})

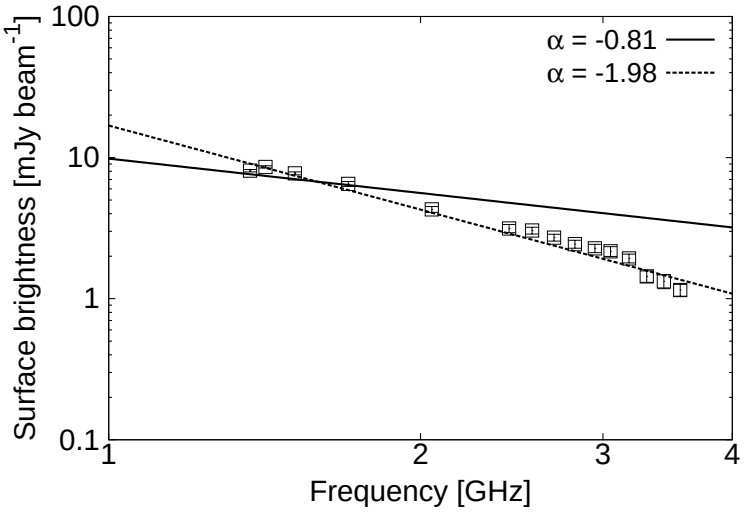

Figure 15: Example of the spectral energy distribution (from Ozawa et al., 2015). Open squares show the observed surface brightness for a pixel (RA, Dec: $17^{\rm h}02^{\rm m}51\overset{\rm s}{.}9$, $+78^\circ42'26\overset{''}{.}7$) in the radio relic. The solid line represents an extrapolation of the spectrum from the surface brightness between 1369 MHz to 2051 MHz with the spectral index of $\alpha = -0.81$. The dashed line represents a measured spectral index of $\alpha = -1.98$ from the surface brightness between 1369 MHz to 3563 MHz.

which corresponds to the $3\sigma_{\rm I}$ significance at 2051 MHz. If we consider that the total 1369 MHz flux density of the radio halo is 103 mJy (Clarke & Ensslin, 2006) and adopt the spectral index of $\alpha = -1.1$ (van Weeren et al., 2012), the total 2051 MHz flux density in the whole region of the radio halo should be ~ 66 mJy. Therefore, the estimated total 2051 MHz flux density of 49 mJy observed with JVLA C array configuration is smaller than the expected total 2051 MHz flux density by ~ 26 %.

In Figure 15, we show an example of the SED for a pixel (RA, Dec: $17^{\rm h}02^{\rm m}51\overset{\rm s}{.}9$, $+78^\circ42'26\overset{''}{.}7$) in the radio relic, where the SED is made from the images of the Stokes I convolved with the telescope beam size of $47\overset{''}{.}0$. We found that the measured spectral index from the surface brightness between 1369 MHz to 3563 MHz is $\alpha \sim -1.98$ (the dashed line of Figure 15), whereas the known spectral index from the total flux density of the whole region of the radio relic between 63 MHz to 1369 MHz is $\alpha = -0.81$ (van Weeren et al., 2012). If we extrapolate the surface brightness from the observed results in 1369 MHz to 2051 MHz with the spectral index of $\alpha = -0.81$, the observed surface brightness at frequency above 2 GHz is smaller than the extrapolated surface brightness

(the solid line of Figure 15). We will discuss the missing flux of the radio relic and radio halo in Section 5.1.

4.3. Fractional Polarization

We calculated the fractional polarization for the radio relic, Source A, and Source B, since significant polarized radio emission have been detected from these sources at S-band (see Section 4.1). We used the images of Stoke I and polarization intensity at the L and S band, and the S and X band convolved with the telescope beam size of $47''.0$ and $15''.1$, respectively, in order to analyze the radio relic and individual polarized radio sources. We calculated the fractional polarization only in pixels where the surface brightnesses of the Stokes I, Q, and U are all above 3σ significance.

In Figure 16, we show the fractional polarization spectra of the radio relic (open squares), Source A(open circles), and Source B (open triangles). Each data point represents the spatial average of the fractional polarization for the pixels within each emitting region. For the radio relic, since the emitting region of the radio relic at 3563 MHz is smaller than that at 2051 MHz by factor of ~ 0.37 (Section 14), we used the data of the region where the polarized radio emission is detected at 3563 MHz (the dashed frame region in Figure 13). The number of pixels in this region is 70 pixels. We plotted the data which satisfy the criteria that the fractional polarization was obtained with at least 3 pixels within each emitting region in each frequency. The error bars indicate the standard deviation of the fractional polarization for the pixels.

We found that the averaged fractional polarization of the radio relic decreases from ~ 35 % to ~ 20 % as the frequency decreases from ~ 3.5 GHz to ~ 3 GHz. Then, the averaged fractional polarization is nearly constant between 3 GHz to 1.37 GHz. We also plotted the fractional polarization of the brightest part of the radio relic observed with Westerbork Synthesis Radio Telescope (WSRT) at 350 MHz (Brentjens, 2008), which is less than 1 % (filled square). Therefore, the averaged fractional polarization in the field toward the radio relic varies twice, above ~ 3 GHz and between 0.35 to 1.37 GHz, and has step-like variations. In contrast, the averaged fractional polarization of Source A and Source B did not show the step-like variations, and has constant values of ~ 3 % and ~ 6 %, respectively. We will discuss the step-like variations of the averaged fractional polarization of the radio relic in Section 5.5.

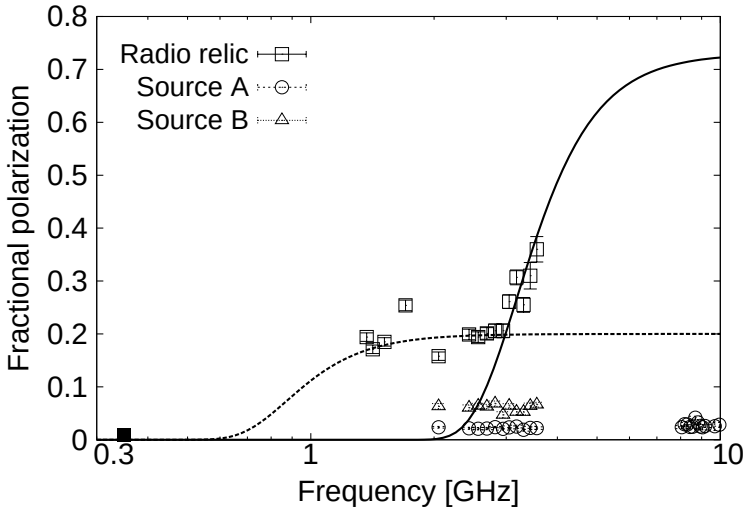

Figure 16: The averaged fractional polarization spectra of the radio relic (open squares), Source A (open circles), Source B (open triangles). The filled square at the bottom-left is the fractional polarization of the brightest part of the radio relic observed with the WSRT at 350 MHz (Brentjens, 2008). The lines show the Burn's law defined in equation (45) with $p_0 = 0.73$, $\sigma_{\rm RM} = 80$ rad m^{-2}(solid line) and $p_0 = 0.2$, $\sigma_{\rm RM} = 6$ rad m^{-2}(dashed line).

4.4. Faraday Rotation Measure

We created the RM distribution maps using the equation (31)

$$\chi = \chi_0 + \chi_{\rm F}$$

and equation (32)

$$\chi_{\rm F} = RM\lambda^2,$$

considering the nπ ambiguity. If we assume that the observed polarization angles and square wavelengths satisfy the linear relationship, then the observed data can be fitted with the least squares method, and the standard deviation of the observed data from the best fit line is the minimum value. Hence, we can avoid the effect of the nπ ambiguity by adding nπ to the polarization angles and then finding the minimum standard deviation.

We used the images of polarization angles at the L and S bands, and the S and X bands convolved with the telescope beam size of $47\farcs0$ and $15\farcs1$, respectively, to analyze the radio relic and individual polarized radio sources. We calculated the RM only in

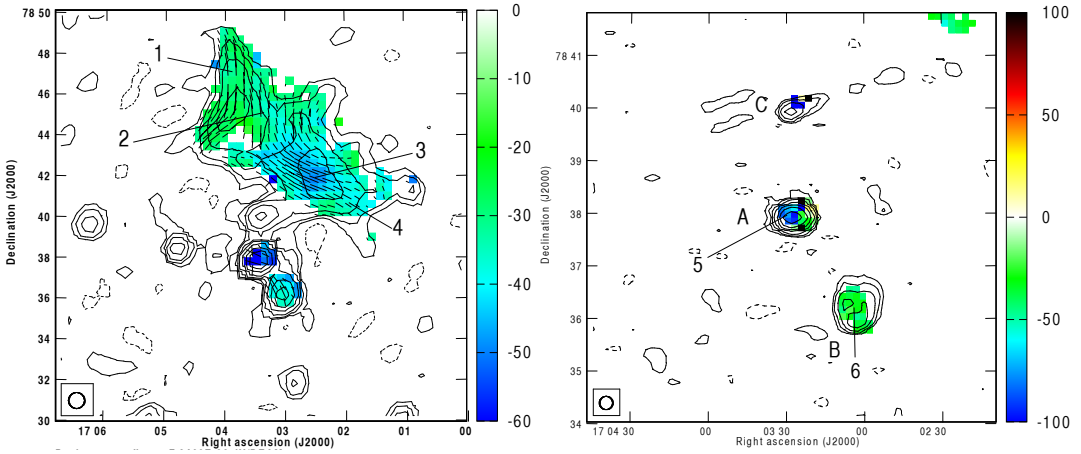

Figure 17: The RM distribution maps of Abell 2256 overlaid with contours of total intensity in the JVLA C array configuration (from Ozawa et al., 2015). *Left panel*: The RM distribution map made from the polarization angles at the L and S-band convolved with the telescope beam size of $47\overset{''}{.}0$. Contours of the total 2051 MHz flux density are drawn at $(-3, 3, 6, 12, 24, 48, 96, 192) \times 201.9$ μJy beam^{-1}, corresponding to a surface brightness of $(3.432 \times 10^{-23}$ W m^{-2} Hz^{-1} sr$^{-1})$. The vectors represent the intrinsic B-vectors obtained from ϕ_0. *Right panel*: The RM distribution map made from the polarization angles at the S and X band convolved with the telescope beam size of $15\overset{''}{.}1$. Contours of the total 8051 MHz flux density are drawn at $(-3, 3, 6, 12, 24, 48, 96, 192) \times 48.4$ μJy beam^{-1}, corresponding to a surface brightness of $(7.976 \times 10^{-23}$ W m^{-2} Hz^{-1} sr$^{-1})$.

the pixels which satisfy the following conditions: the surface brightness of the Stokes I, Q, and U are all above 3σ significances, and the pixels satisfying the first condition are available from at least 4 frequencies.

In Figure 17, we show the RM distribution maps of Abell 2256 overlaid with contours of the total intensity in the JVLA C array configuration. The vectors shown in the left panel represent the intrinsic B-vectors obtained from χ_0 in equation (31). We can see that the RM of the radio relic and Source B have flattened RM distributions, but the RM of the Source A is not flattened. We also calculated the average, $\langle \mathrm{RM} \rangle$, and the standard deviation, σ_{RM}, for the RM within the emitting region of the radio relic, Source A, and Source B. We show our results and the results reported by Clarke & Ensslin (2006) simultaneously in Table 4. Our results indicate that the $\langle \mathrm{RM} \rangle$ and σ_{RM} for the radio relic and Source B are broadly consistent with the result for the radio relic

Table 4: The average and standard deviation of RM (Ozawa et al., 2015).

Target	$\langle \mathrm{RM} \rangle^*$ (rad m^{-2})	$\sigma_{\mathrm{RM}}{}^*$ (rad m^{-2})	reference
Relic	-44	7	Clarke & Ensslin (2006)
Relic	-34.5	6.2	this work
Source A	-24.9	65.5	this work
Source B	-34.1	10.5	this work

* $\langle \mathrm{RM} \rangle$ and σ_{RM} are the average and standard deviation of RM, respectively.

reported by Clarke & Ensslin (2006). In contrast, the Source A has smaller $\langle \mathrm{RM} \rangle$ and larger σ_{RM} compared to the other sources. We considered that this could be related to the magnetic field fluctuations in the cluster because the simulated $|\langle \mathrm{RM} \rangle|/\sigma_{\mathrm{RM}}$ ratio depends only on magnetic field power spectrum slope and it has considerable scatter (Murgia et al., 2004).

In order to verify the linearity of the χ with λ^2, we created the plot for the χ–λ^2 relations toward the radio relic, Source A, and Source B. In Figure 18, we show the sample plots of the polarization angle χ against λ^2 for different locations in Abell 2256. Each number of bottom left corner represents the locations described in Figure 17. We confirmed that the linearity is roughly satisfied for the radio relic, Source A, and Source B. We can also see the RM from the Source C but we did not use these RM since the polarized radio emission of the Source C is not significant (Section 4.1).

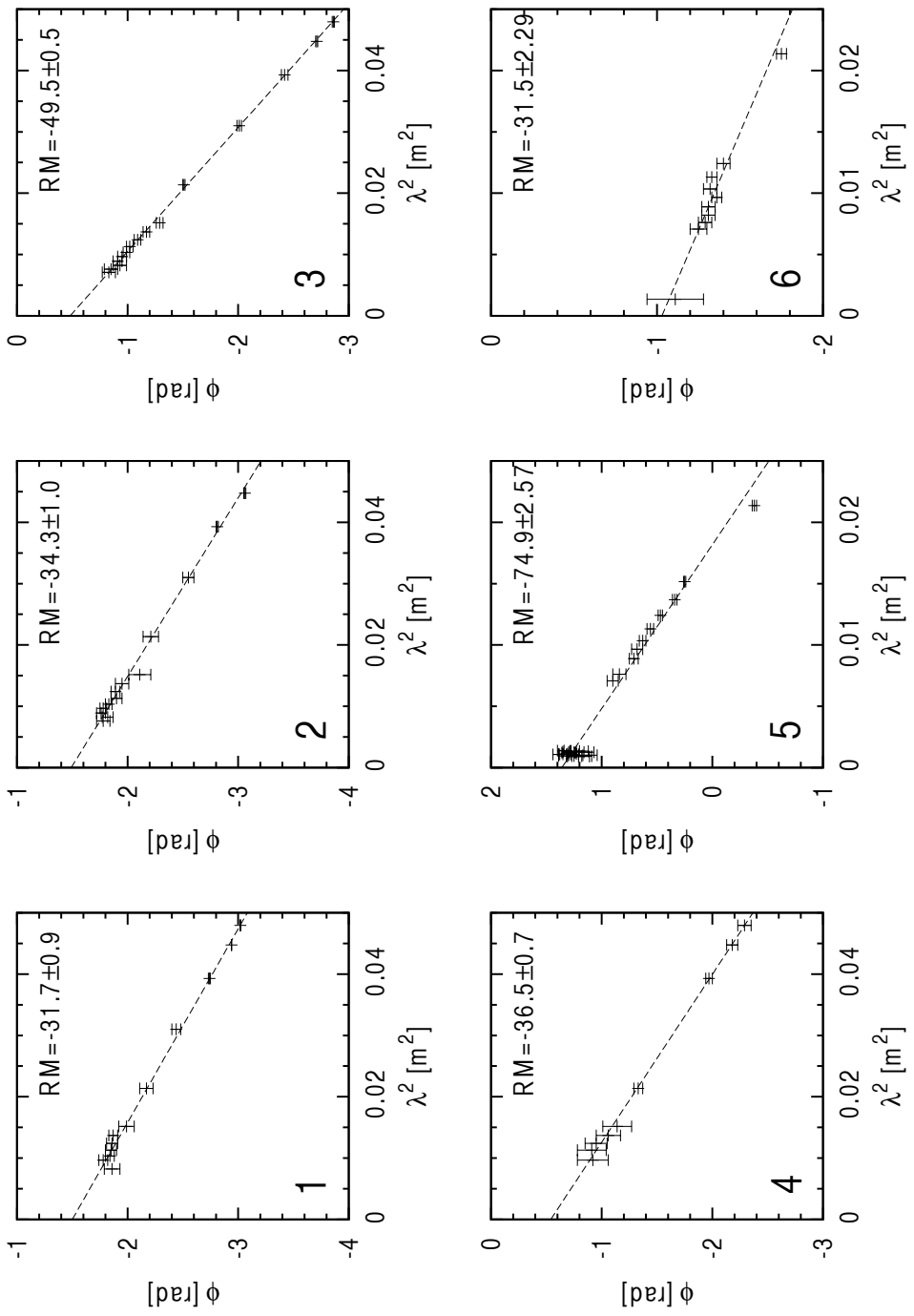

Figure 18: Sample plots of the polarization angle χ against λ^2 for different locations in Abell 2256 (from Ozawa et al., 2015). Each location is shown in Figure 17.

5. Discussion

We will discuss the magnetic field properties of Abell 2256 based on our results: radio images, total intensity, fractional polarization, and rotation measure. Especially, we used the depolarization models and Faraday tomography in order to reveal the magnetic field structures along the line of sight toward the radio relic. These measurement techniques can be used when the multiple frequency observation is performed such as our JVLA observations, because both techniques require many samples of the polarization intensity with frequency. The depolarization models would support to interpret the FDF obtained with the Faraday tomography.

5.1. Missing Flux of the Diffuse and Extended Radio Sources

As we have shown in Section 4.2, the total 2051 MHz flux density in the whole region of the radio relic in Abell 2256 was estimated to be 286 mJy, which is smaller than the expectation of 330 mJy extrapolated from the total 1369 MHz flux density and the spectral index of $\alpha = 0.81$. We did not find such decline of the flux density in the SED between 63 to 10450 MHz (Trasatti et al., 2015). We also found that the estimated upper limit of the total 2051 MHz flux density of the radio halo of ~ 49 mJy assuming the radius of the emitting region and the upper limit of the surface brightness of the radio halo is smaller than the expectation of ~ 66 mJy extrapolated from the total 1369 MHz flux density and the spectral index of $\alpha = 1.1$.

We considered that the missing flux is caused by the largest angular scale (LAS). The LAS is a detection limit of the scales of the extended emission in interferometry, and it is defined as $\theta_{\rm LAS} \sim \lambda / D_{\rm min}$, where $D_{\rm min}$ represents the shortest baseline length (Taylor et al., 1999). We can not detect the extended emission which has a scale larger than the LAS of the interferometer. For instance, if we consider that there are uniform extended emission on the all sky, then the visibility of the emission is delta function on the origin of uv plane. Since an antenna pair cannot make the 0 separation distance and we cannot obtain the visibility on the origin of uv plane, the reconstructed image should not contain the uniform extended emission.

In Table 5, we show the scales of the LASs at 1.5, 3.0, 6.0, and 10.0 GHz in the JVLA. The LASs at 1.5 and 3.0 GHz are $970''$ and $490''$, respectively, whereas the scales of the major axis of the radio relic and halo are $1014''$ and $732''$ on the sky (Clarke & Ensslin, 2006). Therefore, we could not detect the part of the radio relic due to the LAS.

This possibility is also supported by single dish radio observations. In the single dish radio observations, the LAS problem does not occur, and the observed flux density

Table 5: Largest Angular Scale of the JVLA (arcsec).[8]

Band	Array configuration			
(GHz)	A	B	C	D
1.5 (L-band)	1.3	4.3	14	46
3.0 (S-band)	0.65	2.1	7.0	23
6.0 (C-band)	0.33	1.0	3.5	12
10.0 (X-band)	0.20	0.60	2.1	7.2

should satisfy the spectral index of the radio relic. Owen (1975) and Haslam et al. (1978) estimated that the total 2695 MHz flux density in the entire area of Abell 2256 are 570 and 666 mJy with Green Bank and Effelsberg, respectively, and these values satisfy the spectral index of the radio relic of $\alpha = -0.72$ (Brentjens, 2008). Note that the most of the flux density in the entire area of Abell 2256 originates from the radio relic and intrinsic radio sources in this band because the contribution of the radio halo is estimated to be $\sim$ 20mJy ($\sim$ 3% of the 2563 MHz flux in the entire area of Abell 2256) with the spectral index of the radio halo of $\alpha = -1.61$ (Brentjens, 2008).

We can also consider another possibility that the decline would be a cutoff of cosmic-ray electrons at high energies. However, since the effect of the missing flux could be significant, we could not argue the possibility of the energy cutoff.

5.2. Magnetic Field Strengths in the Radio Relic

We estimated the total magnetic field strength of the radio relic in Abell 2256 from the synchrotron emission assuming the equipartition between the energy densities of the cosmic-ray particles and the energy densities of the magnetic fields. In order to calculate the magnetic field strength, we used revised equipartition formula (equation 30)

$$B_{\rm t} = \left\{ \frac{4\pi(2\alpha+1)(\mathbf{K_0}+1) I_\nu E_{\rm p}^{1-2\alpha} (\nu/2c_1)^\alpha}{(2\alpha-1)c_2(\alpha) l c_4(i)} \right\}^{1/(\alpha+3)}$$

because the classical minimum energy formula is formally incorrect (Beck & Krause, 2005).

For the parameters of the revised equipartition formula, we adopted following values: $I_\nu = 6.27 \times 10^{-19}$ erg s^{-1} cm^{-2} Hz^{-1} sr^{-1}, $\nu = 2051 \times 10^6$ Hz, $\alpha = 0.81$, $l = 25$ and 1125 kpc, and i =45°. I_ν is the averaged 2051 MHz intensity of the radio relic region

[8] https://science.nrao.edu/facilities/vla/docs/manuals/oss/performance/resolution

where the averaged fractional polarization was measured (the dashed frame region in Figure 13). Since we could not measure the accurate spectral index of the radio relic from our JVLA data due to the missing flux (see Section 4.2), we adopted the spectral index measured by van Weeren et al. (2012). Since we do not know the path length of the synchrotron emission in the radio relic, we expect the value from the width of the filament in the radio relic and largest linear scale of the radio relic. Owen et al. (2014) found that the radio relic in Abell 2256 includes several radio filaments, and the shape of individual filaments suggest that the radio relic is at least 25 kpc thick. We therefore adopted $l = 25$ kpc as the minimum path length. We also adopted the maximum path length from the largest linear scale $l = 1125$ kpc of the radio relic which is obtained by Clarke & Ensslin (2006). For the inclination i, we assumed a mid value.

We obtained the total magnetic field strengths of the radio relic as ~ 5.0 μG with $l = 25$ kpc and ~ 1.8 μG with $l = 1125$ kpc. Since the ambiguity of the path length l was too large, we did not show the results of the error propagation. These values calculated from revised equipartition formula are roughly consistent with the field strengths of the intracluster space $B = 1.5$–3.2 μG and $B = 3.3$–8.9 μG obtained with the classical and hadronic minimum energy condition, respectively (Clarke & Ensslin, 2006). Hence, the magnetic field strength in the radio relic is micro-Gauss order, roughly corresponding to the field strengths of the radio halo.

From the fractional polarization p, we can estimate the degree of uniformity of the magnetic fields f within the telescope beam (Segalovitz et al., 1976);

$$p = p_0 \left[1 + \frac{(1-f)\pi^{1/2}\Gamma[(p_\mathrm{e}+5)/4]}{2f(\sin\theta)^{(p_\mathrm{e}+1)/2}\Gamma[(p_\mathrm{e}+7)/4]} \right]^{-1}, \tag{71}$$

where Γ is the gamma function, p_0 is the intrinsic fractional polarization, and θ is the angle between the line of sight and the uniform magnetic fields.

From the degree of uniformity of the magnetic fields, the ratio between the strengths of the uniform magnetic fields and total magnetic fields is given by

$$\frac{B_\mathrm{u}}{B_\mathrm{t}} = f^{1/(p_\mathrm{e}-1)}, \tag{72}$$

and the random magnetic field strength B_r is given by

$$B_\mathrm{r} = (B_\mathrm{t}^2 - B_\mathrm{u}^2)^{1/2}, \tag{73}$$

(Beck, 1982).

We calculated the degree of uniformity of the magnetic fields f using equation (71), and the uniform and random magnetic field strengths using equations (72) and (73). In order to avoid the effect of the depolarization within the foreground sources, we used the fractional polarization of high frequency, which is $p = 0.36$ at 3563 MHz. Since we do not know the angle of θ, we assumed the mid value of θ =45°. We obtained the degree of uniformity of $f \sim 0.56$, uniform magnetic field strengths ~ 3.7 μG with $l = 25$ kpc and ~ 1.3 μG with $l = 1125$ kpc, and the random magnetic field strength is ~ 3.4 μG with $l = 25$ kpc and ~ 1.2 μG with $l = 1125$ kpc.

The obtained degree of uniformity of the magnetic fields indicate that there are uniform magnetic fields as well as random magnetic fields in the radio relic. However, the degree of uniformity of $f \sim 0.56$ could be a larger value because equation (71) does not take into account the effect of the depolarization. It seems that there are ordered intrinsic magnetic fields over the telescope beam size of ~ 52 kpc in the left panel of Figure 17 against $f \sim 0.56$. This could suggest that there are random magnetic fields along the line of sight toward the radio relic in Abell 2256 causing depolarization.

5.3. Magnetic Field Strengths in the Intracluster Space

We estimated the magnetic field strengths in the intracluster space of Abell 2256. As we have introduced in Section 1.2.4, the polarized radio emission emitted from the radio source in the back ground of the clusters are affected by the Faraday rotation of the cluster. We can therefore deduce the magnetic field strength toward the polarized radio sources, Source A and Source B, using equation (37):

$$\sigma_{\rm RM} = \frac{KBn_0 r_{\rm c}^{1/2} \Lambda_{\rm B}^{1/2}}{(1 + r^2/r_{\rm c}^2)^{(6\beta-1)/4}} \sqrt{\frac{\Gamma(3\beta - 0.5)}{\Gamma(3\beta)}}.$$

For the parameters of equation (37), we adopted the values shown in Table 6, and we also show the results in Table 6. Since we do not know the length of Λ_B, we assumed 5 or 20 kpc according to the dynamo theory (Cho & Ryu, 2009). We found that the magnetic field strength toward Source A is $B = 1.26$ μG with $\Lambda_B = 5$ kpc and $B = 0.63$ μG with $\Lambda_B = 20$ kpc, and the magnetic field strength toward Source B is $B = 0.21$ μG with $\Lambda_B = 5$ kpc and $B = 0.11$ μG with $\Lambda_B = 20$ kpc.

The magnetic field strengths obtained with different methods show the different strengths in the cluster. For instance, the magnetic field strengths is 0.45 μG with equipartition in Coma cluster (Giovannini et al., 1993), whereas the strength is 7 μG with RM (Feretti et al., 1995). The strengths obtained with RM are roughly an order of magnitude

Table 6: Parameters for the magnetic field strengths of intracluster space (Ozawa et al., 2015).

Source	K	$\sigma_{\rm RM}$ (rad m^{-2})	$n_0{}^*$ (10^{-3} cm^{-3})	$r^\dagger$ (kpc)	$r_{\rm c}{}^*$ (kpc)	β^*	$\Lambda_{\rm B}$ (kpc)	B (μG)
Source A	441	65.5	2.6	7.2	587	0.914	20–5	0.63–1.26
Source B	441	10.5	2.6	133.7	587	0.914	20–5	0.11–0.21

Reference: *Chen et al. (2007); †Ebeling et al. (1998).

higher than that obtained with equipartition. We can consider several reasons. Firstly, the equipartition magnetic field strengths rely on several assumptions (see Section 1.2.2). Secondly, equipartition gives the averaged magnetic field strength of the region where the diffuse radio emission exist, whereas the RM gives the average magnetic field strengths along the line of sight, which depends on the distribution of the magnetic fields and ICM in the cluster. If the magnetic field strengths relate to the electron densities, RMs observed in the cluster center would be heavily weighted (Dreher et al., 1987). For instance, in Abell 119, Dolag et al. (2001) found that the magnetic field scales as $B \propto n_{\rm e}^{0.9}$. Thirdly, most of the polarized radio sources are located in the cluster center and identified with a cD galaxy (Carilli & Taylor, 2002). Existence of the compression of the magnetic fields and ICM around the polarized radio sources could also produce the RM enhancement (Bicknell et al., 1990). Finally, the magnetic field strength would depend on the dynamical history and the location within the cluster (Govoni & Feretti, 2004; Ferrari et al., 2008).

However, our estimation of the magnetic field strengths toward Source A and Source B, $B \sim 0.11$–1.26, is smaller than the magnetic field strength obtained with the minimum and hadronic minimum energy condition with the emission of the radio halo, which are $B = 1.5$–3.2 μG and $B = 3.3$–8.9 μG, respectively (Clarke & Ensslin, 2006). We have still argued the cause of this values. If the telescope beam size is larger than the coherent length of the magnetic fields, then the value of $\sigma_{\rm RM}$ is smaller than that of the case where the telescope beam size is smaller than the coherent length of the magnetic fields. The telescope beam size of our JVLA observation could be insufficient for the magnetic fields in Abell 2256.

5.4. Contribution of the Milky Way Fields

As we have introduced in Section 1.2.4, if there are ideal magnetic fields along the line of sight, the distribution of RM becomes a Gaussian with zero mean. In Table 4, we

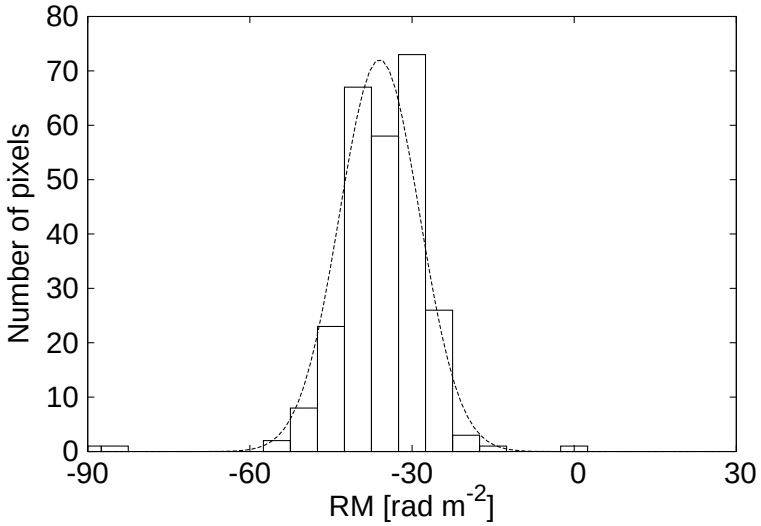

Figure 19: Histogram of the RM (from Ozawa et al., 2015). We obtained 355 pixels in the RM map of Abell 2256. RM was binned with a width 5 rad m^{-2}. Dashed line represents the result of Gaussian fitting with $\mu = -36$ rad m^{-2} and $\sigma = 7.4$ rad m^{-2}.

can see a shift of the RM from 0 rad m^{-2} to about -30 rad m^{-2}. In Figure 19, we show the histogram of RMs in Abell 2256. The number of pixels is 355 and was obtained from Figure 17. The histogram indicates that the centre is at around -36 rad m^{-2}.

We considered that the cause of the shift is the contribution of the Milky Way fields. For estimating the contribution of the Milky Way fields to the Abell 2256 fields, we used RM catalogue shown in Figure 6 (Taylor et al., 2009), and examined the RM values of 28 extragalactic polarized radio sources within 6° around Abell 2256 (Table 7). We averaged the RM values, and we found that the averaged RM is -30.0 rad m^{-2} with the standard deviation of 16.7 rad m^{-2}. The averaged RM of -30.0 rad m is broadly consistent with the means of RM for the radio relic, Source A, and Source B (see Table 4). Therefore, we conclude that the cause of the shift of RM would be the galactic contribution.

5.5. Magnetic Field Structure toward the Radio Relic

As we have shown in Figure 16, the fractional polarizations of the radio relic in Abell 2256 show the step-like variation. We predicted that the variation of the fractional polarization of the radio relic is caused by the beam depolarization, as introduced in Section

Table 7: 28 extragalactic polarized radio sources within 6° around Abell 2256.

Right Ascension (J2000)	Declination (J2000)	RM (rad m^{-2})	σ_{RM} (rad m^{-2})
$16^h20^m3^s.83$	$77°24'58''.4$	-23.8	14
$16^h26^m27^s.8$	$76°24'48''.5$	-45.3	16.2
$16^h28^m21^s.91$	$81°0'7''.1$	-18.1	14
$16^h47^m6^s.39$	$79°6'18''.1$	-23.7	9
$16^h48^m43^s.16$	$75°46'28''.7$	12.7	7
$16^h50^m18^s.06$	$76°32'13''.6$	-16.8	18.5
$16^h50^m39^s.36$	$81°32'38''.6$	-55.2	10.2
$16^h51^m35^s.73$	$78°28'53''.5$	-13.7	2.5
$16^h54^m28^s.17$	$76°28'19''.6$	-20.8	3.7
$16^h57^m40^s.99$	$78°4'51''.1$	-16	13.6
$16^h58^m14^s.81$	$80°56'59''.8$	-36.8	14
$16^h59^m3^s.56$	$77°2'54''.6$	-27.3	14.3
$17^h0^m30^s.34$	$79°30'48''.1$	-26.6	11.5
$17^h1^m41^s.71$	$76°52'38''.7$	-61.3	14.1
$17^h5^m24^s.81$	$77°55'59''.8$	-36.3	9
$17^h5^m57^s.19$	$77°6'11''.6$	-18.9	7.2
$17^h6^m11^s.51$	$77°7'23''.7$	-20.2	4.4
$17^h7^m18^s.72$	$78°6'40''.2$	-27.5	7.8
$17^h10^m52^s.11$	$75°50'52''.4$	-32	10.6
$17^h12^m6^s.35$	$77°46'13''.6$	-54.8	11
$17^h14^m16^s.91$	$76°12'45''.4$	-27.2	5.4
$17^h23^m4^s.87$	$78°27'25''.8$	-42.2	13.6
$17^h23^m48^s.79$	$79°5'10''.9$	-30.8	9.3
$17^h25^m56^s.47$	$78°17'1''.8$	-37	12.6
$17^h27^m54^s.48$	$77°27'43''.5$	-15.1	16.8
$17^h42^m59^s.19$	$80°20'26''.8$	-18.8	15.9
$17^h43^m41^s.98$	$80°4'8''.0$	-40.1	4.3
$18^h0^m45^s.76$	$78°28'5''.0$	-66.5	0.9

Reference: Taylor et al. (2009).

1.2.5. Since the depolarizations have been studied analytically by Burn (1966), we fitted the function of the EFD in equation (45) with the observed fractional polarizations of the radio relic.

In Figure 16, the lines represent the function of the EFD. Obviously, the function cannot reproduce the observed fractional polarizations, whereas the histogram of RMs in Abell 2256 (Figure 19) shows the Gaussian distribution, indicating the beam depolarization induced by the random magnetic fields. This result indicates that the Burn's law assuming a single depolarization component is not enough to explain the step-like variation of the fractional polarization of the radio relic. We predicted that two depolarization components along the line of sight toward the radio relic produce the step-like variation of the fractional polarization.

5.5.1. Depolarization Models

We predicted the existence of two depolarization components along the line of sight toward the radio relic. In order to study the variation of the fractional polarization for two depolarization components along the line of sight, we carried out numerical simulations of beam depolarizations using simple random magnetic fields models.

We calculated the intensity of polarized radio emission which passed depolarization components. The depolarization component consist of many cells. Each cell at (x, y, z) on the three-dimensional orthogonal coordinate (X, Y, Z) has same cell size, uniform electron density, and uniform magnetic field strength with a single scale random direction. The number of cells are defined as ($N_{\rm X}$, $N_{\rm Y}$, $N_{\rm Z}$). We firstly considered both the EFD and IFD depolarization models with a single depolarization component. Both models should reproduce Burn's law.

In the EFD depolarization model, only a cell at $(x, y, N_{\rm Z})$ is emitted. From equation (38), complexed linear polarization of each cylinder at (x, y) is given by

$$P_{xy} = p_0 \epsilon e^{2i\chi_{xy}} \tag{74}$$

From equations (31), (32), and (33), the polarization angle of each cylinder at (x, y) is given by

$$\chi_{xy} = \chi_0 + 812 n_{\rm e} B_{\parallel} \Delta l N_{\rm Z} \lambda^2, \tag{75}$$

where Δl is the size of a cell. We can obtain the complexed liner polarization $P_{\rm EFD}$

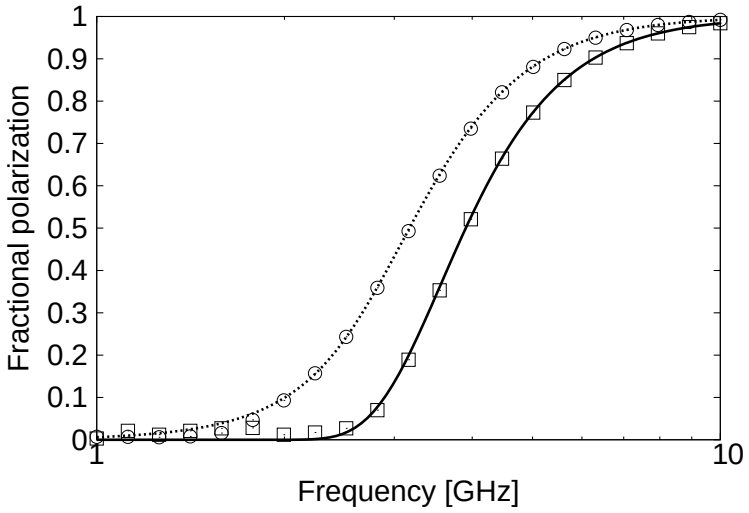

Figure 20: The fractional polarization spectra of the EFD and IFD depolarization models. Open squares and circles represent the EFD and IFD depolarization models with $p_0 = 1$ and $\sigma_{\rm RM} = 100$ rad m^{-2}, respectively. The solid and dashed line represent the Burn's law of the EFD and IFD with $p_0 = 1$ and $\sigma_{\rm RM} = 100$ rad m^{-2}, respectively.

through the $N_{\rm X} \times N_{\rm Y}$ cylinders as

$$P_{\rm EFD} = \sum_{x=1}^{N_{\rm X}} \sum_{y=1}^{N_{\rm Y}} P_{xy}. \tag{76}$$

In the IFD depolarization model, all cells at (x, y, z) is emitted. From equation (38), the complexed linear polarization of each cylinder at (x, y) is given by

$$P_{xy} = \sum_{z=1}^{N_{\rm Z}} p_0 \epsilon e^{2i\chi_{xyz}}. \tag{77}$$

From equations (31), (32), and (33), the polarization angle of each cylinder at (x, y) is given by

$$\chi_{xyz} = \chi_0 + 812 n_{\rm e} B_{\parallel} \Delta l \{N_{\rm Z} - (z-1)\} \lambda^2. \tag{78}$$

We can obtain the complexed linear polarization $P_{\rm IFD}$ through the $N_{\rm X} \times N_{\rm Y}$ cylinders

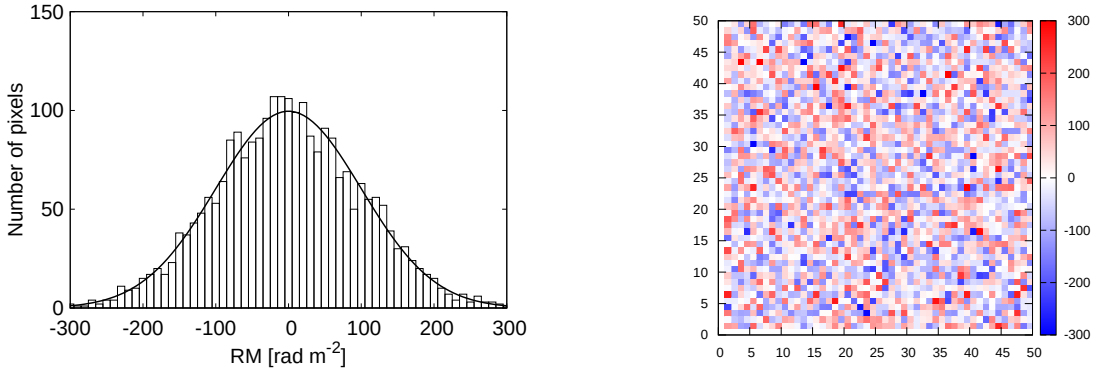

Figure 21: Histogram of the RM and RM distribution of the EFD depolarization model with $p_0 = 1$ and $\sigma_{\rm RM} = 100$ rad m^{-2}. *Left panel*: Histogram of the RM, binned with a width 10 rad m^{-2}. Dashed line represents the result of Gaussian fitting with $\mu = 0$ rad m^{-2} and $\sigma = 100$ rad m^{-2}. *Right panel*: RM distribution. Color represents the value of the RM.

as

$$P_{\rm IFD} = \sum_{x=1}^{N_{\rm X}} \sum_{y=1}^{N_{\rm Y}} P_{xy}. \tag{79}$$

The polarization intensity is expressed as the absolute value of both the $P_{\rm EFD}$ and $P_{\rm IFD}$.

In the EFD and IFD depolarization models, we have the following parameters: the magnetic field strength B, the electron density $n_{\rm e}$, the cells size Δl, the number of cells in the directions of the X, Y and Z axes ($N_{\rm X}$, $N_{\rm Y}$, $N_{\rm Z}$), and the polarization intensity.

In Figure 20, we show the sample plot of our EFD and IFD depolarization models with $p_0 = 1$ and $\sigma_{\rm RM} = 100$. Our EFD and IFD depolarization model was nicely fitted with the function of Burn's law of the EFD and IFD with $p_0 = 1$ and $\sigma_{\rm RM} = 100$, and we therefore confirmed the suitability of the depolarization models. Figure 21 shows the histogram of the RM and RM distribution of the EFD depolarization model. We can also confirm the Gaussian distribution of the RM, reflecting the simplest ideal case of the magneto-ionic component.

Next, we considered the two depolarization components models, EFD+EFD and IFD+IFD models (Figure 22). In each model, we put the depolarization components along the line of sight from the observer in the following orders ;

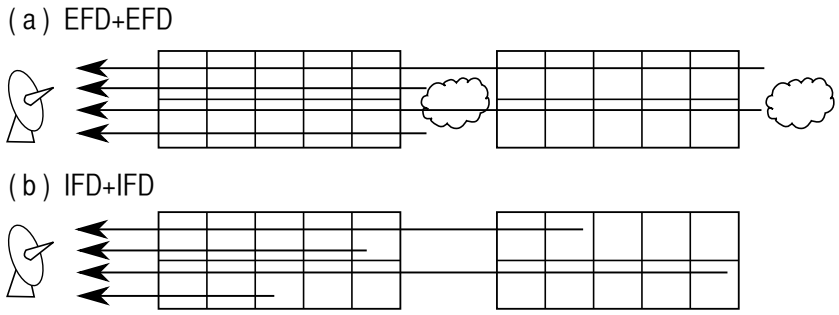

Figure 22: Schematic illustration of the depolarization models (from Ozawa et al., 2015). (a) The depolarization model of EFD+EFD, which has two non-emitting depolarization components with two polarized radio sources. (b) The depolarization model of IFD+IFD, which has emitting two depolarization components.

- In the EFD+EFD model, we put the depolarization components in the order of a depolarization component, a polarized radio source, a depolarization component, and a polarized radio source.
- In the IFD+IFD model, we put the depolarization components in the order of an emitting depolarization component, and another emitting depolarization component.

Based on the calculation procedure of the single depolarization component model, we calculated both the EFD+EFD and IFD+IFD models. In the EFD+EFD model, the observed complexed linear polarization of each cylinder at (x, y) is given by

$$P_{xy} = P_{1xy} + P_{1+2xy}, \tag{80}$$

where the subscripts 1 and 2 indicate the foreside and backside depolarization component viewed from the observer, respectively, P_{1xy} is the intensity of the polarized radio emission emitted from the left cloud in Figure 22a, which is affected by the foreside depolarization component, and P_{1+2xy} is the intensity of the polarized radio emission emitted from the right cloud in Figure 22a, which is affected by the foreside and backside depolarization components, respectively. We substitute equation (74) into equation (80) as

$$P_{xy} = p_0 \epsilon e^{2i\chi_{1xy}} + p_0 \epsilon e^{2i\chi_{1+2xy}}. \tag{81}$$

From equation (75), the polarization angles χ_{1xy} and χ_{1+2xy} are written as

$$\chi_{1xy} = \chi_0 + 812 n_{\rm e1} B_{\parallel 1} \Delta l N_{Z1} \lambda^2 \tag{82}$$

and

$$\chi_{1+2xy} = \chi_0 + 812 (n_{\rm e1} B_{\parallel 1} N_{\rm Z1} + n_{\rm e2} B_{\parallel 2} N_{\rm Z2}) \Delta l \lambda^2, \tag{83}$$

respectively. From equation (76), we can obtain the complexed liner polarization $P_{\rm EFD+EFD}$ through the $N_{\rm X} \times N_{\rm Y}$ cylinders as

$$P_{\rm EFD+EFD} = \sum_{x=1}^{N_{\rm X}} \sum_{y=1}^{N_{\rm Y}} P_{xy}. \tag{84}$$

In the IFD+IFD model, the observed complexed linear polarization of each cylinder at (x, y) is given by

$$P_{xy} = P_{1xy} + P_{1+2xy}, \tag{85}$$

where P_{1xy} is the intensity of the polarized radio emission emitted from the left component in Figure 22b and P_{1+2xy} is the intensity of the polarized radio emission emitted from the right component in Figure 22b, respectively. We substitute equation (77) into equation (85) as

$$P_{xy} = \sum_{z_1=1}^{N_{Z1}} p_0 \epsilon e^{2i\chi_{1xyz_1}} + \sum_{z_2=1}^{N_{Z2}} p_0 \epsilon e^{2i(\chi_{1xy} + \chi_{2xyz_2})}. \tag{86}$$

where the second term on the right hand side indicates the intensity of the polarized radio emission emitted from the backside component, and χ_{1xy} and χ_{2xyz_2} are the contribution of the foreside and backside component, respectively. From equation (78), the polarization angles χ_{1xy}, χ_{1xyz_1}, and χ_{2xyz_2} are written as

$$\chi_{1xy} = 812 n_{\rm e1} B_{\parallel 1} \Delta l N_{Z1} \lambda^2, \tag{87}$$

$$\chi_{1xyz_1} = \chi_0 + 812 n_{\rm e1} B_{\parallel 1} \Delta l \{N_{\rm Z1} - (z_1 - 1)\} \lambda^2, \tag{88}$$

and

$$\chi_{2xyz_2} = \chi_0 + 812 n_{\rm e2} B_{\parallel 2} \Delta l \{N_{\rm Z2} - (z_2 - 1)\} \lambda^2, \tag{89}$$

respectively. From equation (79), we can obtain the complexed linear polarization

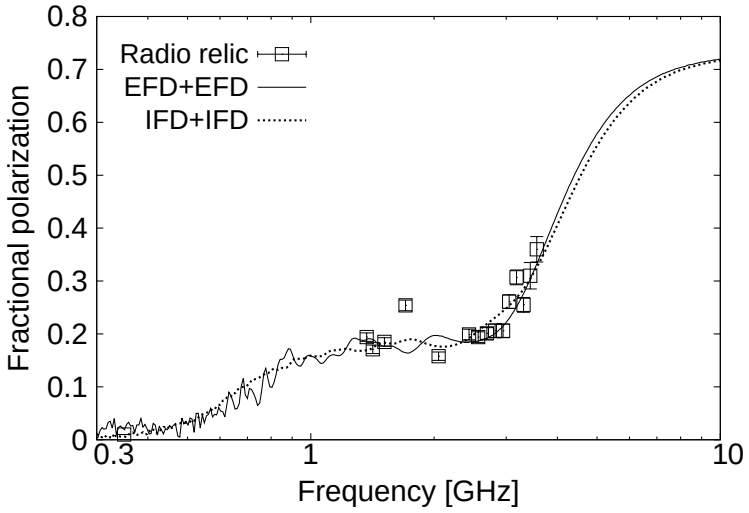

Figure 23: The fractional polarization spectra of the depolarization models (from Ozawa et al., 2015). The solid and dotted lines show the EFD+EFD model and IFD+IFD model, respectively. Open squares represent the observed fractional polarization of the radio relic (the dashed frame region in Figure 13).

$P_{\rm IFD+IFD}$ through the $N_{\rm X} \times N_{\rm Y}$ cylinders as

$$P_{\rm IFD+IFD} = \sum_{x=1}^{N_{\rm X}} \sum_{y=1}^{N_{\rm Y}} P_{xy}. \tag{90}$$

In order to calculate the above equations, we made both the EFD+EFD and IFD+IFD models with Fortran. In these models, we have the following parameters: the magnetic field strengths B_1 and B_2, the electron density $n_{\rm e1}$ and $n_{\rm e2}$, the spectral index α_1 and α_2, the number of cells in the direction of the X, Y, and Z axes ($N_{\rm X}$, $N_{\rm Y}$, $N_{\rm Z1}$) and ($N_{\rm X}$, $N_{\rm Y}$, $N_{\rm Z2}$), the ratio of the polarization intensity between the foreside and backside components, and the calculation points in the frequency domain. We will describe the details of the program in Appendix A.3.

In Figure 23, we show the best fit results for the two depolarization models. Each parameter is shown in Table 8. We can see the models which can nicely reproduce the fractional polarization of the radio relic. We confirmed that the two-component depolarization models can produce the step-like variation of the fractional polarization. Moreover, we found that the step-like variation of the fractional polarization can be produced in a situation where the $\sigma_{\rm RM}$ of the foreside depolarization component viewed

Table 8: Parameters for the Depolarization Models (Ozawa et al., 2015).

Model	Component	B [μG]	$n_{\rm e}$ [10^{-3} cm^{-3}]	Δl [kpc]	$N_{\rm X} \times N_{\rm Y}$ [kpc $\times$ kpc]	$N_{\rm Z}$ [kpc]	Intensity	$\sigma_{\rm RM}$ [rad m^{-2}]
EFD+EFD	foreside	0.2	1.0	1*	50 $\times$ 50*	600	1	3.2
	backside	2.3	3.0			600	3	111
IFD+IFD	foreside	0.2	1.0	5*	50 $\times$ 50*	500	1	4.1
	backside	2.3	3.0			600	3.5	164

* We assumed 50 $\times$ 50 kpc since the telescope beam size of $47''.0$ corresponds to $\sim$52 kpc.

from the observer has to be smaller than that of the backside depolarization component. Note that, since the telescope beam size of the image where the fractional polarization was measured is $47'.0 \times 47'.0$, we adopted 50 [kpc] $\times$ 50 [kpc] in $N_{\rm X} \times N_{\rm Y}$. Numerical simulation of the fractional polarization can take into account the telescope beam size, whereas the analytically Burn's law cannot take into account that one, and we also take into account the coherent length of the magnetic fields as Δl.

We could interpret the two depolarization components in our models as follows. The foreside depolarization component viewed from the observer may be the magneto-ionic plasma in the cluster or the Milky Way Galaxy. Since we do not have the data of the fractional polarization between 0.3 and 1 GHz, we do not identify the cause of the depolarization in this frequency range. The backside depolarization component would be the magneto-ionic plasma inside the radio relic because the fact that the fractional polarization of Source A and Source B near the radio relic does not show the step-like variation (see Figure 16).

Although we can reproduce the step-like variation of the fractional polarization of the radio relic using the two-component depolarization models, we should improve our depolarization model. For instance, filamentary structures exist in the radio relic (Clarke & Ensslin, 2006; Brentjens, 2008; Owen et al., 2014), and the filamentary structures could contribute to the observed fractional polarization.

5.5.2. Faraday Tomography

We also carried out Faraday tomography, which is introduced in section 1.2.6, in order to confirm the existence of the two depolarization components along the line of sight toward the radio relic. We applied QU-fitting method, which is developed by Ideguchi et al. (2014). In the QU-fitting method, we construct the FDF model with free parameters such as RM, assuming the distributions of the magnetic fields and polarized radio sources. Fitting the model Q and U data with the observed Q and U data, we find the best fit

Table 9: The reduced chi-square (RCS), the Bayesian information criterion (BIC), and best-fit values and 1-σ confidence regions for model parameters in the QU-fitting (Ozawa et al., 2015).

Model	RCS	BIC	ϕ	Amp.	χ_0	Width
Delta function	21.2	645.2	$-41.55^{0.745}_{-0.742}$	$0.42^{0.008}_{-0.008}$	$-0.55^{0.012}_{-0.012}$	
Gaussian	21.2	648.6	$-41.53^{0.736}_{-0.775}$	$0.42^{0.008}_{-0.008}$	$-0.55^{0.012}_{-0.011}$	$0.02^{0.736}_{-0.005}$
two Deltas	3.0	110.2	$-40.87^{0.626}_{-0.016}$	$21.23^{-1.118}_{-1.464}$	$0.12^{-0.003}_{-0.010}$	
			$-40.36^{0.649}_{-0.008}$	$21.17^{-1.149}_{-1.472}$	$-1.45^{-0.003}_{-0.010}$	
two Gaussian	2.2	93.3	$-49.32^{0.191}_{-1.003}$	$13.31^{1.019}_{0.779}$	$0.42^{-0.013}_{-0.051}$	$8.36^{1.727}_{-0.885}$
			$-48.14^{0.134}_{-1.032}$	$13.41^{1.011}_{0.764}$	$-1.15^{-0.012}_{-0.050}$	$8.70^{1.913}_{-0.733}$
Delta + Gaussian	2.6	100.9	$-50.35^{0.322}_{-1.162}$	$12.11^{-1.270}_{-1.555}$	$0.55^{0.069}_{0.045}$	
			$-49.38^{0.320}_{-1.066}$	$12.28^{-1.244}_{-1.536}$	$-1.02^{0.068}_{0.045}$	$1.50^{0.217}_{-1.341}$

parameters of the FDF. For more details of the QU-fitting method, see Ideguchi et al. (2014).

We carried out the QU-fitting with a Markov Chain Monte Carlo (MCMC) approach in order to find the best fit parameters. As for the structures of the FDF, we considered two functions, a delta function or Gaussian. The two functions consist of following parameters: the Faraday depth ϕ, amplitude, and intrinsic polarization angle χ_0. In addition, the Gaussian also includes the parameter of the width of the function. We considered five FDF models, one delta function, one Gaussian, two delta functions, two Gaussians, and one delta function plus one Gaussian, and estimated the FDF models using the Bayesian information criterion (BIC). We also checked the reduced chi square (RCS) of the best fit for each model.

Table 9 and Figure 24 show the results. We found that one-component models poorly reproduce the observed Q and U, whereas the two component models apparently reproduce the observed Q and U. From Table 9, we can confirm that RCS and BIC of the one-component models are too high, whereas that of the two component models are low. However, we can not conclude the best fit model, since the RCSs of two-component models show similar values with each others. Therefore, two-component models are more reasonable, and we considered that there are two-components along the line of sight

The fitting results of the two-component models commonly show that there are components at the Faraday depth of $\phi \sim -50$ rad m^{-2}. We can interpret that the Gaussian component would be the radio relic, since the values of the Faraday depth and width are close to the average (~ -34 rad m^{-2}) and standard deviation (~ 6 rad m^{-2}) of RM of

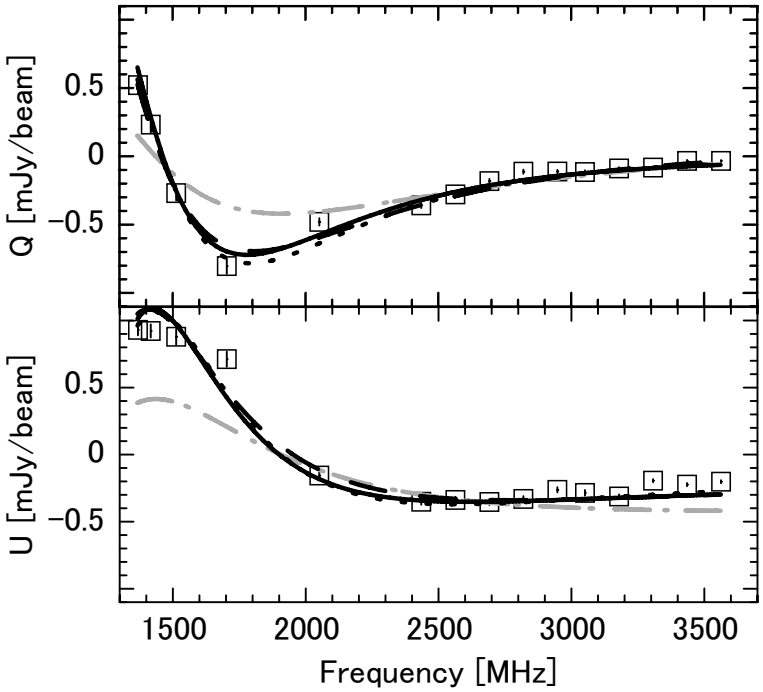

Figure 24: Results of the QU-fitting (from Ozawa et al., 2015). Marks with error bars represent the values of spatially averaged fractional polarization (Figure 16). Gray lines represent the one-component models (dashed line: delta function, dotted line: Gaussian). Black lines represent the two-component models (dashed line: two delta functions, dotted line: two Gaussians, solid line: one delta function plus one Gaussian).

the radio relic. We could also interpret that there are two-components at same physical distance toward the line of sight, since the two-component models have different intrinsic polarization angles.

5.5.3. Other Possibilities

Although we agreed that the step-like variation of the radio relic can explain with the two depolarization components along the line of sight toward the radio relic, we can also consider a possibility that the missing flux of the LAS affects the fractional polarization above ~ 3 GHz. As we have introduced in Section 5.1, missing flux exists in the surface brightness of the radio relic due to the LAS of the JVLA. The polarization intensity could be also affected by the effect of the LAS.

In order to examine the effect of the LAS for the polarization intensity, we made Stokes

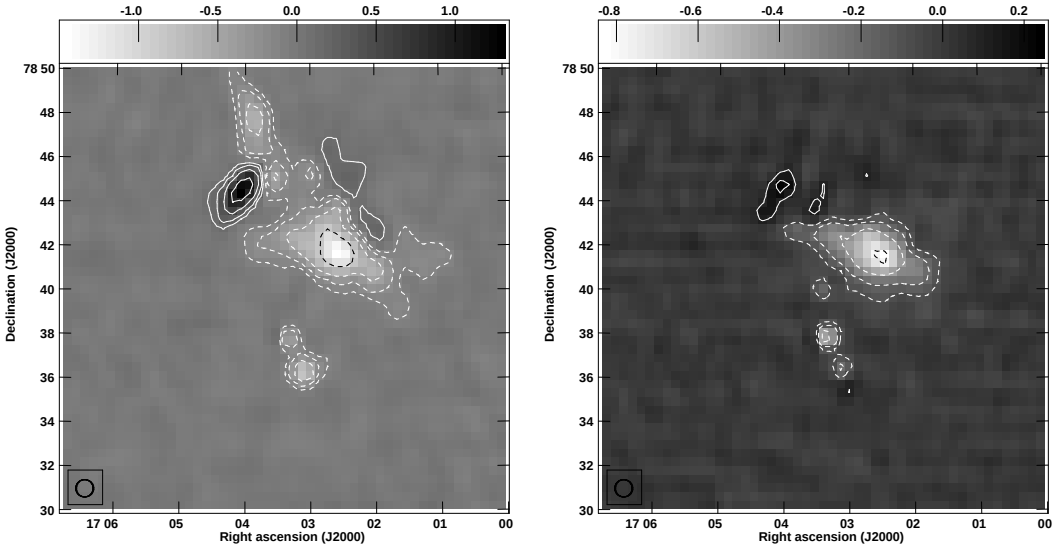

Figure 25: Stokes Q and U images of Abell 2256 at 2051 MHz in the JVLA C-array configuration. All contours are drawn at (-24, -12, -6, -3, 3, 6, 12, 24) times the rms level. *Left panel*: The image of Stokes Q. The rms level is 37.5 μJy beam^{-1}, and telescope beam size is $47\overset{\circ}{.}0\times47\overset{\circ}{.}0$. *Right panel*: The images of Stokes U. The rms level is 31.6 μJy beam^{-1}, and telescope telescope beam size is $47\overset{\circ}{.}0\times47\overset{\circ}{.}0$.

Q and U intensity images at 2051 MHz (Figure 25). In contrast to the distribution of the Stokes I intensity at 2051 MHz (top left panel in Figure 14), the distributions of Stokes Q and U intensity are more patchy since the value of Stokes Q and U can take negative values. It is considered that the missing flux of the LAS is hard to take place in Stokes Q and U. However, in the image of Stokes Q (left panel in Figure 25), it seems that the major axis of the radio relic is roughly same as that of Stokes I. The missing flux of the LAS could occur in the polarization intensity.

While the fractional polarization of the radio relic varies above $\sim$ 3 GHz, the fractional polarization of Source A and Source B show the constant values (see Figure 16). Since the scales of Source A and Source B are sufficiently compact compared with the LAS of the JVLA, the fractional polarization of Source A and Source B would not be affected by the missing flux of the LAS.

We can also see the variation of the fractional polarization between 0.35 to 1.37 GHz. Since the LAS at $\sim$ 1 GHz is sufficiently larger than the major axis of the radio relic, the decrease of the fractional polarization is not explained by the missing flux of the LAS.

Stroe et al. (2015) reported that the flux deconvolved through the CLEAN decreases with S/N . Since the S/N of the radio relic is low at high frequency (maximum S/N is $\sim 6\sigma$ at 3563 MHz), the effect may also contribute to the surface brightness of Stokes I, Q, and U, and fractional polarization of the radio relic.

6. Summary

In this thesis, we have studied the nature of the magnetic fields in the merging cluster of galaxies Abell 2256. Using depolarization models and Faraday tomography, we were able to reveal the structure of the cluster magnetic fields. For this purpose, we carried out the multiple frequency polarization observation of Abell 2256 with the JVLA at S (2051–3947 MHz) and X bands (8051–9947 MHz) in the C array configuration. We obtained the images of Stokes I, Q, and U, and calculated the rotation measure (RM) and fractional polarization of the radio relic, Source A, and Source B.

We estimated the equipartition magnetic field strengths of the radio relic using the revised equipartition formula. We found that the total equipartition magnetic field strengths of the radio relic is $B_{\rm t} \sim 5.0$ μG with $l = 25$ kpc and $B_{\rm t} \sim 1.8$ μG with $l = 1125$ kpc. The degree of uniformity of the magnetic fields is $f \sim 0.56$, suggesting the random magnetic fields along the line of sight toward the radio relic and depolarization. We also estimated the random magnetic field strength in the intracluster space using $\sigma_{\rm RM}$. We found that the magnetic fields along the line of sight toward Source A is $B \sim 1.26$ μG with $\Lambda_{\rm B} = 5$ kpc and $B \sim 0.63$ μG with $\Lambda_{\rm B} = 20$ kpc. The magnetic fields along the line of sight toward Source B is $B \sim 0.21$ μG with $\Lambda_{\rm B} = 5$ kpc and $B \sim 0.11$ μG with $\Lambda_{\rm B} = 20$ kpc.

The fractional polarization of the radio relic decreases from ~ 35 % to ~ 20 % around 3 GHz as the frequency decreases, and remains ~ 20 % between 1.37 and 3 GHz. Since the fractional polarization observed with the WSRT indicates a value less than 1 % at 0.3 GHz, the fractional polarization of the radio relic show the step-like variation. This may be caused by depolarization, but the Burn's law with a single depolarization component did not reproduce the step-like variation.

We created the depolarization models, which allow us to know the structure of the magnetic fields along the line of sight. We found that two-component depolarization models can reproduce the observed step-like variations of the fractional polarization, suggesting the existence of the two magneto-ionic component along the line of sight toward the radio relic. Furthermore, the standard deviation of the RM for the foreside depolarization component viewed from the observer has to be smaller than that for the backside depolarization component. Therefore, we can identify the position of the depolarization components along the line of sight, and the foreside component would be the intracluster space or Milky Way component, back side component would be the radio relic component. Faraday tomography also indicates the existence of the two-components Faraday dispersion function along the line of sight.

Based on above results, we conclude that there are random magnetic fields with micro Gauss order in the intracluster space of Abell 2256. Depolarization models and Faraday tomography reveal the existence of two depolarization components along the line of sight toward the radio relic, and are very useful for understanding the three-dimensional magnetic field structures.

A. Appendix

A.1. Polarization

Polarization is a property of an electromagnetic wave when its electric field vector (E-vector) oscillates in a specific orientation. It is classified into three patterns, elliptical polarization, circular polarization, and linear polarization, which have different tracks of oscillation.

In order to describe the polarization of the three patterns, we consider an orthogonal coordinate system (X, Y, Z), and an electromagnetic wave which oscillates on the XY plane and propagates to the Z axis direction. Then, the E-vector of the electromagnetic wave is written as

$$E_{\mathrm{X}} = \epsilon_X \cos(kz - \omega t + \delta_{\mathrm{X}}) \tag{91}$$

$$E_{\mathrm{Y}} = \epsilon_Y \cos(kz - \omega t + \delta_{\mathrm{Y}}) \tag{92}$$

$$E_{\mathrm{Z}} = 0, \tag{93}$$

where $E_{\mathrm{X}}, E_{\mathrm{Y}}$, and E_{Z} are the components of the E-vector in the directions of the X, Y, and Z axes, respectively, ϵ_{X} and ϵ_{Y} are the amplitudes of the E_{X} and E_{Y} components, respectively, k is the wave number, ω is the angular frequency, δ_{X} and δ_{Y} are the phase constants of the E_{X} and E_{Y} components, respectively, and we define δ as a phase difference between E_{X} and E_{Y} components, $\delta = \delta_{\mathrm{Y}} - \delta_{\mathrm{X}}$.

Elliptical Polarization A track of the E-vector of elliptical polarization traces an ellipse on the XY plane. It is a general case of circular polarization and linear polarization. Eliminating the phase from equation (91) and (92), we can obtain the track of elliptical polarization. For simplicity, we rewrite equations (91) and (92) using $\tau = kz - \omega t$:

$$E_{\mathrm{X}} = \epsilon_{\mathrm{X}} \cos(\tau + \delta_{\mathrm{X}}) \tag{94}$$

$$E_{\mathrm{Y}} = \epsilon_{\mathrm{Y}} \cos(\tau + \delta_{\mathrm{Y}}). \tag{95}$$

Rewriting equations (94) and (95) as

$$\frac{E_{\mathrm{X}}}{\epsilon_{\mathrm{X}}} = \cos(\tau + \delta_{\mathrm{X}}) = \cos\tau\cos\delta_{\mathrm{X}} - \sin\tau\sin\delta_{\mathrm{X}} \tag{96}$$

$$\frac{E_{\mathrm{Y}}}{\epsilon_{\mathrm{Y}}} = \cos(\tau + \delta_{\mathrm{Y}}) = \cos\tau\cos\delta_{\mathrm{Y}} - \sin\tau\sin\delta_{\mathrm{Y}} \tag{97}$$

gives

$$\frac{E_{\mathrm{X}}}{\epsilon_{\mathrm{X}}}\sin\delta_{\mathrm{Y}} - \frac{E_{\mathrm{Y}}}{\epsilon_{\mathrm{Y}}}\sin\delta_{\mathrm{X}} = \cos\tau\sin(\delta_{\mathrm{Y}} - \delta_{\mathrm{X}}) \quad (98)$$

$$\frac{E_{\mathrm{X}}}{\epsilon_{\mathrm{X}}}\cos\delta_{\mathrm{Y}} - \frac{E_{\mathrm{Y}}}{\epsilon_{\mathrm{Y}}}\cos\delta_{\mathrm{X}} = \sin\tau\sin(\delta_{\mathrm{Y}} - \delta_{\mathrm{X}}). \quad (99)$$

Squaring equations (98) and (99) gives

$$\left(\frac{E_{\mathrm{X}}}{\epsilon_{\mathrm{X}}}\right)^2\sin^2\delta_{\mathrm{Y}} - 2\frac{E_{\mathrm{X}}}{\epsilon_{\mathrm{X}}}\frac{E_{\mathrm{Y}}}{\epsilon_{\mathrm{Y}}}\sin\delta_{\mathrm{Y}}\sin\delta_{\mathrm{X}} + \left(\frac{E_{\mathrm{Y}}}{\epsilon_{\mathrm{Y}}}\right)^2\sin^2\delta_{\mathrm{X}} = \cos^2\tau\sin^2(\delta_{\mathrm{Y}} - \delta_{\mathrm{X}}) \quad (100)$$

$$\left(\frac{E_{\mathrm{X}}}{\epsilon_{\mathrm{X}}}\right)^2\cos^2\delta_{\mathrm{Y}} - 2\frac{E_{\mathrm{X}}}{\epsilon_{\mathrm{X}}}\frac{E_{\mathrm{Y}}}{\epsilon_{\mathrm{Y}}}\cos\delta_{\mathrm{Y}}\cos\delta_{\mathrm{X}} + \left(\frac{E_{\mathrm{Y}}}{\epsilon_{\mathrm{Y}}}\right)^2\cos^2\delta_{\mathrm{X}} = \sin^2\tau\sin^2(\delta_{\mathrm{Y}} - \delta_{\mathrm{X}}). \quad (101)$$

Adding equations (100) and (101), we obtain

$$\left(\frac{E_{\mathrm{X}}}{\epsilon_{X}}\right)^2 + \left(\frac{E_{\mathrm{Y}}}{\epsilon_{\mathrm{Y}}}\right)^2 - 2\frac{E_{\mathrm{X}}}{\epsilon_{\mathrm{X}}}\frac{E_{\mathrm{Y}}}{\epsilon_{\mathrm{Y}}}\cos\delta = \sin^2\delta, \quad (102)$$

which represents the equation of an ellipse.

Usually, the major axis of a polarization ellipse (Figure 26) of equation (102) is inclined by an arbitrary angle χ with respect to the X axis. In the new orthogonal coordinate system $(\mathrm{X}', \mathrm{Y}', \mathrm{Z})$, the equation of an ellipse is written as

$$E_{\mathrm{X}'} = \epsilon_{\mathrm{a}}\cos(\tau + \delta') \quad (103)$$

$$E_{\mathrm{Y}'} = \epsilon_{\mathrm{b}}\sin(\tau + \delta'), \quad (104)$$

where ϵ_{a} and ϵ_{b} are the amplitude of $E_{\mathrm{X}'}$ and $E_{\mathrm{Y}'}$ components, respectively, and the relationship between the $(\mathrm{X}, \mathrm{Y}, \mathrm{Z})$ coordinate system and $(\mathrm{X}', \mathrm{Y}', \mathrm{Z})$ coordinate system is given by

$$E_{\mathrm{X}'} = E_{\mathrm{X}}\cos\chi + E_{\mathrm{Y}}\sin\chi \quad (105)$$

$$E_{\mathrm{Y}'} = -E_{\mathrm{X}}\sin\chi + E_{\mathrm{Y}}\cos\chi. \quad (106)$$

In order to determine ϵ_{a} and ϵ_{b}, we substitute equations (96) and (103) into equation

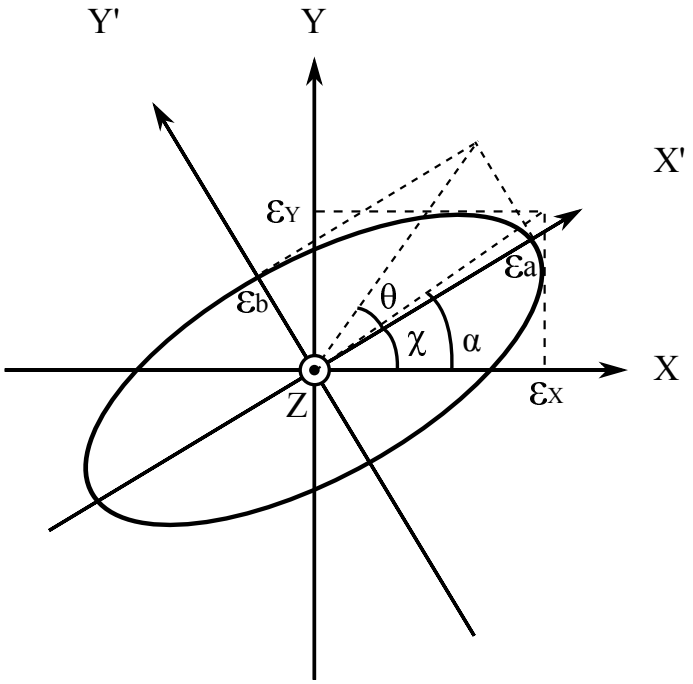

Figure 26: A polarization ellipse.

(105) (respectively equations (97) and (104) into equation (106)):

$$\begin{aligned}\epsilon_{\mathrm{a}}(\cos\tau\cos\delta' - \sin\tau\sin\delta') = \epsilon_{\mathrm{X}}(\cos\tau\cos\delta_{\mathrm{X}} - \sin\tau\sin\delta_{\mathrm{X}})\cos\chi \\ +\epsilon_{\mathrm{Y}}(\cos\tau\cos\delta_{\mathrm{Y}} - \sin\tau\sin\delta_{\mathrm{Y}})\sin\chi\end{aligned} \tag{107}$$

$$\begin{aligned}\epsilon_{\mathrm{b}}(\sin\tau\cos\delta' + \cos\tau\sin\delta') = -\epsilon_{\mathrm{X}}(\cos\tau\cos\delta_{\mathrm{X}} - \sin\tau\sin\delta_{\mathrm{X}})\sin\chi \\ +\epsilon_{\mathrm{Y}}(\cos\tau\cos\delta_{\mathrm{Y}} - \sin\tau\sin\delta_{\mathrm{Y}})\cos\chi.\end{aligned} \tag{108}$$

These equations are valid for all τ, and substituting 0 or $\pi/2$ into the τ gives

$$\epsilon_{\mathrm{a}}\cos\delta' = \epsilon_{\mathrm{X}}\cos\delta_{\mathrm{X}}\cos\chi + \epsilon_{\mathrm{Y}}\cos\delta_{\mathrm{Y}}\sin\chi \tag{109}$$

$$-\epsilon_{\mathrm{a}}\sin\delta' = -\epsilon_{\mathrm{X}}\sin\delta_{\mathrm{X}}\cos\chi - \epsilon_{\mathrm{Y}}\sin\delta_{\mathrm{Y}}\sin\chi \tag{110}$$

$$\epsilon_{\mathrm{b}}\cos\delta' = \epsilon_{\mathrm{X}}\sin\delta_{\mathrm{X}}\sin\chi - \epsilon_{\mathrm{Y}}\sin\delta_{\mathrm{Y}}\cos\chi \tag{111}$$

$$\epsilon_{\mathrm{b}}\sin\delta' = -\epsilon_{\mathrm{X}}\cos\delta_{\mathrm{X}}\sin\chi + \epsilon_{\mathrm{Y}}\cos\delta_{\mathrm{Y}}\cos\chi. \tag{112}$$

Squaring and adding equations (109) and (110) (respectively equations (111) and (112))

gives

$$\epsilon_{\rm a}^2 = \epsilon_{\rm X}^2 \cos^2\chi + \epsilon_{\rm Y}^2 \sin^2\chi + 2\epsilon_{\rm X}\epsilon_{\rm Y}\cos\chi\sin\chi\cos\delta \quad (113)$$

$$\epsilon_{\rm b}^2 = \epsilon_{\rm X}^2 \cos^2\chi + \epsilon_{\rm Y} \sin^2\chi - 2\epsilon_{\rm X}\epsilon_{\rm Y}\cos\chi\sin\chi\cos\delta, \quad (114)$$

and adding equations (113) and (114) gives a total intensity

$$S_0 \equiv \epsilon_{\rm a}^2 + \epsilon_{\rm b}^2 = \epsilon_{\rm X}^2 + \epsilon_{\rm Y}^2. \quad (115)$$

In order to obtain χ, we multiply equations (109) and (111) (respectively equations (110) and (112)), and subtracting two equations gives

$$\epsilon_{\rm a}\epsilon_{\rm b} = \epsilon_{\rm X}\epsilon_{\rm Y}\sin\delta, \quad (116)$$

while division of equations (111) by (109) (respectively equations (112) by (110)) gives

$$\frac{\epsilon_{\rm b}}{\epsilon_{\rm a}} = \frac{\epsilon_{\rm X}\sin\delta_{\rm X}\sin\chi - \epsilon_{\rm Y}\sin\delta_{\rm Y}\cos\chi}{\epsilon_{\rm X}\cos\delta_{\rm X}\cos\chi + \epsilon_{\rm Y}\cos\delta_{\rm Y}\sin\chi} = \frac{-\epsilon_{\rm X}\cos\delta_{\rm X}\sin\chi + \epsilon_{\rm Y}\cos\delta_{\rm Y}\cos\chi}{\epsilon_{\rm X}\sin\delta_{\rm X}\cos\chi + \epsilon_{\rm Y}\sin\delta_{\rm Y}\sin\chi}, \quad (117)$$

Rearranging equation (117) yields

$$\begin{aligned} -(\epsilon_{\rm X} - \epsilon_{\rm Y})^2 \sin\chi\cos\chi &= \epsilon_{\rm X}\epsilon_{\rm Y}\cos\delta(\sin^2\chi - \cos^2\chi) \\ (\epsilon_{\rm X}^2 - \epsilon_{\rm Y}^2)\sin 2\chi &= 2\epsilon_{\rm X}\epsilon_{\rm Y}\cos\delta\cos 2\chi. \end{aligned} \quad (118)$$

If we define α as

$$\tan\alpha = \frac{\epsilon_{\rm Y}}{\epsilon_{\rm X}}, \quad (119)$$

then equation (118) can be rewritten as

$$\tan 2\chi = \frac{2\epsilon_{\rm X}\epsilon_{\rm Y}}{\epsilon_{\rm X}^2 - \epsilon_{\rm Y}^2}\cos\delta = \frac{2\tan\alpha}{1-\tan^2\alpha}\cos\delta \quad (120)$$

or

$$\tan 2\chi = \tan 2\alpha\cos\delta. \quad (121)$$

Dividing equation (116) by (115), we can obtain

$$\frac{2\epsilon_{\rm a}\epsilon_{\rm b}}{\epsilon_{\rm a}^2 + \epsilon_{\rm b}^2} = \frac{2\epsilon_{\rm X}\epsilon_{\rm Y}}{\epsilon_{\rm X}^2 + \epsilon_{\rm Y}^2}\sin\delta = \sin 2\alpha\sin\delta \quad (122)$$

If we define

$$\tan\theta = \frac{\epsilon_{\mathrm{b}}}{\epsilon_{\mathrm{a}}}, \tag{123}$$

then equation (122) can be rewritten as

$$\sin 2\theta = \sin 2\alpha \sin\delta. \tag{124}$$

As a result, an elliptical polarization with ϵ_{X}, ϵ_{Y}, and δ can be represented by the polarization ellipse with ϵ_{a}, ϵ_{b}, and χ, and we have the following relations between the $\epsilon_{\mathrm{X}}, \epsilon_{\mathrm{Y}}, \delta$ and $\epsilon_{\mathrm{a}}, \epsilon_{\mathrm{b}}, \chi$, written as

$$\begin{aligned} \epsilon_{\mathrm{a}}^2 + \epsilon_{\mathrm{b}}^2 &= \epsilon_{\mathrm{X}}^2 + \epsilon_{\mathrm{Y}}^2 \\ \tan 2\chi &= \tan 2\alpha \cos\delta \\ \sin 2\theta &= \sin 2\alpha \sin\delta. \end{aligned} \tag{125}$$

Therefore, we need three parameters for describing the states of the polarizations.

Circular Polarization A track of the E-vector of circular polarization traces a circle on the XY plane. It occurs when the E_{X} and E_{Y} have same amplitude, $\epsilon_{\mathrm{X}} = \epsilon_{\mathrm{Y}}$, and the phase difference is $\delta = \pm\pi/2$. If we adopt $\epsilon_{\mathrm{X}} = \epsilon_{\mathrm{Y}} = \epsilon$ and $\delta = -\pi/2$, equations (91), (92), and (93) are rewritten as

$$E_{\mathrm{X}} = \epsilon\cos(kz - \omega t) \tag{126}$$

$$E_{\mathrm{Y}} = \epsilon\cos(kz - \omega t - \frac{\pi}{2}) = \epsilon\sin(kz - \omega t) \tag{127}$$

$$E_{\mathrm{Z}} = 0, \tag{128}$$

and we obtain

$$E_{\mathrm{X}}^2 + E_{\mathrm{Y}}^2 = \epsilon^2. \tag{129}$$

Therefore, there is an orbit of the E-vector of circular polarization which have radius ϵ on the XY plane. When the phase difference is $\delta = -\pi/2$, the rotation direction of the E-vector is clockwise, and this circular polarization is defined as left hand circular polarization (LHCP). In contrast, when the phase difference is $\delta = \pi/2$, then the direction of the rotation of the E-vector is counterclockwise, which is defined as right hand circular polarization (RHCP).

Note that an arbitrary elliptical polarization can be decomposed to the sum of two

circular polarization. Equations (103) and (104) can be written as

$$E_{X'} = \epsilon_a \cos(\tau + \delta') = (\epsilon_r + \epsilon_l)\cos(\tau + \delta') \quad (130)$$

$$E_{Y'} = \epsilon_b \sin(\tau + \delta') = (\epsilon_r - \epsilon_l)\cos(\tau + \delta' - \frac{\pi}{2}). \quad (131)$$

Therefore, the amplitude of the circular polarization ϵ_r and ϵ_l are given by

$$\epsilon_r = \frac{1}{2}(\epsilon_a + \epsilon_b) \quad (132)$$

$$\epsilon_l = \frac{1}{2}(\epsilon_a - \epsilon_b). \quad (133)$$

and we obtain

$$S_0 = \epsilon_a^2 + \epsilon_b^2 = \epsilon_r^2 + \epsilon_l^2. \quad (134)$$

Linear Polarization A track of the E-vector of linear polarization traces a line on the XY plane. It occurs when the E_X and E_Y have same phase; the phase difference is $\delta = 0$ or $\delta = \pm\pi$. If we adopt $\delta = 0$, equations (91), (92), and (93) are rewritten as

$$E_X = \epsilon_X \cos(kz - \omega t) \quad (135)$$

$$E_Y = \epsilon_Y \cos(kz - \omega t) \quad (136)$$

$$E_Z = 0. \quad (137)$$

If we combine two linear polarizations which have the phase difference of 0 or $\pm\pi/2$, then we can create a new linear polarization, and the linear polarization divided into two linear polarizations (Rohlfs & Wilson, 1996; Ernst Lueder , 2010).

A.2. Stokes Parameter

Stokes parameters consist of four quantities (I, Q, U, V), which describe the states of the polarization. Combination of Stokes I, Q, U, and V provides us the information of the polarization: polarization intensity, fractional polarization, and polarization angle. In this section, we introduce the definition of Stokes parameters and lead the information of the polarization.

Stokes parameter Stokes parameters are defined as

$$I = \epsilon_{\rm a}^2 + \epsilon_{\rm b}^2 \tag{138}$$

$$Q = S_0 \cos 2\theta \cos 2\chi \tag{139}$$

$$U = 2S_0 \cos 2\theta \sin 2\chi \tag{140}$$

$$V = 2S_0 \sin 2\theta, \tag{141}$$

where $\epsilon_{\rm a}$ and $\epsilon_{\rm b}$ are the amplitude of the major axis and minor axis of the polarization ellipse, respectively, $S_0 = I = \epsilon_{\rm a}^2 + \epsilon_{\rm b}^2$, χ is the inclination of the major axis of the polarization ellipse to the X axis, and $\tan\theta = \epsilon_{\rm b}/\epsilon_{\rm a}$.

Equations (138), (139), (140), and (141) can be rewritten into the form using $\epsilon_{\rm X}$, $\epsilon_{\rm Y}$, and δ. In order to rewrite Stokes parameters, from equation (119), we obtain

$$\tan 2\alpha = \frac{2\tan\alpha}{1-\tan^2\alpha} = \frac{2\epsilon_{\rm X}\epsilon_{\rm Y}}{\epsilon_{\rm X}^2 - \epsilon_{\rm Y}^2} \tag{142}$$

$$\cos 2\alpha = \frac{1-\tan^2\alpha}{1+\tan^2\alpha} = \frac{\epsilon_{\rm X}^2 - \epsilon_{\rm Y}^2}{\epsilon_{\rm X}^2 + \epsilon_{\rm Y}^2} \tag{143}$$

$$\sin 2\alpha = \frac{2\tan\alpha}{1+\tan^2\alpha} = \frac{2\epsilon_{\rm X}\epsilon_{\rm Y}}{\epsilon_{\rm X}^2 + \epsilon_{\rm Y}^2} \tag{144}$$

From equation (124), using equations (144) and (115), we obtain

$$\sin 2\theta = \frac{2\epsilon_{\rm X}\epsilon_{\rm Y}}{\epsilon_{\rm X}^2 + \epsilon_{\rm Y}^2}\sin\delta = \frac{2\epsilon_{\rm X}\epsilon_{\rm Y}}{S_0}\sin\delta, \tag{145}$$

and

$$\begin{aligned}\cos 2\theta &= \sqrt{1-\sin^2 2\theta} \\ &= \sqrt{\frac{S_0^2}{S_0^2} - \frac{(2\epsilon_{\rm X}\epsilon_{\rm Y})^2\sin^2\delta}{S_0^2}} \\ &= \frac{\sqrt{S_0^2 - (2\epsilon_{\rm X}\epsilon_{\rm Y})^2\sin^2\delta}}{S_0}.\end{aligned} \tag{146}$$

From equation (121), using equation (142), we obtain

$$\tan 2\chi = \frac{2\epsilon_{\rm X}\epsilon_{\rm Y}}{\epsilon_{\rm X}^2 - \epsilon_{\rm Y}^2}\cos\delta, \tag{147}$$

$$\begin{aligned}
\cos 2\chi &= \sqrt{\frac{\cos^2 2\chi}{\sin^2 2\chi + \cos^2 2\chi}} \\
&= \frac{1}{\sqrt{1+\tan^2 2\chi}} \\
&= \frac{1}{\sqrt{1+(\frac{2\epsilon_X\epsilon_Y}{\epsilon_X^2-\epsilon_Y^2})^2(1-\sin^2\delta)}} \\
&= \frac{\epsilon_X^2-\epsilon_Y^2}{\sqrt{S_0^2-(2\epsilon_X\epsilon_Y)^2\sin^2\delta}},
\end{aligned} \tag{148}$$

and

$$\begin{aligned}
\sin 2\chi &= \sqrt{\frac{\sin 2\chi^2}{\sin 2\chi^2 + \cos 2\chi^2}} \\
&= \sqrt{\frac{\tan 2\chi^2}{\tan 2\chi^2 + 1}} \\
&= \frac{2\epsilon_X\epsilon_Y\cos\delta}{\sqrt{S_0^2-(2\epsilon_X\epsilon_Y)^2\sin^2\delta}}.
\end{aligned} \tag{149}$$

Substituting equations (145), (146), (148), and (149) into equations (138), (139), (140), and (141), we can obtain

$$I = \epsilon_X^2 + \epsilon_Y^2 = S_0 \tag{150}$$

$$Q = \epsilon_X^2 - \epsilon_Y^2 = S_0\cos 2\theta\cos 2\chi \tag{151}$$

$$U = 2\sqrt{\epsilon_X^2\epsilon_Y^2}\cos\delta = S_0\cos 2\theta\sin 2\chi \tag{152}$$

$$V = 2\sqrt{\epsilon_X^2\epsilon_Y^2}\sin\delta = S_0\sin 2\theta, \tag{153}$$

and

$$I^2 = Q^2 + U^2 + V^2. \tag{154}$$

On the other hand, in the case that the observed electromagnetic wave is partially

polarized, we obtain

$$
\begin{aligned}
I &= \langle \epsilon_{\rm X}^2 \rangle + \langle \epsilon_{\rm Y}^2 \rangle && (155)\\
Q &= \langle \epsilon_{\rm X}^2 \rangle - \langle \epsilon_{\rm Y}^2 \rangle && (156)\\
U &= 2\langle \sqrt{\epsilon_{\rm X}^2 \epsilon_{\rm Y}^2} \rangle \cos\delta && (157)\\
V &= 2\langle \sqrt{\epsilon_{\rm X}^2 \epsilon_{\rm Y}^2} \rangle \sin\delta, && (158)
\end{aligned}
$$

where brackets represent the time average value and

$$
I^2 \geq Q^2 + U^2 + V^2. \tag{159}
$$

Stokes parameters allow us to know the states of the polarization from observations.

(a) For horizontally linear polarization, we have $\epsilon_{\rm Y} = 0$, so that

$$
\begin{aligned}
I &= S_0\\
Q &= S_0\\
U &= 0\\
V &= 0.
\end{aligned} \tag{160}
$$

(b) For vertically linear polarization, we have $\epsilon_{\rm X} = 0$, so that

$$
\begin{aligned}
I &= S_0\\
Q &= -S_0\\
U &= 0\\
V &= 0.
\end{aligned} \tag{161}
$$

(c) For $+45^\circ$ linear polarization, we have $\epsilon_{\rm X} = \epsilon_{\rm Y}$ and $\delta = 0$, so that

$$
\begin{aligned}
I &= S_0\\
Q &= 0\\
U &= S_0\\
V &= 0.
\end{aligned} \tag{162}
$$

(d) For -45° linear polarization, we have $\epsilon_{\rm X} = \epsilon_{\rm Y}$ and $\delta = \pm\pi$, so that

$$\begin{aligned} I &= S_0 \\ Q &= 0 \\ U &= -S_0 \\ V &= 0. \end{aligned} \tag{163}$$

(e) For left hand circular polarization, we have $\epsilon_{\mathrm{X}} = \epsilon_{\mathrm{Y}}$ and $\delta = -\pi/2$, so that

$$\begin{aligned} I &= S_0 \\ Q &= 0 \\ U &= 0 \\ V &= -S_0. \end{aligned} \tag{164}$$

(f) For right hand circular polarization, we have $\epsilon_{\mathrm{X}} = \epsilon_{\mathrm{Y}}$ and $\delta = \pi/2$, so that

$$\begin{aligned} I &= S_0 \\ Q &= 0 \\ U &= 0 \\ V &= S_0. \end{aligned} \tag{165}$$

Here, we describe how to detect Stokes parameters. For this purpose, we again consider an electromagnetic wave which oscillates on the XY plane and propagates to the Z axis direction, and rewrite equation (91) and (92) to the form of the complex number:

$$\begin{aligned} E_{\mathrm{X}} &= \epsilon_{\mathrm{X}} \cos(kz - \omega t) \\ &= \mathbf{Re}\left[\epsilon_{\mathrm{X}} e^{i(kz-\omega t)}\right] \qquad (166) \\ E_{\mathrm{Y}} &= \epsilon_{\mathrm{Y}} \cos(kz - \omega t + \delta) \\ &= \mathbf{Re}\left[\epsilon_{\mathrm{Y}} e^{i(kz-\omega t+\delta)}\right], \qquad (167) \end{aligned}$$

where **Re** represents the real part of the complex number; in the following sentences, we omit the symbol of **Re** from the formula for simplicity. We define β as

$$\tan\beta = \frac{E_{\mathrm{Y}}}{E_{\mathrm{X}}}, \tag{168}$$

and if we rotate the coordinate by an angle β, then the E-vector is expressed as a function

of β:

$$E(\beta,\delta) = E_{\mathrm{X}}\cos\beta + E_{\mathrm{Y}}\sin\beta \tag{169}$$
$$= \epsilon_{\mathrm{X}} e^{i(kz-\omega t)}\cos\beta + \epsilon_{\mathrm{Y}} e^{i(kz-\omega t+\delta)}\sin\beta. \tag{170}$$

Since the Poynting vector of the Z axis component is given by

$$S_z = cu_{em} = c\epsilon_0 \left|\boldsymbol{E}\right|^2, \tag{171}$$

the intensity with respect to the β is written as

$$\begin{aligned} I(\beta,\delta) &\sim E(\beta)^2 \\ &= EE^* \\ &= \epsilon_{\mathrm{X}}^2\cos^2\beta + \epsilon_{\mathrm{Y}}^2\sin^2\beta + 2\epsilon_{\mathrm{X}}\epsilon_{\mathrm{Y}}\sin\beta\cos\beta\cos\delta \\ &= \frac{\epsilon_{\mathrm{X}}^2+\epsilon_{\mathrm{Y}}^2}{2}(\sin^2\beta+\cos^2\beta) + \frac{\epsilon_{\mathrm{X}}^2-\epsilon_{\mathrm{Y}}^2}{2}(\cos^2\beta-\sin^2\beta) + 2\epsilon_{\mathrm{X}}\epsilon_{\mathrm{Y}}\sin\beta\cos\beta\cos\delta \\ &= \frac{\epsilon_{\mathrm{X}}^2+\epsilon_{\mathrm{Y}}^2}{2} + \frac{\epsilon_{\mathrm{X}}^2-\epsilon_{\mathrm{Y}}^2}{2}\cos 2\beta + \epsilon_{\mathrm{X}}\epsilon_{\mathrm{Y}}\sin 2\beta\cos\delta. \end{aligned} \tag{172}$$

We can rewrite equation (172) in the form of time-independent:

$$I(\beta,\delta) = \frac{\langle\epsilon_{\mathrm{X}}^2\rangle + \langle\epsilon_{\mathrm{Y}}^2\rangle}{2} + \frac{\langle\epsilon_{\mathrm{X}}^2\rangle - \langle\epsilon_{\mathrm{Y}}^2\rangle}{2}\cos 2\beta + \sqrt{\langle\epsilon_{\mathrm{X}}^2\rangle\langle\epsilon_{\mathrm{Y}}^2\rangle}\sin 2\beta\cos\delta. \tag{173}$$

If we adopt 0° or 90° into β, we can obtain

$$I(0^\circ,\delta) = \langle\epsilon_{\mathrm{X}}^2\rangle \tag{174}$$
$$I(90^\circ,\delta) = \langle\epsilon_{\mathrm{Y}}^2\rangle, \tag{175}$$

and

$$I = \langle\epsilon_{\mathrm{X}}^2\rangle + \langle\epsilon_{\mathrm{Y}}^2\rangle = I(0^\circ,\delta) + I(90^\circ,\delta) \tag{176}$$
$$Q = \langle\epsilon_{\mathrm{X}}^2\rangle - \langle\epsilon_{\mathrm{Y}}^2\rangle = I(0^\circ,\delta) - I(90^\circ,\delta). \tag{177}$$

If we adopt 45° or -45° into β, we can obtain

$$I(45^\circ,\delta) = \frac{\langle\epsilon_{\mathrm{X}}^2\rangle + \langle\epsilon_{\mathrm{Y}}^2\rangle}{2} + \sqrt{\langle\epsilon_{\mathrm{X}}^2\rangle\langle\epsilon_{\mathrm{Y}}^2\rangle}\cos\delta \tag{178}$$
$$I(-45^\circ,\delta) = \frac{\langle\epsilon_{\mathrm{X}}^2\rangle + \langle\epsilon_{\mathrm{Y}}^2\rangle}{2} - \sqrt{\langle\epsilon_{\mathrm{X}}^2\rangle\langle\epsilon_{\mathrm{Y}}^2\rangle}\cos\delta, \tag{179}$$

and

$$U = 2\sqrt{\langle\epsilon_{\rm X}^2\rangle\langle\epsilon_{\rm Y}^2\rangle}\cos\delta = I(45^\circ,\delta) - I(-45^\circ,\delta). \tag{180}$$

In order to obtain Stokes V, we rewrite equations (178) and (179) to the form using $\cos(\delta - \pi/2) = \sin\delta$,

$$I(45^\circ,\delta-\frac{\pi}{2}) = \frac{\langle\epsilon_{\rm X}^2\rangle + \langle\epsilon_{\rm Y}^2\rangle}{2} + \sqrt{\langle\epsilon_{\rm X}^2\rangle\langle\epsilon_{\rm Y}^2\rangle}\sin\delta \tag{181}$$

$$I(-45^\circ,\delta-\frac{\pi}{2}) = \frac{\langle\epsilon_{\rm X}^2\rangle + \langle\epsilon_{\rm Y}^2\rangle}{2} - \sqrt{\langle\epsilon_{\rm X}^2\rangle\langle\epsilon_{\rm Y}^2\rangle}\sin\delta, \tag{182}$$

and obtain

$$V = 2\epsilon_{\rm X}\epsilon_{\rm Y}\sin\delta = I(45^\circ,\delta-\frac{\pi}{2}) - I(-45^\circ,\delta-\frac{\pi}{2}). \tag{183}$$

Therefore, we can measure Stokes parameters (I, Q, U, V) from the amplitude of the E-vector, using linear polarizer and 1/4 wavelength plate.

Fractional Polarization Fractional polarization is the ratio of the total intensity to the polarization intensity. Stokes parameters lead the fractional polarization p as

$$p = \frac{\sqrt{Q^2+U^2+V^2}}{I}. \tag{184}$$

In the synchrotron emission, usually, the intensity of circular polarization is low, but the intensity of linear polarization is strong (Beck & Wielebinski, 2013). As we have shown in equations (164) and (165), Stokes V represent the intensity of circular polarization. Therefore, the fractional polarization of linear polarization is given by

$$p = \frac{\sqrt{Q^2+U^2}}{I}, \tag{185}$$

If we consider the linear polarization of synchrotron emission, the intrinsic fractional polarization p_0 is given by

$$p_0 = \frac{3p_e+3}{3p_e+7} \tag{186}$$

(Le Roux, 1961), where p_e is the spectral index of the energy spectrum of relativistic electrons. If we adopt the typical values of diffuse sources of cluster of galaxies of $\gamma = 2.5$ (Feretti et al., 1995), expected intrinsic fractional polarization is about 0.72.

Polarization Angle Polarization angle is the position angle of the E-vector of linear polarization, which is defined as

$$\chi = \frac{1}{2} \arctan\left(\frac{U}{Q}\right), \tag{187}$$

where $0 \leq \chi \leq \pi$. We note that if the polarization angle is $\chi = 0$, then the direction of the E-vector is north, and it has a right-handed coordinate system.

A.3. Programs for the Depolarization Models

We describe the details of the EFD+EFD and IFD+IFD depolarization models. We made the calculation program with Fortran 90. In order to carry out the program attached to this appendix, we need linux and have to install Fortran compiler and gnuplot (the installation procedure of Fortran compiler is beyond the scope of this thesis).

As we have discussed in Section 5.5.1, both the EFD+EFD and IFD+IFD models assume the situation that there are two depolarization components along the line of sight. The depolarization component consist of many cells, which contain uniform electron density and uniform magnetic field strength with a single scale random direction. In our program, we firstly generate uniform random numbers and put the random magnetic fields into each cell. With the uniform electrons, we calculate the RM of the depolarization component in each cylinder at (X,Y), and calculate the observed polarization angle in each frequency. We lastly calculate the polarization intensity and fractional polarization.

Each program of the depolarization models consists of two execution files (compile.sh and go) and four directories (input, plot, results, src). The compile.sh and go file carry out the compiling and running the program. Each directory store the parameter file, plot files, result files, and source files. The result files are created after carrying out the program.

Using the parameter file, we can modify the parameters for the depolarization model. The parameters are stored in parameter.txt, shown in Appendix A3.1 and A3.2. We can set the following parameters: the magnetic fields B(1) and B(2), the electron densities ne(1) and ne(2), the number of cells in the direction of the Z axis Ncell(1) and Ncell(2), the coefficients of the polarization intensity CPolI(1) and CPolI(2), the spectral index alpha(1) and alpha(2), the intrinsic polarization angle phi0(1) and phi0(2), the number of cells in the direction of the X and Y axes Ncyl, the size of cells cellsize, the calculation points in the frequency domain Nf, and the intrinsic fractional polarization p0. Subscription (1) and (2) represent the foreside and backside depolarization components

viewed from the observer, respectively. Only in the EFE+EFD models, parameter sc can switch the single and two-component depolarization model.

In order to carry out the program, we firstly move to the EFD+EFD or IFD+IFD directly on your terminal. We can compile the program with `./compile.sh`, and the execution file go is generated. If you carry out `./compile.sh clean`, the object files in src directly, result files, and the execution file go are removed. GFortran is designated as the default compiler. If you use other compiler, you have to rewrite the FC in makefile. We can carry out the program with `./go` and the results are stored in results directly. If you have gnuplot, the fractional polarization spectra, histogram of the RM, and RM distribution images are generated.

A.3.1. EFD+EFD model

We attached the program of the EFD+EFD depolarization model. If you carry out the program, you have to store the source codes as follows.

Directory structure

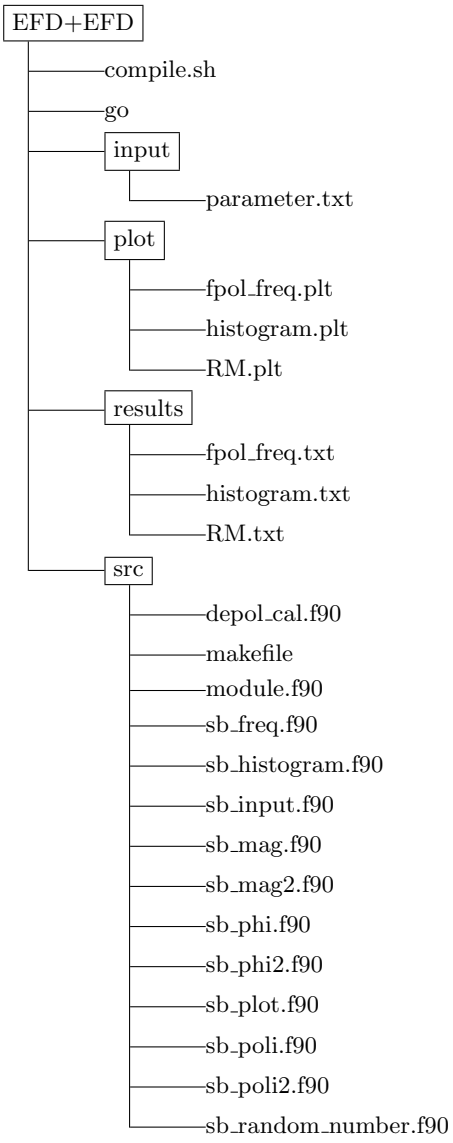

compile.sh

```
#!/bin/bash

cd ./src/
if [ "$1" = "clean" ] ; then
  make clean
  rm ../go
else
  make
  mv ./go ..
fi
cd ..

exit 0
```

parameter.txt

```
----EFD(first_component) 0
B(1)= 1d0                    B: magnetic field strength [uG]
ne(1)= 0.0106d0              ne: electron density [cm^-3]
Ncyl= 50                     Nsil: number of x=y cylinders
Ncell(1)= 100                Ncell: number of cells
cellsize= 2                  cellsize: [kpc]
phi0(1)= 0.0d0               phi0: intrinsic Pol. angle [rad]
Nf= 20                       Nf: number of freq. points
alpha(1)= -0.8d0             alpha: spectral index
CPolI(1)= 1.0d0              CPolI: coefficient of PolI
p0= 1d0                      p0: intrinsic FPOL
----EFD(second_component) 0
sc= 1                        sc: 1:single 2:dble
B(2)= 2.3d0                  B: magnetic field strength [uG]
ne(2)= 0.003d0               ne2: 2nd sc electron density [cm^-3]
Ncell(2)= 300                Ncell: number of 2nd cells
CPolI(2)= 3.0d0              CPolI: coefficient of PolI
alpha(2)= -0.8d0             alpha: spectral index
phi0(2)= 0.0d0               phi0: intrinsic Pol. angle [rad]
```

fpol_freq.plt

```
clear
reset
set terminal postscript eps enhanced
set output 'fpol_freq.eps'

set xlabel offset 0,-1
set bmargin 6
set lmargin 12
set xlabel font "Helvetica,28" "Frequency [GHz]"
set ylabel  font "Helvetica,28" "Fractional polarization" \
offset -2

#set label 1 at graph -0.005,-0.0345 "0.3" font "Helvetica,28"
set label 2 at graph 1.012,-0.0345 "0" font "Helvetica,28"

set format x "{%.0l}"
set xtics 10 font "Helvetica,28"
set ytics 0.1 font "Helvetica,28"
set mytic

set key at graph 0.35,0.95
set key font "Helvetica,26"
set key spacing 2

set logscale x
set logscale y
set xrange [1*1E09:10*1e09]
set yrange [0:0.8]

set pointsize 2
```

```
set bar 2

plot "./results/fpol_freq.txt" index 0 using 1:2 title "" \
with lines

set terminal aqua
set output
```

histogram.plt

```
clear
reset
set terminal postscript eps enhanced
set output 'histogram.eps'

set bmargin 6
set lmargin 12
set xlabel font "Helvetica,28" "RM [rad m^{-2}]" offset 0,-2
set ylabel font "Helvetica,28" "Number of pixels" offset -2

set xtics 20 font "Helvetica,28" offset 0,-1
set ytics 50 font "Helvetica,28"

set xrange [-100:100]

plot "./results/histogram.txt" index 0 using 1:2 title "" \
with boxes

set terminal aqua
set output
```

RM.plt

```
clear
reset
set terminal postscript eps enhanced color
set output 'RM.eps'
set pm3d corners2color c1
set pm3d map
set size ratio 1

set cbrange[-20:20]
set palette defined (-20 "blue", 0 "white", 20 "red")

splot './results/RM.txt' title ""

set terminal aqua
set output
```

makefile

```
TARGET = go
OBJECTS = module.o sb_input.o sb_freq.o sb_random_number.o \
sb_mag.o sb_mag2.o sb_phi.o sb_phi2.o \
sb_poli.o sb_poli2.o sb_histogram.o sb_plot.o depol_cal.o
MOD_FILES  = module.mod
FC = gfortran

FFLAGS += -fimplicit-none
#LDFLAGS +=

.SUFFIXES : .o .f90
.f90.o:
        ${FC} -c $<
${TARGET} : ${OBJECTS}
        ${FC} -o $@ ${OBJECTS} ${LDFLAGS} ${FFLAGS}
.PHONY: clean
clean:
        ${RM} ${TARGET} ${OBJECTS} ${MOD_FILES}
# above space is tab space
```

depol_cal.f90

```
!=============================================================
! EFD+EFD Version-141231 Produced by Takeaki Ozawa
!=============================================================
  program depol_cal
  use module
  implicit none
! local variables
  integer(4)                    :: i,j,k

!#############################################################
! calculation
!#############################################################
  call sb_input
  call sb_freq
  select case(sc)
    case(1); call sb_mag; call sb_phi; call sb_poli
    case(2); call sb_mag2; call sb_phi2; call sb_poli2
  end select

!#############################################################
! results
!#############################################################
  print "(80('*'))"
  print "('*',a,t80,'*')",' depol_cal'
  print "('*',a,f6.1,a,f6.1,t80,'*')", &
&       ' RMave(1)=',RMave(1),' RMsd(1)=',RMsd(1)
  if(sc==2) then
    print "('*',a,f6.1,a,f6.1,t80,'*')", &
&         ' RMave(2)=',RMave(2),' RMsd(2)=',RMsd(2)
  end if
  print "(80('*'))"

!-------------------------------------------------------------
! fpol-freq.txt
!-------------------------------------------------------------
  open(10,status='unknown',file='./results/fpol_freq.txt')
  write(10,"(3(a))") '#',' frequency',' FPOL'
  do k=1,4*Nf+1
    write(10,"(e12.5,2x,f5.3)") freq(k),FPOL(k)
  end do
  close(10)

!-------------------------------------------------------------
! RM.txt
!-------------------------------------------------------------
  open(10,status='unknown',file='./results/RM.txt')
  do j=1,Ncyl
  do i=1,Ncyl
    write(10,"(2(2x,i3),3x,f6.1)") i,j,RMcyl(i,j,1)
  end do
  write(10,*)
  end do
  if(sc==2) then
    do j=1,Ncyl
    do i=1,Ncyl
      write(10,"(2(2x,i3),3x,f6.1)") i,j,RMcyl(i,j,1) &
&                                    +RMcyl(i,j,1)+RMcyl(i,j,2)
    end do
    write(10,*)
    end do
```

```
  end if
  close(10)

!-------------------------------------------------------
! histogram.txt
!-------------------------------------------------------
  call sb_histogram(Ncyl,Ncyl)
  open(10,status='unknown',file='./results/histogram.txt')
  do i=-5000,5000,10
  if(i==0) then
    write(10,"(i5,i4)") i,hist(i)
  else
    write(10,"(i5,i4)") i,hist(i/10)
  end if
  end do
  close(10)

!############################################################
! plot
!############################################################
  call sb_plot

  end program depol_cal
```

module.f90

```
!=========================================================
! module
!=========================================================
  module module
  implicit none

!############################################################
! global variables
!############################################################
! magnetic field strength
  real(8),allocatable,save      :: B(:)
  real(8),allocatable,save      :: Bp(:,:,:,:,:)
! electron density
  real(8),allocatable,save      :: ne(:)
! polarization angle
  real(8),allocatable,save      :: Phicyl(:,:,:,:)
  real(8),allocatable,save      :: RMcyl(:,:,:)
  real(8),allocatable,save      :: RMave(:)
  real(8),allocatable,save      :: RMsd(:)
  real(8),allocatable,save      :: Phi0(:)
! polarization intensity
  real(8),allocatable,save      :: PolI(:,:)
  real(8),allocatable,save      :: ReEuler(:)
  real(8),allocatable,save      :: ImEuler(:)
  real(8),allocatable,save      :: CPolI(:)
  real(8),allocatable,save      :: FPOL(:)
  real(8),save                  :: p0
! frequency
  integer(4),save               :: Nf
  real(8),allocatable,save      :: freq(:)
  real(8),allocatable,save      :: lambda(:)
! synchrotron emission
  real(8),allocatable,save      :: alpha(:)
! cell
  integer(4),save               :: Ncyl
  integer(4),allocatable,save   :: Ncell(:)
  real(8),save                  :: cellsize
  real(8),allocatable,save      :: rnd(:)
! RM screen
  integer(4),save               :: sc
! results
  integer(4),allocatable,save   :: hist(:)

!############################################################
! constants
!############################################################
  real(8),parameter             :: pi=3.14159265358979d0
  real(8),parameter             :: radian=57.2957795130823d0
  real(8),parameter             :: clight=2.9979245800D+08

  end module module
```

sb_input.f90

```
!=========================================================
! sb_input
!=========================================================
  subroutine sb_input
  use module
  implicit none
! local variables
  integer(4)                    :: ifrag
  real(8)                       :: tagr
  character(10)                 :: tagc
  character(100)                :: line
! allocation
  allocate(B(2))
  allocate(ne(2))
  allocate(alpha(2))
  allocate(phi0(2))
  allocate(ncell(2))
  allocate(CPolI(2))

!############################################################
! input
!############################################################
!-----------------------------------------------------------
! magnetic field strength
!-----------------------------------------------------------
  open(10,form='formatted',status='old',&
&        file='./input/parameter.txt')
  ifrag=0
  do while(ifrag==0)
    read(10,"(a)") line
    read(line,*) tagc,tagr
    if(tagc=='B(1)=') then
      B(1)=tagr
      ifrag=1
    end if
  end do
  close(10)

!-----------------------------------------------------------
! electron density
!-----------------------------------------------------------
  open(10,form='formatted',status='old',&
&         file='./input/parameter.txt')
  ifrag=0
  do while(ifrag==0)
    read(10,"(a)") line
    read(line,*) tagc,tagr
    if(tagc=='ne(1)=') then
      ne(1)=tagr
      ifrag=1
    end if
  end do
  close(10)

!-----------------------------------------------------------
! number of cylinders
```

```
!-------------------------------------------------------------
  open(10,form='formatted',status='old',&
&         file='./input/parameter.txt')
  ifrag=0
  do while(ifrag==0)
    read(10,"(a)") line
    read(line,*) tagc,tagr
    if(tagc=='Ncyl=') then
      Ncyl=int(tagr)
      ifrag=1
    end if
  end do
  close(10)

!-------------------------------------------------------------
! number of cells
!-------------------------------------------------------------
  open(10,form='formatted',status='old',&
&         file='./input/parameter.txt')
  ifrag=0
  do while(ifrag==0)
    read(10,"(a)") line
    read(line,*) tagc,tagr
    if(tagc=='Ncell(1)=') then
      Ncell(1)=int(tagr)
      ifrag=1
    end if
  end do
  close(10)

!-------------------------------------------------------------
! cellsize
!-------------------------------------------------------------
  open(10,form='formatted',status='old',&
&         file='./input/parameter.txt')
  ifrag=0
  do while(ifrag==0)
    read(10,"(a)") line
    read(line,*) tagc,tagr
    if(tagc=='cellsize=') then
      cellsize=tagr
      ifrag=1
    end if
  end do
  close(10)

!-------------------------------------------------------------
! phi0
!-------------------------------------------------------------
  open(10,form='formatted',status='old',&
&         file='./input/parameter.txt')
  ifrag=0
  do while(ifrag==0)
    read(10,"(a)") line
    read(line,*) tagc,tagr
    if(tagc=='phi0(1)=') then
      phi0(1)=tagr
      ifrag=1
    end if
  end do
  close(10)

!-------------------------------------------------------------
! Nf
!-------------------------------------------------------------
  open(10,form='formatted',status='old',&
&         file='./input/parameter.txt')
  ifrag=0
  do while(ifrag==0)
    read(10,"(a)") line
    read(line,*) tagc,tagr
    if(tagc=='Nf=') then
      Nf=int(tagr)
      ifrag=1
    end if
  end do
  close(10)

!-------------------------------------------------------------
! alpha(1)
!-------------------------------------------------------------
  open(10,form='formatted',status='old',&
&         file='./input/parameter.txt')
  ifrag=0
  do while(ifrag==0)
    read(10,"(a)") line
    read(line,*) tagc,tagr
    if(tagc=='alpha(1)=') then
      alpha(1)=tagr
      ifrag=1
    end if
  end do
  close(10)

!-------------------------------------------------------------
! CPolI(1)
!-------------------------------------------------------------
  open(10,form='formatted',status='old',&
&         file='./input/parameter.txt')
  ifrag=0
  do while(ifrag==0)
    read(10,"(a)") line
    read(line,*) tagc,tagr
    if(tagc=='CPolI(1)=') then
      CPolI(1)=tagr
      ifrag=1
    end if
  end do
  close(10)

!-------------------------------------------------------------
! sc
!-------------------------------------------------------------
  open(10,form='formatted',status='old',&
&         file='./input/parameter.txt')
  ifrag=0
  do while(ifrag==0)
    read(10,"(a)") line
    read(line,*) tagc,tagr
    if(tagc=='sc=') then
      sc=int(tagr)
      ifrag=1
    end if
  end do
  close(10)

!-------------------------------------------------------------
! number of second cells
!-------------------------------------------------------------
  open(10,form='formatted',status='old',&
&  file='./input/parameter.txt')
  ifrag=0
  do while(ifrag==0)
    read(10,"(a)") line
    read(line,*) tagc,tagr
    if(tagc=='Ncell(2)=') then
      Ncell(2)=int(tagr)
      ifrag=1
```

```
    end if
  end do
  close(10)

!-------------------------------------------------------------
! 2nd sc. magnetic field strength
!-------------------------------------------------------------
  open(10,form='formatted',status='old',&
&         file='./input/parameter.txt')
  ifrag=0
  do while(ifrag==0)
    read(10,"(a)") line
    read(line,*) tagc,tagr
    if(tagc=='B(2)=') then
      B(2)=tagr
      ifrag=1
    end if
  end do
  close(10)

!-------------------------------------------------------------
! 2nd sc. electron density
!-------------------------------------------------------------
  open(10,form='formatted',status='old',&
&         file='./input/parameter.txt')
  ifrag=0
  do while(ifrag==0)
    read(10,"(a)") line
    read(line,*) tagc,tagr
    if(tagc=='ne(2)=') then
      ne(2)=tagr
      ifrag=1
    end if
  end do
  close(10)

!-------------------------------------------------------------
! CPolI(2)
!-------------------------------------------------------------
  open(10,form='formatted',status='old',&
&         file='./input/parameter.txt')
  ifrag=0
  do while(ifrag==0)
    read(10,"(a)") line
    read(line,*) tagc,tagr
    if(tagc=='CPolI(2)=') then
      CPolI(2)=tagr
      ifrag=1
    end if
  end do
  close(10)

!-------------------------------------------------------------
! alpha(2)
!-------------------------------------------------------------
  open(10,form='formatted',status='old',&
&         file='./input/parameter.txt')
  ifrag=0
  do while(ifrag==0)
    read(10,"(a)") line
    read(line,*) tagc,tagr
    if(tagc=='alpha(2)=') then
      alpha(2)=tagr
      ifrag=1
    end if
  end do
  close(10)

!-------------------------------------------------------------
! phi0(2)
!-------------------------------------------------------------
  open(10,form='formatted',status='old',&
&         file='./input/parameter.txt')
  ifrag=0
  do while(ifrag==0)
    read(10,"(a)") line
    read(line,*) tagc,tagr
    if(tagc=='phi0(2)=') then
      phi0(2)=tagr
      ifrag=1
    end if
  end do
  close(10)

!-------------------------------------------------------------
! p0
!-------------------------------------------------------------
  open(10,form='formatted',status='old',&
&         file='./input/parameter.txt')
  ifrag=0
  do while(ifrag==0)
    read(10,"(a)") line
    read(line,*) tagc,tagr
    if(tagc=='p0=') then
      p0=tagr
      ifrag=1
    end if
  end do
  close(10)

  end subroutine sb_input
```

sb_random_number.f90

```
!=============================================================
! sb_random_number
!=============================================================
  subroutine sb_random_number(z)
  use module
  implicit none
! local variables
  integer(4)                  :: c,z
  real(8)                     :: x
  integer(4)                  :: i,seedsize
  integer(4),allocatable      :: seed(:)

  call random_seed(size=seedsize)
  allocate(seed(seedsize))
  call random_seed(get=seed)
  call system_clock(count=c)
  seed(1:12)=c
  call random_seed(put=seed)

  do i=1,Ncyl*Ncyl*z*3
    call random_number(x)
    rnd(i)=x
  end do

  do i=1,Ncyl*Ncyl*z*3
    rnd(i)=2.0d0*rnd(i)-1.0d0
  end do

  end subroutine sb_random_number
```

sb_mag.f90

```
!=============================================================
! sb_mag
!=============================================================
  subroutine sb_mag
  use module
  implicit none
! local variables
  integer(4)                    :: i,j,k,l,m
  real(8)                       :: Bn
! allocation
  allocate(Bp(Ncyl,Ncyl,Ncell(1),3,2))
  allocate(rnd(Ncyl*Ncyl*Ncell(1)*3))

  call sb_random_number(Ncell(1))
  do l=1,3
  do k=1,Ncell(1)
  do j=1,Ncyl
  do i=1,Ncyl
    m=(3*Ncyl*Ncell(1)*(i-1))+(3*Ncell(1)*(j-1))+3*(k-1)+l
    Bp(i,j,k,l,1)=rnd(m)
  end do
  end do
  end do
  end do

! normalization
  do k=1,Ncell(1)
  do j=1,Ncyl
  do i=1,Ncyl
    Bn=sqrt(Bp(i,j,k,1,1)**2+Bp(i,j,k,2,1)**2+Bp(i,j,k,3,1)**2)
    Bp(i,j,k,1,1)=(Bp(i,j,k,1,1)/Bn)*B(1)
    Bp(i,j,k,2,1)=(Bp(i,j,k,2,1)/Bn)*B(1)
    Bp(i,j,k,3,1)=(Bp(i,j,k,3,1)/Bn)*B(1)
  end do
  end do
  end do

  end subroutine sb_mag
```

sb_freq.f90

```
!=============================================================
! sb_freq
!=============================================================
  subroutine sb_freq
  use module
  implicit none
! local variables
  integer(4)                    :: i,j,add
! allocation
  allocate(freq(4*Nf+1))
  allocate(lambda(4*Nf+1))

!#############################################################
! split
!#############################################################
! 0.01-0.1GHz
  j=0
  do i=1,Nf+1
    freq(i)=(0.01d0*10d0**(dble(i-1)/dble(Nf)))*10**9
    j=j+1
  end do
  add=j

! 0.1-1 GHz
  do i=1,Nf
    freq(i+add)=(0.1d0*10d0**(dble(i)/dble(Nf)))*10**9
    j=j+1
  end do
  add=j

! 1-10 GHz
  do i=1,Nf
    freq(i+add)=(10d0**(dble(i)/dble(Nf)))*10**9
    j=j+1
  end do
  add=j

! 10-100 GHz
  do i=1,Nf
    freq(i+add)=(10d0*10d0**(dble(i)/dble(Nf)))*10**9
    j=j+1
  end do

!#############################################################
! frequency to wavelength
!#############################################################
  do i=1,4*Nf+1
    lambda(i)=clight/(freq(i))
  end do

  end subroutine sb_freq
```

sb_mag2.f90

```
!=============================================================
! sb_mag2
!=============================================================
  subroutine sb_mag2
  use module
  implicit none
! local variables
  integer(4)                    :: i,j,k,l,m
  real(8)                       :: Bn
! allocation
  if(Ncell(1)>=Ncell(2)) then
    allocate(rnd(Ncyl*Ncyl*Ncell(1)*3))
    allocate(Bp(Ncyl,Ncyl,Ncell(1),3,2))
  else
    allocate(rnd(Ncyl*Ncyl*Ncell(2)*3))
    allocate(Bp(Ncyl,Ncyl,Ncell(2),3,2))
  end if

!-------------------------------------------------------------
! first screen
!-------------------------------------------------------------
  call sb_random_number(Ncell(1))
  do l=1,3
  do k=1,Ncell(1)
  do j=1,Ncyl
  do i=1,Ncyl
    m=(3*Ncyl*Ncell(1)*(i-1))+(3*Ncell(1)*(j-1))+3*(k-1)+l
    Bp(i,j,k,l,1)=rnd(m)
  end do
  end do
  end do
  end do

! normalization
  do k=1,Ncell(1)
  do j=1,Ncyl
  do i=1,Ncyl
    Bn=sqrt(Bp(i,j,k,1,1)**2+Bp(i,j,k,2,1)**2+Bp(i,j,k,3,1)**2)
    Bp(i,j,k,1,1)=(Bp(i,j,k,1,1)/Bn)*B(1)
```

```
    Bp(i,j,k,2,1)=(Bp(i,j,k,2,1)/Bn)*B(1)
    Bp(i,j,k,3,1)=(Bp(i,j,k,3,1)/Bn)*B(1)
  end do
  end do
  end do

!-------------------------------------------------------------
! second screen
!-------------------------------------------------------------
  call sb_random_number(Ncell(2))
  do l=1,3
  do k=1,Ncell(2)
  do j=1,Ncyl
  do i=1,Ncyl
    m=(3*Ncyl*Ncell(2)*(i-1))+(3*Ncell(2)*(j-1))+3*(k-1)+l
    Bp(i,j,k,l,2)=rnd(m)
  end do
  end do
  end do
  end do

! normalization
  do k=1,Ncell(2)
  do j=1,Ncyl
  do i=1,Ncyl
    Bn=sqrt(Bp(i,j,k,1,2)**2+Bp(i,j,k,2,2)**2+Bp(i,j,k,3,2)**2)
    Bp(i,j,k,1,2)=(Bp(i,j,k,1,2)/Bn)*B(2)
    Bp(i,j,k,2,2)=(Bp(i,j,k,2,2)/Bn)*B(2)
    Bp(i,j,k,3,2)=(Bp(i,j,k,3,2)/Bn)*B(2)
  end do
  end do
  end do

  end subroutine sb_mag2
```

sb_phi.f90

```
!============================================================
! sb_phi
!============================================================
  subroutine sb_phi
  use module
  implicit none
! local variables
  integer(4)                    :: i,j,k
  real(8)                       :: d
! allocation
  allocate(Phicyl(Ncyl,Ncyl,4*Nf+1,2))
  allocate(RMcyl(Ncyl,Ncyl,2))
  allocate(RMave(2))
  allocate(RMsd(2))

!############################################################
! each cyl's Rotation Measure
!############################################################
  RMcyl(:,:,1)=0.0d0
  do j=1,Ncyl
  do i=1,Ncyl
  do k=1,Ncell(1)
    RMcyl(i,j,1)=RMcyl(i,j,1)+(ne(1)*Bp(i,j,k,3,1)*cellsize)
  end do
  end do
  end do

  do j=1,Ncyl
  do i=1,Ncyl
    RMcyl(i,j,1)=812.0d0*RMcyl(i,j,1)
  end do
  end do

! average of RM
  RMave(1)=0.0d0
  do j=1,Ncyl
  do i=1,Ncyl
    RMave(1)=RMave(1)+RMcyl(i,j,1)
  end do
  end do
  RMave(1)=RMave(1)/(Ncyl*Ncyl)

! SD of RM
  RMsd(1)=0.0d0
  d=0.0d0
  do j=1,Ncyl
  do i=1,Ncyl
    d=d+(RMcyl(i,j,1)-RMave(1))**2
  end do
  end do
  RMsd(1)=sqrt(d/(dble(Ncyl*Ncyl)-1.0d0))

!############################################################
! each cyl's Polarization angle
!############################################################
  do k=1,4*Nf+1
  do j=1,Ncyl
  do i=1,Ncyl
    Phicyl(i,j,k,1)=phi0(1)+RMcyl(i,j,1)*lambda(k)**2
  end do
  end do
  end do

  end subroutine sb_phi
```

sb_phi2.f90

```
!============================================================
! sb_phi2
!============================================================
  subroutine sb_phi2
  use module
  implicit none
! local variables
  integer(4)                    :: i,j,k
  real(8)                       :: d
! allocation
  allocate(Phicyl(Ncyl,Ncyl,4*Nf+1,2))
  allocate(RMcyl(Ncyl,Ncyl,2))
  allocate(RMave(3))
  allocate(RMsd(3))

!############################################################
! each cyl's Rotation Measure
!############################################################
!------------------------------------------------------------
! first screen
!------------------------------------------------------------
  RMcyl(:,:,1)=0.0d0
  do j=1,Ncyl
  do i=1,Ncyl
  do k=1,Ncell(1)
    RMcyl(i,j,1)=RMcyl(i,j,1)+(ne(1)*Bp(i,j,k,3,1)*cellsize)
  end do
  end do
  end do

  do j=1,Ncyl
  do i=1,Ncyl
```

```
    RMcyl(i,j,1)=812.0d0*RMcyl(i,j,1)
  end do
  end do

! average of RM
  RMave(1)=0.0d0
  do j=1,Ncyl
  do i=1,Ncyl
    RMave(1)=RMave(1)+RMcyl(i,j,1)
  end do
  end do
  RMave(1)=RMave(1)/(Ncyl*Ncyl)

! SD of RM
  RMsd(1)=0.0d0
  do j=1,Ncyl
  do i=1,Ncyl
    d=d+(RMcyl(i,j,1)-RMave(1))**2
  end do
  end do
  RMsd(1)=sqrt(d/(real(Ncyl*Ncyl)-1.0d0))

!-------------------------------------------------------------
! second screen
!-------------------------------------------------------------
  RMcyl(:,:,2)=0.0d0
  do j=1,Ncyl
  do i=1,Ncyl
  do k=1,Ncell(2)
    RMcyl(i,j,2)=RMcyl(i,j,2)+(ne(2)*Bp(i,j,k,3,2)*cellsize)
  end do
  end do
  end do

  do j=1,Ncyl
  do i=1,Ncyl
    RMcyl(i,j,2)=812.0d0*RMcyl(i,j,2)
  end do
  end do

! average of RM
  RMave(2)=0.0d0
  do j=1,Ncyl
  do i=1,Ncyl
    RMave(2)=RMave(2)+RMcyl(i,j,2)
  end do
  end do
  RMave(2)=RMave(2)/(Ncyl*Ncyl)

! SD of RM
  RMsd(2)=0.0d0
  d=0.0d0
  do j=1,Ncyl
  do i=1,Ncyl
    d=d+(RMcyl(i,j,2)-RMave(2))**2
  end do
  end do
  RMsd(2)=sqrt(d/(dble(Ncyl*Ncyl)-1.0d0))

!############################################################
! each cyl's Polarization angle
!############################################################
!-------------------------------------------------------------
! first screen
!-------------------------------------------------------------
  do k=1,4*Nf+1
  do j=1,Ncyl
  do i=1,Ncyl
    Phicyl(i,j,k,1)=phi0(1)+RMcyl(i,j,1)*lambda(k)**2
  end do
  end do
  end do

!-------------------------------------------------------------
! second screen + first screen
!-------------------------------------------------------------
  do k=1,4*Nf+1
  do j=1,Ncyl
  do i=1,Ncyl
    Phicyl(i,j,k,2)=phi0(2)+RMcyl(i,j,1)*lambda(k)**2 &
&                  +RMcyl(i,j,2)*lambda(k)**2
  end do
  end do
  end do

  end subroutine sb_phi2
```

sb_poli.f90

```
!=============================================================
! sb_poli
!=============================================================
  subroutine sb_poli
  use module
  implicit none
! local variables
  integer(4)                    :: i,j,k
! allocation
  allocate(PolI(4*Nf+1,3))
  allocate(FPOL(4*Nf+1))
  allocate(ReEuler(4*Nf+1),ImEuler(4*Nf+1))

  ReEuler(:)=0.0d0
  do k=1,4*Nf+1
  do j=1,Ncyl
  do i=1,Ncyl
    ReEuler(k)=cos(2*Phicyl(i,j,k,1))+ReEuler(k)
  end do
  end do
  end do

  ImEuler(:)=0.0d0
  do k=1,4*Nf+1
  do j=1,Ncyl
  do i=1,Ncyl
    ImEuler(k)=sin(2*Phicyl(i,j,k,1))+ImEuler(k)
  end do
  end do
  end do

  do k=1,4*Nf+1
    PolI(k,1)=sqrt(ReEuler(k)**2+ImEuler(k)**2)
    PolI(k,1)=(CPolI(1)*freq(k)**alpha(1)*PolI(k,1))/dble(Ncyl*Ncyl)
  end do

  do k=1,4*Nf+1
    PolI(k,3)=PolI(k,1)
  end do

  do k=1,4*Nf+1
    FPOL(k)=p0*PolI(k,1)/(CPolI(1)*freq(k)**alpha(1))
  end do

  end subroutine sb_poli
```

sb_poli2.f90

```
!=============================================================
! sb_poli2
!=============================================================
  subroutine sb_poli2
  use module
  implicit none
! local variables
  integer(4)                    :: i,j,k
  real(8)                       :: NFlux(4*Nf+1,2)
! allocation
  allocate(PolI(4*Nf+1,3))
  allocate(FPOL(4*Nf+1))
  allocate(ReEuler(4*Nf+1),ImEuler(4*Nf+1))

!############################################################
! Normarized Flux
!############################################################
  do k=1,4*Nf+1
    NFlux(k,1)=(CPolI(1)*freq(k)**alpha(1))/dble(Ncyl*Ncyl)
    NFlux(k,2)=(CPolI(2)*freq(k)**alpha(2))/dble(Ncyl*Ncyl)
  enddo

!############################################################
! Polarization intensity
!############################################################
  ReEuler(:)=0.0d0
  do k=1,4*Nf+1
  do j=1,Ncyl
  do i=1,Ncyl
    ReEuler(k)=NFlux(k,1)*cos(2*Phicyl(i,j,k,1)) &
&             +NFlux(k,2)*cos(2*Phicyl(i,j,k,2))+ReEuler(k)
  enddo
  enddo
  enddo

  ImEuler(:)=0.0d0
  do k=1,4*Nf+1
  do j=1,Ncyl
  do i=1,Ncyl
    ImEuler(k)=NFlux(k,1)*sin(2*Phicyl(i,j,k,1)) &
&             +NFlux(k,2)*sin(2*Phicyl(i,j,k,2))+ImEuler(k)
  enddo
  enddo
  enddo

  do k=1,4*Nf+1
    PolI(k,3)=sqrt(ReEuler(k)**2+ImEuler(k)**2)
  enddo

  do k=1,4*Nf+1
    FPOL(k)=p0*PolI(k,3)/((NFlux(k,1)+NFlux(k,2))*dble(Ncyl*Ncyl))
  enddo

  end subroutine sb_poli2
```

sb_histogram.f90

```
!=============================================================
! sb_histogram
!=============================================================
  subroutine sb_histogram(x,y)
  use module
  implicit none
! arguments
  integer(4) :: x,y
! local variables
  integer(4) :: i,j,p,nrm
! allocation
  allocate(hist(-500:500))
  hist(:)=0

  do i=1,x
  do j=1,y
    nrm=nint(RMcyl(i,j,1)/10.0d0)
    hist(nrm)=hist(nrm)+1
  end do
  end do

  end subroutine sb_histogram
```

sb_plot.f90

```
!=============================================================
! sb_plot
!=============================================================
  subroutine sb_plot
  use module
  implicit none
! local variables
  integer(4)                    :: status,system

  status=system("gnuplot "//" ./plot/fpol_freq.plt")
  status=system("gnuplot "//" ./plot/histogram.plt")
  status=system("gnuplot "//" ./plot/RM.plt")

  end subroutine sb_plot
```

A.3.2. IFD+IFD model

We attached the program of the IFD+IFD depolarization model. If you carry out the program, you have to store the source codes as follows.

Directory structure

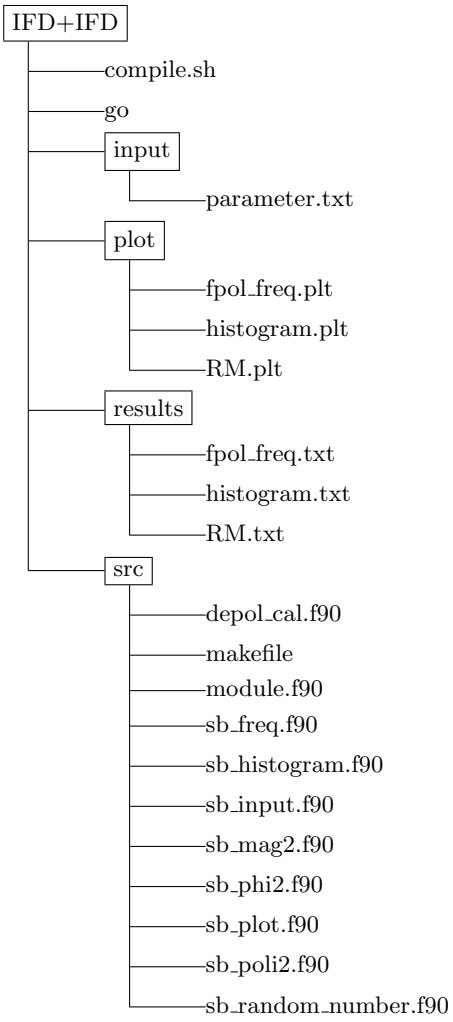

compile.sh

```
#!/bin/bash
  cd ./src/
  if [ "$1" = "clean" ] ; then
    make clean
    rm ../go
  else
    make
    mv ./go ..
  fi
  cd ..

  exit 0
```

parameter.txt

```
sc= 2                      2:IFD+IFD
----IFD(first_component) 0
B(2)= 0.2d0             magnetic field strength [uG]
ne(2)= 0.001d0          electron density [cm^-3]
Ncyl= 10                number of x=y cylinders
Ncell(2)= 100           number of cells
cellsize= 5             cellsize [kpc]
Nf= 200                 number of frequency points
CV(2)= 1.0d0            coefficient of emission from vertical B
CV(3)= 0.0d0            coefficient of emission from random B
p0= 0.73d0              intrinsic FPOL
----IFD(second_component) 0
B(1)= 2.3d0             magnetic field strength [uG]
ne(1)= 0.003d0          electron density [cm^-3]
Ncell(1)= 120          number of cells
CV(1)= 3d0             coefficient of emission from vertical B
alpha(1)= -0.8d0       spectral index of emission from vertical B
alpha(2)= -0.8d0       spectral index of emission from random B
```

fpol_freq.plt

```
clear
reset
set terminal postscript eps enhanced
set output 'fpol_freq.eps'

set xlabel offset 0,-1
set bmargin 6
set lmargin 12
set xlabel font "Helvetica,28" "Frequency [GHz]"
set ylabel  font "Helvetica,28" "Fractional polarization"\
offset -2

#set label 1 at graph -0.005,-0.0345 "0.3" font "Helvetica,28"
set label 2 at graph 1.012,-0.0345 "0" font "Helvetica,28"

set format x "{%.0l}"
set xtics 10 font "Helvetica,28"
set ytics 0.1 font "Helvetica,28"
set mytic

set key at graph 0.35,0.95
set key font "Helvetica,26"
set key spacing 2

set logscale x
#set logscale y
set xrange [1*1E09:10*1e09]
set yrange [0:0.8]

set pointsize 2
set bar 2

plot "./results/fpol_freq.txt" index 0 using 1:2 title ""\
with lines

set terminal aqua
set output
```

histogram.plt

```
clear
reset
set terminal postscript eps enhanced
set output 'histogram.eps'

set bmargin 6
set lmargin 12
```

```
set xlabel font "Helvetica,28" "RM [rad m^{-2}]" offset 0,-2
set ylabel font "Helvetica,28" "Number of pixels" offset -2

set xtics 20 font "Helvetica,28" offset 0,-1
set ytics 50 font "Helvetica,28"

set xrange [-100:100]

plot "./results/histogram.txt" index 0 using 1:2 title ""\
with boxes

set terminal aqua
set output
```

RM.plt

```
clear
reset
set terminal postscript eps enhanced color
set output 'RM.eps'
set pm3d corners2color c1
set pm3d map
set size ratio 1

set cbrange[-20:20]
set palette defined (-20 "blue", 0 "white", 20 "red")

splot './results/RM.txt' title ""

set terminal aqua
set output
```

makefile

```
TARGET = go
OBJECTS = module.o sb_input.o sb_freq.o sb_random_number.o \
sb_mag2.o sb_phi2.o \
sb_poli2.o sb_histogram.o sb_plot.o depol_cal.o
MOD_FILES  = module.mod
FC = gfortran

FFLAGS += -fimplicit-none
#LDFLAGS +=

.SUFFIXES : .o .f90
.f90.o:
        ${FC} -c $<
${TARGET} : ${OBJECTS}
        ${FC} -o $@ ${OBJECTS} ${LDFLAGS} ${FFLAGS}
.PHONY: clean
clean:
        ${RM} ${TARGET} ${OBJECTS} ${MOD_FILES}
# above space is tab space
```

depol_cal.f90

```
!=============================================================
! IFD+IFD Version-140205 Produced by Takeaki Ozawa
!=============================================================
  program depol_cal
  use module
  implicit none
! local variables
  integer(4)                    :: i,j,k

!#############################################################
! calculation
!#############################################################
  call sb_input
  call sb_freq
  select case(sc)
    case(2); call sb_mag2; call sb_phi2; call sb_poli2
  end select

!#############################################################
! results
!#############################################################
  print "(80('*'))"
  print "('*',a,t80,'*')",' IFD+IFD'
  print "('*',a,f6.1,a,f6.1,t80,'*')", &
&  ' RMave(1)    (only backside)=',RMave(1),' RMsd(1)=',RMsd(1)
  print "('*',a,f6.1,a,f6.1,t80,'*')", &
&  ' RMave(2)    (only foreside)=',RMave(2),' RMsd(2)=',RMsd(2)
  print "(80('*'))"

!-------------------------------------------------------------
! fpol-freq.txt
!-------------------------------------------------------------
  open(10,status='unknown',file='./results/fpol_freq.txt')
  write(10,"(3(a))") '#',' frequency','  FPOL'
  do k=1,4*Nf+1
    write(10,"(e12.5,2x,f5.3)") freq(k),FPOL(k)
  end do
  close(10)

!-------------------------------------------------------------
! RM.txt
!-------------------------------------------------------------
  open(10,status='unknown',file='./results/RM.txt')
  do j=1,Ncyl
  do i=1,Ncyl
    write(10,"(2(2x,i3),3x,f6.1)") i,j,RMcyl(i,j,1,1)
  end do
  write(10,*)
  end do
  if(sc==2) then
    do j=1,Ncyl
    do i=1,Ncyl
!      write(10,"(2(2x,i3),3x,f6.1)") i,j,RMcyl(i,j,1)
    end do
    write(10,*)
    end do
  end if
  close(10)

!-------------------------------------------------------------
! histogram.txt
!-------------------------------------------------------------
  call sb_histogram(Ncyl,Ncyl)
  open(10,status='unknown',file='./results/histogram.txt')
  do i=-5000,5000,10
  if(i==0) then
    write(10,"(i5,i4)") i,hist(i)
  else
    write(10,"(i5,i4)") i,hist(i/10)
  end if
  end do
  close(10)

!#############################################################
! plot
!#############################################################
  call sb_plot
```

```
  end program depol_cal
```

module.f90

```
!=============================================================
! module
!=============================================================
  module module
  implicit none

!#############################################################
! global variables
!#############################################################
! magnetic field strength
  real(8),allocatable,save      :: B(:)
  real(8),allocatable,save      :: Bp(:,:,:,:,:)
! electron density
  real(8),allocatable,save      :: ne(:)
! polarization angle
  real(8),allocatable,save      :: Phicyl(:,:,:,:,:)
  real(8),allocatable,save      :: RMcyl(:,:,:,:)
  real(8),allocatable,save      :: RMave(:)
  real(8),allocatable,save      :: RMsd(:)
  real(8),allocatable,save      :: Phi0(:,:,:,:)
! polarization intensity
  real(8),allocatable,save      :: PolI(:,:)
  real(8),allocatable,save      :: ReEuler(:,:,:)
  real(8),allocatable,save      :: ImEuler(:,:,:)
  real(8),allocatable,save      :: CV(:)
  real(8),allocatable,save      :: ec(:,:,:,:)
  real(8),allocatable,save      :: FPOL(:)
  real(8),save                  :: p0
! frequency
  integer(4),save               :: Nf
  real(8),allocatable,save      :: freq(:)
  real(8),allocatable,save      :: lambda(:)
! synchrotron emission
  real(8),allocatable,save      :: alpha(:)
! cell
  integer(4),save               :: Ncyl
  integer(4),allocatable,save   :: Ncell(:)
  real(8),save                  :: cellsize
  real(8),allocatable,save      :: rnd(:)
! RM screen
  integer(4),save               :: sc
! results
  integer(4),allocatable,save   :: hist(:)

!#############################################################
! constants
!#############################################################
  real(8),parameter             :: pi=3.14159265358979d0
  real(8),parameter             :: radian=57.2957795130823d0
  real(8),parameter             :: clight=2.9979245800D+08

!#############################################################
! function
!#############################################################
  contains
! negauss
  function negauss(i,j) result(func)
  implicit none
! arguments
  integer(4),intent(in)         :: i,j
! local variables
  real(8)                       :: x,y
  real(8)                       :: func

  x=(dble(i)/4.0d0)-dble(j)
  y=((1d0/3d0)*(dble(i)/2.0d0))
  func=(1.0d0/sqrt(2*pi*y**2))*exp(-(x**2/(2.0*y**2)))

  end function negauss

  end module module
```

sb_input.f90

```
!=============================================================
! sb_input
!=============================================================
  subroutine sb_input
  use module
  implicit none
! local variables
  integer(4)                    :: ifrag
  real(8)                       :: tagr
  character(10)                 :: tagc
  character(100)                :: line
! allocation
  allocate(B(2))
  allocate(ne(2))
  allocate(alpha(2))
  allocate(ncell(2))
  allocate(CV(3))

!#############################################################
! input
!#############################################################
!-------------------------------------------------------------
! magnetic field strength
!-------------------------------------------------------------
  open(10,form='formatted',status='old',&
&         file='./input/parameter.txt')
  ifrag=0
  do while(ifrag==0)
    read(10,"(a)") line
    read(line,*) tagc,tagr
    if(tagc=='B(1)=') then
      B(1)=tagr
      ifrag=1
    end if
  end do
  close(10)

!-------------------------------------------------------------
! electron density
!-------------------------------------------------------------
  open(10,form='formatted',status='old',&
&         file='./input/parameter.txt')
  ifrag=0
  do while(ifrag==0)
    read(10,"(a)") line
    read(line,*) tagc,tagr
    if(tagc=='ne(1)=') then
      ne(1)=tagr
      ifrag=1
    end if
  end do
  close(10)

!-------------------------------------------------------------
! number of cylinders
!-------------------------------------------------------------
  open(10,form='formatted',status='old',&
&         file='./input/parameter.txt')
```

```
  ifrag=0
  do while(ifrag==0)
    read(10,"(a)") line
    read(line,*) tagc,tagr
    if(tagc=='Ncyl=') then
      Ncyl=int(tagr)
      ifrag=1
    end if
  end do
  close(10)

!-------------------------------------------------------------
! number of cells
!-------------------------------------------------------------
  open(10,form='formatted',status='old',&
&         file='./input/parameter.txt')
  ifrag=0
  do while(ifrag==0)
    read(10,"(a)") line
    read(line,*) tagc,tagr
    if(tagc=='Ncell(1)=') then
      Ncell(1)=int(tagr)
      ifrag=1
    end if
  end do
  close(10)

!-------------------------------------------------------------
! cellsize
!-------------------------------------------------------------
  open(10,form='formatted',status='old',&
&         file='./input/parameter.txt')
  ifrag=0
  do while(ifrag==0)
    read(10,"(a)") line
    read(line,*) tagc,tagr
    if(tagc=='cellsize=') then
      cellsize=tagr
      ifrag=1
    end if
  end do
  close(10)

!-------------------------------------------------------------
! Nf
!-------------------------------------------------------------
  open(10,form='formatted',status='old',&
&         file='./input/parameter.txt')
  ifrag=0
  do while(ifrag==0)
    read(10,"(a)") line
    read(line,*) tagc,tagr
    if(tagc=='Nf=') then
      Nf=int(tagr)
      ifrag=1
    end if
  end do
  close(10)

!-------------------------------------------------------------
! alpha(1)
!-------------------------------------------------------------
  open(10,form='formatted',status='old',&
&         file='./input/parameter.txt')
  ifrag=0
  do while(ifrag==0)
    read(10,"(a)") line
    read(line,*) tagc,tagr
    if(tagc=='alpha(1)=') then
      alpha(1)=tagr
      ifrag=1
    end if
  end do
  close(10)

!-------------------------------------------------------------
! CV(1)
!-------------------------------------------------------------
  open(10,form='formatted',status='old',&
&         file='./input/parameter.txt')
  ifrag=0
  do while(ifrag==0)
    read(10,"(a)") line
    read(line,*) tagc,tagr
    if(tagc=='CV(1)=') then
      CV(1)=tagr
      ifrag=1
    end if
  end do
  close(10)

!-------------------------------------------------------------
! CV(2)
!-------------------------------------------------------------
  open(10,form='formatted',status='old',&
&         file='./input/parameter.txt')
  ifrag=0
  do while(ifrag==0)
    read(10,"(a)") line
    read(line,*) tagc,tagr
    if(tagc=='CV(2)=') then
      CV(2)=tagr
      ifrag=1
    end if
  end do
  close(10)

!-------------------------------------------------------------
! sc
!-------------------------------------------------------------
  open(10,form='formatted',status='old',&
&         file='./input/parameter.txt')
  ifrag=0
  do while(ifrag==0)
    read(10,"(a)") line
    read(line,*) tagc,tagr
    if(tagc=='sc=') then
      sc=int(tagr)
      ifrag=1
    end if
  end do
  close(10)

!-------------------------------------------------------------
! number of second cells
!-------------------------------------------------------------
  open(10,form='formatted',status='old',&
&         file='./input/parameter.txt')
  ifrag=0
  do while(ifrag==0)
    read(10,"(a)") line
    read(line,*) tagc,tagr
    if(tagc=='Ncell(2)=') then
      Ncell(2)=int(tagr)
      ifrag=1
    end if
  end do
  close(10)
```

```
!-------------------------------------------------------------
! 2nd sc. magnetic field strength
!-------------------------------------------------------------
  open(10,form='formatted',status='old',&
&         file='./input/parameter.txt')
  ifrag=0
  do while(ifrag==0)
    read(10,"(a)") line
    read(line,*) tagc,tagr
    if(tagc=='B(2)=') then
      B(2)=tagr
      ifrag=1
    end if
  end do
  close(10)

!-------------------------------------------------------------
! 2nd sc. electron density
!-------------------------------------------------------------
  open(10,form='formatted',status='old',&
&         file='./input/parameter.txt')
  ifrag=0
  do while(ifrag==0)
    read(10,"(a)") line
    read(line,*) tagc,tagr
    if(tagc=='ne(2)=') then
      ne(2)=tagr
      ifrag=1
    end if
  end do
  close(10)

!-------------------------------------------------------------
! CV(3)
!-------------------------------------------------------------
  open(10,form='formatted',status='old',&
&         file='./input/parameter.txt')
  ifrag=0
  do while(ifrag==0)
    read(10,"(a)") line
    read(line,*) tagc,tagr
    if(tagc=='CV(3)=') then
      CV(3)=tagr
      ifrag=1
    end if
  end do
  close(10)

!-------------------------------------------------------------
! alpha(2)
!-------------------------------------------------------------
  open(10,form='formatted',status='old',&
&         file='./input/parameter.txt')
  ifrag=0
  do while(ifrag==0)
    read(10,"(a)") line
    read(line,*) tagc,tagr
    if(tagc=='alpha(2)=') then
      alpha(2)=tagr
      ifrag=1
    end if
  end do
  close(10)

!-------------------------------------------------------------
! p0
!-------------------------------------------------------------
  open(10,form='formatted',status='old',&
&         file='./input/parameter.txt')
  ifrag=0
  do while(ifrag==0)
    read(10,"(a)") line
    read(line,*) tagc,tagr
    if(tagc=='p0=') then
      p0=tagr
      ifrag=1
    end if
  end do
  close(10)

  end subroutine sb_input
```

sb_freq.f90

```
!=============================================================
! sb_freq
!=============================================================
  subroutine sb_freq
  use module
  implicit none
! local variables
  integer(4)                    :: i,j,add
! allocation
  allocate(freq(4*Nf+1))
  allocate(lambda(4*Nf+1))

!#############################################################
! split
!#############################################################
! 0.01-0.1GHz
  j=0
  do i=1,Nf+1
    freq(i)=(0.01d0*10d0**(dble(i-1)/dble(Nf)))*10**9
    j=j+1
  end do
  add=j

! 0.1-1 GHz
  do i=1,Nf
    freq(i+add)=(0.1d0*10d0**(dble(i)/dble(Nf)))*10**9
    j=j+1
  end do
  add=j

! 1-10 GHz
  do i=1,Nf
    freq(i+add)=(10d0**(dble(i)/dble(Nf)))*10**9
    j=j+1
  end do
  add=j

! 10-100 GHz
  do i=1,Nf
    freq(i+add)=(10d0*10d0**(dble(i)/dble(Nf)))*10**9
    j=j+1
  end do

!#############################################################
! frequency to wavelength
!#############################################################
  do i=1,4*Nf+1
    lambda(i)=clight/(freq(i))
  end do

  end subroutine sb_freq
```

sb_random_number.f90

```
!=============================================================
! sb_random_number
!=============================================================
  subroutine sb_random_number(z)
  use module
  implicit none
! local variables
  integer(4)                    :: c,z
  real(8)                       :: x
  integer(4)                    :: i,seedsize
  integer(4),allocatable        :: seed(:)

  call random_seed(size=seedsize)
  allocate(seed(seedsize))
  call random_seed(get=seed)
  call system_clock(count=c)
  seed(1:12)=c
  call random_seed(put=seed)

  do i=1,Ncyl*Ncyl*z*3
    call random_number(x)
    rnd(i)=x
  enddo

  do i=1,Ncyl*Ncyl*z*3
    rnd(i)=2.0d0*rnd(i)-1.0d0
  enddo

  end subroutine sb_random_number
```

sb_mag2.f90

```
!=============================================================
! sb_mag2
!=============================================================
  subroutine sb_mag2
  use module
  implicit none
! local variables
  integer(4)                    :: i,j,k,l,m
  real(8)                       :: Bn
  real(8)                       :: x,y,z
! allocation
  if(Ncell(1)>=Ncell(2)) then
    allocate(Bp(Ncyl,Ncyl,Ncell(1),3,2))
    allocate(rnd(Ncyl*Ncyl*Ncell(1)*3))
    allocate(phi0(Ncyl,Ncyl,Ncell(1),2))
    allocate(ec(Ncyl,Ncyl,Ncell(1),2))
  else
    allocate(rnd(Ncyl*Ncyl*Ncell(2)*3))
    allocate(phi0(Ncyl,Ncyl,Ncell(2),2))
    allocate(ec(Ncyl,Ncyl,Ncell(2),2))
    allocate(Bp(Ncyl,Ncyl,Ncell(2),3,2))
  end if

!############################################################
! IFD
!############################################################
  call sb_random_number(Ncell(1))
  do l=1,3
  do k=1,Ncell(1)
  do j=1,Ncyl
  do i=1,Ncyl
    m=(3*Ncyl*Ncell(1)*(i-1))+(3*Ncell(1)*(j-1))+3*(k-1)+l
    Bp(i,j,k,l,1)=rnd(m)
  enddo
  enddo
  enddo

! normalization
  do k=1,Ncell(1)
  do j=1,Ncyl
  do i=1,Ncyl
    Bn=sqrt(Bp(i,j,k,1,1)**2+Bp(i,j,k,2,1)**2+Bp(i,j,k,3,1)**2)
    Bp(i,j,k,1,1)=(Bp(i,j,k,1,1)/Bn)*B(1)
    Bp(i,j,k,2,1)=(Bp(i,j,k,2,1)/Bn)*B(1)
    Bp(i,j,k,3,1)=(Bp(i,j,k,3,1)/Bn)*B(1)
  enddo
  enddo
  enddo

! emission coefficient
  do k=1,Ncell(1)
  do j=1,Ncyl
  do i=1,Ncyl
    ec(i,j,k,1)=sqrt(Bp(i,j,k,1,1)**2+Bp(i,j,k,2,1)**2)/B(1)
  enddo
  enddo
  enddo

! intrinsic polarization angle
  do k=1,Ncell(1)
  do j=1,Ncyl
  do i=1,Ncyl
    Phi0(i,j,k,1)=acos(Bp(i,j,k,1,1)/sqrt(Bp(i,j,k,1,1)**2 &
&              +Bp(i,j,k,2,1)**2))+(pi/2.0d0)
  enddo
  enddo
  enddo

!############################################################
! IFD
!############################################################
  call sb_random_number(Ncell(2))
  do l=1,3
  do k=1,Ncell(2)
  do j=1,Ncyl
  do i=1,Ncyl
    m=(3*Ncyl*Ncell(2)*(i-1))+(3*Ncell(2)*(j-1))+3*(k-1)+l
    Bp(i,j,k,l,2)=rnd(m)
  enddo
  enddo
  enddo
  enddo

! normalization
  do k=1,Ncell(2)
  do j=1,Ncyl
  do i=1,Ncyl
    Bn=sqrt(Bp(i,j,k,1,2)**2+Bp(i,j,k,2,2)**2+Bp(i,j,k,3,2)**2)
    Bp(i,j,k,1,2)=(Bp(i,j,k,1,2)/Bn)*B(2)
    Bp(i,j,k,2,2)=(Bp(i,j,k,2,2)/Bn)*B(2)
    Bp(i,j,k,3,2)=(Bp(i,j,k,3,2)/Bn)*B(2)
  enddo
  enddo
  enddo

! emission coefficient
  do k=1,Ncell(2)
  do j=1,Ncyl
  do i=1,Ncyl
    ec(i,j,k,2)=sqrt(Bp(i,j,k,1,2)**2+Bp(i,j,k,2,2)**2)/B(2)
  enddo
  enddo
```

```
  enddo

! intrinsic polarization angle
  do k=1,Ncell(2)
  do j=1,Ncyl
  do i=1,Ncyl
    Phi0(i,j,k,2)=acos(Bp(i,j,k,1,2)/sqrt(Bp(i,j,k,1,2)**2 &
&             +Bp(i,j,k,2,2)**2))+(pi/2.0d0)
  enddo
  enddo
  enddo

! intrinsic polarization angle
  do k=1,Ncell(1)
  do j=1,Ncyl
  do i=1,Ncyl
    Phi0(i,j,k,1)=acos(Bp(i,j,k,1,1)/sqrt(Bp(i,j,k,1,1)**2 &
&             +Bp(i,j,k,2,1)**2))+(pi/2.0d0)
  enddo
  enddo
  enddo

  end subroutine sb_mag2
```

sb_phi2.f90

```
!=============================================================
! sb_phi2
!=============================================================
  subroutine sb_phi2
  use module
  implicit none
! local variables
  integer(4)                    :: i,j,k,l
  real(8)                       :: d
! allocation
  if(Ncell(1)>=Ncell(2)) then
    allocate(Phicyl(Ncyl,Ncyl,Ncell(1)+1,4*Nf+1,2))
    allocate(RMcyl(Ncyl,Ncyl,Ncell(1)+1,2))
  else
    allocate(Phicyl(Ncyl,Ncyl,Ncell(2)+1,4*Nf+1,2))
    allocate(RMcyl(Ncyl,Ncyl,Ncell(2)+1,2))
  endif
  allocate(RMave(3))
  allocate(RMsd(3))

!############################################################
! each cyl's Rotation Measure
! when k=1, sum up until Ncell
!############################################################
!!! foreside + backside !!!
  RMcyl(:,:,:,1)=0.0d0
  do k=1,Ncell(1)
  do j=1,Ncyl
  do i=1,Ncyl
  do l=1,Ncell(1)-(k-1)
    RMcyl(i,j,k,1)=(ne(1)*Bp(i,j,l,3,1)*cellsize)+RMcyl(i,j,k,1)
  enddo
  enddo
  enddo
  enddo

! average of RM for a backside component (k=1)
  RMave(1)=0.0d0
  do j=1,Ncyl
  do i=1,Ncyl
    RMave(1)=(812.0d0*RMcyl(i,j,1,1))+RMave(1)
  end do
  end do
  RMave(1)=RMave(1)/(Ncyl*Ncyl)
! SD of RM
  RMsd(1)=0.0d0
  d=0.0d0
  do j=1,Ncyl
  do i=1,Ncyl
    d=d+((812.0d0*RMcyl(i,j,1,1))-RMave(1))**2
  end do
  end do
  RMsd(1)=sqrt(d/(dble(Ncyl*Ncyl)-1.0d0))

  do k=1,Ncell(1)
  do j=1,Ncyl
  do i=1,Ncyl
  do l=1,Ncell(2)
    RMcyl(i,j,k,1)=(ne(2)*Bp(i,j,l,3,2)*cellsize)+RMcyl(i,j,k,1)
  enddo
  enddo
  enddo
  enddo

!!! only foreside !!!
  do k=1,Ncell(2)
  do j=1,Ncyl
  do i=1,Ncyl
  do l=1,Ncell(2)-(k-1)
    RMcyl(i,j,k,2)=(ne(2)*Bp(i,j,l,3,2)*cellsize)+RMcyl(i,j,k,2)
  enddo
  enddo
  enddo
  enddo

  do k=1,Ncell(1)
  do j=1,Ncyl
  do i=1,Ncyl
    RMcyl(i,j,k,1)=812.0d0*RMcyl(i,j,k,1)
  enddo
  enddo
  enddo

  do k=1,Ncell(2)
  do j=1,Ncyl
  do i=1,Ncyl
    RMcyl(i,j,k,2)=812.0d0*RMcyl(i,j,k,2)
  enddo
  enddo
  enddo

! average of RM for a foreside component
  RMave(2)=0.0d0
  do j=1,Ncyl
  do i=1,Ncyl
    RMave(2)=RMcyl(i,j,1,2)+RMave(2)
  end do
  end do
  RMave(2)=RMave(2)/(Ncyl*Ncyl)

! SD of RM
  RMsd(2)=0.0d0
  d=0.0d0
  do j=1,Ncyl
  do i=1,Ncyl
    d=d+(RMcyl(i,j,1,2)-RMave(2))**2
  end do
  end do
  RMsd(2)=sqrt(d/(dble(Ncyl*Ncyl)-1.0d0))

!############################################################
```

```
! each cyl's Polarization angle
!############################################################
  do l=1,4*Nf+1
  do k=1,Ncell(1)
  do j=1,Ncyl
  do i=1,Ncyl
    Phicyl(i,j,k,l,1)=RMcyl(i,j,k,1)*lambda(l)**2
  enddo
  enddo
  enddo
  enddo

  do l=1,4*Nf+1
  do k=1,Ncell(2)
  do j=1,Ncyl
  do i=1,Ncyl
    Phicyl(i,j,k,l,2)=RMcyl(i,j,k,2)*lambda(l)**2
  enddo
  enddo
  enddo
  enddo

  end subroutine sb_phi2
```

sb_poli2.f90

```
!============================================================
! sb_poli2
!============================================================
  subroutine sb_poli2
  use module
  implicit none
! local variables
  integer(4)                    :: i,j,k,l
  real(8)                       :: NFlux(4*Nf+1,2)
  real(8)                       :: NRFlux(4*Nf+1,2)
  real(8)                       :: Ftotal(4*Nf+1)
! allocation
  allocate(PolI(4*Nf+1,3))
  allocate(FPOL(4*Nf+1))
  allocate(ReEuler(Ncyl+1,Ncyl+1,4*Nf+1))
  allocate(ImEuler(Ncyl+1,Ncyl+1,4*Nf+1))

!############################################################
! Normarized Flux
!############################################################
  do l=1,4*Nf+1
    NFlux(l,1)=(CV(1)*freq(l)**alpha(1))/dble(Ncyl*Ncyl*Ncell(1))
    NRFlux(l,1)=(CV(3)*freq(l)**alpha(2))/dble(Ncyl*Ncyl*Ncell(1))
  enddo

  do l=1,4*Nf+1
    NFlux(l,2)=(CV(2)*freq(l)**alpha(1))/dble(Ncyl*Ncyl*Ncell(2))
    NRFlux(l,2)=(CV(3)*freq(l)**alpha(2))/dble(Ncyl*Ncyl*Ncell(2))
  enddo

!############################################################
! Polarization intensity
!############################################################
  ReEuler(:,:,:)=0.0d0
  do l=1,4*Nf+1
  do j=1,Ncyl
  do i=1,Ncyl
  do k=1,Ncell(1)
    ReEuler(i,j,l)=NFlux(l,1)*cos(2*Phicyl(i,j,k,l,1)) &
&                 +ec(i,j,k,1)*NRFlux(l,1) &
&                 *cos(2*(Phi0(i,j,k,1)+Phicyl(i,j,k,l,1))) &
&                 +ReEuler(i,j,l)
  enddo
  enddo
  enddo
  enddo

  do l=1,4*Nf+1
  do j=1,Ncyl
  do i=1,Ncyl
  do k=1,Ncell(2)
    ReEuler(i,j,l)=NFlux(l,2)*cos(2*Phicyl(i,j,k,l,2)) &
&                 +ec(i,j,k,2)*NRFlux(l,2) &
&                 *cos(2*(Phi0(i,j,k,2)+Phicyl(i,j,k,l,2))) &
&                 +ReEuler(i,j,l)
  enddo
  enddo
  enddo
  enddo

  ImEuler(:,:,:)=0.0d0
  do l=1,4*Nf+1
  do j=1,Ncyl
  do i=1,Ncyl
  do k=1,Ncell(1)
    ImEuler(i,j,l)=NFlux(l,1)*sin(2*Phicyl(i,j,k,l,1)) &
&                 +ec(i,j,k,1)*NRFlux(l,1) &
&                 *sin(2*(Phi0(i,j,k,1)+Phicyl(i,j,k,l,1))) &
&                 +ImEuler(i,j,l)
  enddo
  enddo
  enddo
  enddo

  do l=1,4*Nf+1
  do j=1,Ncyl
  do i=1,Ncyl
  do k=1,Ncell(2)
    ImEuler(i,j,l)=NFlux(l,2)*sin(2*Phicyl(i,j,k,l,2)) &
&                 +ec(i,j,k,2)*NRFlux(l,2) &
&                 *sin(2*(Phi0(i,j,k,2)+Phicyl(i,j,k,l,2))) &
&                 +ImEuler(i,j,l)
  enddo
  enddo
  enddo
  enddo

  do l=1,4*Nf+1
  do j=1,Ncyl
  do i=1,Ncyl
  ReEuler(Ncyl+1,Ncyl+1,l)=ReEuler(i,j,l)+ReEuler(Ncyl+1,Ncyl+1,l)
  ImEuler(Ncyl+1,Ncyl+1,l)=ImEuler(i,j,l)+ImEuler(Ncyl+1,Ncyl+1,l)
  enddo
  enddo
  enddo

  do l=1,4*Nf+1
    PolI(l,1)=sqrt(ReEuler(Ncyl+1,Ncyl+1,l)**2 &
&                 +ImEuler(Ncyl+1,Ncyl+1,l)**2)
    PolI(l,3)=PolI(l,1)
  enddo

!############################################################
! Fractional polarization
!############################################################
  Ftotal(:)=0.0d0
  do l=1,4*Nf+1
  do j=1,Ncyl
  do i=1,Ncyl
  do k=1,Ncell(1)
    Ftotal(l)=ec(i,j,k,1)*NRFlux(l,1)+Ftotal(l)
```

```
  enddo
  enddo
  enddo
  enddo

  do l=1,4*Nf+1
  do j=1,Ncyl
  do i=1,Ncyl
  do k=1,Ncell(2)
    Ftotal(l)=ec(i,j,k,2)*NRFlux(l,2)+Ftotal(l)
  enddo
  enddo
  enddo
  enddo

  do l=1,4*Nf+1
    Ftotal(l)=(CV(1)*freq(l)**alpha(1))+(CV(2)*freq(l)**alpha(1))&
&               +Ftotal(l)
  enddo

  do l=1,4*Nf+1
    FPOL(l)=p0*(PolI(1,3)/Ftotal(l))
  enddo

  end subroutine sb_poli2
```

sb_histogram.f90

```
!============================================================
! RM histogram
!============================================================
  subroutine sb_histogram(x,y)
  use module
  implicit none
! arguments
  integer(4) :: x,y
! local variables
  integer(4) :: i,j,k,p,nrm
! allocation
  allocate(hist(-500:500))
  hist(:)=0

  do i=1,x
  do j=1,y
    nrm=nint(RMcyl(i,j,1,1)/10.0d0)
    hist(nrm)=hist(nrm)+1
  end do
  end do

  end subroutine sb_histogram
```

sb_plot.f90

```
!============================================================
! sb_plot
!============================================================
  subroutine sb_plot
  use module
  implicit none
! local variables
  integer(4)                    :: status,system

  status=system("gnuplot "//" ./plot/fpol_freq.plt")
  status=system("gnuplot "//" ./plot/histogram.plt")
  status=system("gnuplot "//" ./plot/RM.plt")

  end subroutine sb_plot
```

References

Abell, G. O. 1958, ApJS, 3, 211

Ackermann, M., Ajello, M., Albert, A., et al. 2014, ApJ, 787, 18

Abell, G. O., Corwin, H. G., Jr., & Olowin, R. P. 1989, ApJS, 70, 1

Arshakian, T. G., & Beck, R. 2011, MNRAS, 418, 2336

Bagchi, J., Durret, F., Neto, G. B. L., & Paul, S. 2006, Science, 314, 791

Beck, R. 1982, A&A, 106, 121

Beck, R. 2001, Space Science Reviews, 99, 243

Beck, R., & Krause, M. 2005, Astronomische Nachrichten, 326, 414

Beck, R., & Wielebinski, R. 2013, Planets, Stars and Stellar Systems. Volume 5: Galactic Structure and Stellar Populations, 641

Beck, R., Frick, P., Stepanov, R., & Sokoloff, D. 2012, A&A, 543, A113

Berrington, R. C., Lugger, P. M., & Cohn, H. N. 2002, AJ, 123, 2261

Bicknell, G. V., Cameron, R. A., & Gingold, R. A. 1990, ApJ, 357, 373

Blanton, E. L., Randall, S. W., Clarke, T. E., et al. 2011, ApJ, 737, 99

Blasi, P., & Colafrancesco, S. 1999, Astroparticle Physics, 12, 169

Brentjens, M. A. 2008, A&A, 489, 69

Brentjens, M. A., & de Bruyn, A. G. 2005, A&A, 441, 1217

Bridle, A. H., & Fomalont, E. B. 1976, A&A, 52, 107

Briel, U. G., Henry, J. P., Schwarz, R. A., et al. 1991, A&A, 246, L10

Bridle, A. H., Fomalont, E. B., Miley, G. K., & Valentijn, E. A. 1979, A&A, 80, 201

Brunetti, G. 2004, Journal of Korean Astronomical Society, 37, 493

Brunetti, G., Blasi, P., Cassano, R., & Gabici, S. 2004, MNRAS, 350, 1174

Brunetti, G., Cassano, R., Dolag, K., & Setti, G. 2009, A&A, 507, 661

Brunetti, G., Setti, G., Feretti, L., & Giovannini, G. 2001, MNRAS, 320, 365

Burn, B. J. 1966, MNRAS, 133, 67

Carilli, C. L., & Taylor, G. B. 2002, ARA&A, 40, 319

Cassano, R., & Brunetti, G. 2005, MNRAS, 357, 1313

Chen, Y., Reiprich, T. H., Böhringer, H., Ikebe, Y., & Zhang, Y.-Y. 2007, A&A, 466, 805

Cho, J., & Ryu, D. 2009, ApJL, 705, L90

Clarke, T. E., & Ensslin, T. A. 2006, AJ, 131, 2900

Dennison, B. 1980, ApJL, 239, L93

Dolag, K., & Enßlin, T. A. 2000, A&A, 362, 151

Dolag, K., Schindler, S., Govoni, F., & Feretti, L. 2001, A&A, 378, 777

Donnert, J., Dolag, K., Brunetti, G., & Cassano, R. 2013, MNRAS, 429, 3564

Dreher, J. W., Carilli, C. L., & Perley, R. A. 1987, ApJ, 316, 611

Ebeling, H., Edge, A. C., Bohringer, H., et al. 1998, MNRAS, 301, 881

Lueder, E. 2010, Liquid Crystal Displays: Addressing Schemes and Electro-Optical Effects, ISBN: 978-0-470-74519-9

Faber, S. M., & Dressler, A. 1977, AJ, 82, 187

Fabricant, D. G., Kent, S. M., & Kurtz, M. J. 1989, ApJ, 336, 77

Fabricant, D., Rybicki, G., & Gorenstein, P. 1984, ApJ, 286, 186

Felten, J. E. 1996, Clusters, Lensing, and the Future of the Universe, 88, 271

Ferrari, C., Intema, H. T., Orrù, E., et al. 2011, A&A, 534, L12

Feretti, L., Orrù, E., Brunetti, G., et al. 2004, A&A, 423, 111

Feretti, L., Giovannini, G., Govoni, F., & Murgia, M. 2012, A&ARv, 20, 54

Feretti, L., Dallacasa, D., Giovannini, G., & Tagliani, A. 1995, A&A, 302, 680

Ferrari, C., Govoni, F., Schindler, S., Bykov, A. M., & Rephaeli, Y. 2008, Space Science Reviews, 134, 93

Fujita, Y., Takizawa, M., & Sarazin, C. L. 2003, ApJ, 584, 190

Gardner, F. F., & Whiteoak, J. B. 1966, ARA&A, 4, 245

Giovannini, G., & Feretti, L. 2004, Journal of Korean Astronomical Society, 37, 323

Giovannini, G., Feretti, L., Venturi, T., Kim, K.-T., & Kronberg, P. P. 1993, ApJ, 406, 399

Gitti, M., Brunetti, G., & Setti, G. 2002, A&A, 386, 456

Govoni, F., & Feretti, L. 2004, International Journal of Modern Physics D, 13, 1549

Govoni, F., Dolag, K., Murgia, M., et al. 2010, A&A, 522, AA105

Govoni, F., Feretti, L., Giovannini, G., et al. 2001, A&A, 376, 803

Govoni, F., Murgia, M., Markevitch, M., et al. 2009, A&A, 499, 371

Govoni, F., Murgia, M., Xu, H., et al. 2013, A&A, 554, A102

Guidetti, D., Murgia, M., Govoni, F., et al. 2008, A&A, 483, 699

Haslam, C. G. T., Kronberg, P. P., Waldthausen, H., Wielebinski, R., & Schallwich, D. 1978, A&AS, 31, 99

Heald, G., Braun, R., & Edmonds, R. 2009, A&A, 503, 409

Hunter, D. A., Ficut-Vicas, D., Ashley, T., et al. 2012, AJ, 144, 134

Ideguchi, S., Takahashi, K., Akahori, T., Kumazaki, K., & Ryu, D. 2014, PASJ, 66, 5

Ideguchi, S., Tashiro, Y., Akahori, T., Takahashi, K., & Ryu, D. 2014, ApJ, 792, 51

Jaffe, W. 1980, ApJ, 241, 925

Kale, R., & Dwarakanath, K. S. 2010, ApJ, 718, 939

Keshet, U., & Loeb, A. 2010, ApJ, 722, 737

Kim, K.-T., Tribble, P. C., & Kronberg, P. P. 1991, ApJ, 379, 80

Kim, K.-T., Kronberg, P. P., Dewdney, P. E., & Landecker, T. L. 1990, ApJ, 355, 29

Large, M. I., Mathewson, D. S., & Haslam, C. G. T. 1959, Nature, 183, 1663

Lawler, J. M., & Dennison, B. 1982, ApJ, 252, 81

Le Roux, E. 1961, Annales d'Astrophysique, 24, 71

Meisenheimer, K., Roser, H.-J., Hiltner, P. R., et al. 1989, A&A, 219, 63

Miller, N. A., Owen, F. N., & Hill, J. M. 2003, AJ, 125, 2393

Murgia, M., Govoni, F., Feretti, L., et al. 2004, A&A, 424, 429

Ohno, H., Takizawa, M., & Shibata, S. 2002, ApJ, 577, 658

Orrú, E., Murgia, M., Feretti, L., et al. 2007, A&A, 467, 943

Owen, F. N. 1975, AJ, 80, 263

Owen, F. N., Rudnick, L., Eilek, J., et al. 2014, ApJ, 794, 24

Ozawa, T., Nakanishi, H., Akahori, T., et al. 2015, PASJ, 67, 110

Petrosian, V. 2001, ApJ, 557, 560

Perley, R. A., Chandler, C. J., Butler, B. J., & Wrobel, J. M. 2011, ApJL, 739, L1

Rich, J. W., de Blok, W. J. G., Cornwell, T. J., et al. 2008, AJ, 136, 2897

Roettiger, K., Burns, J. O., & Stone, J. M. 1999, ApJ, 518, 603

Rohlfs, K., & Wilson, T. L. 1996, Tools of Radio Astronomy, ISBN 3-540-60981-4

Rottgering, H., Snellen, I., Miley, G., et al. 1994, ApJ, 436, 654

Ryu, D., Kang, H., & Cho, J. 2010, Numerical Modeling of Space Plasma Flows, Astronum-2009, 429, 39

Ryu, D., Kang, H., Cho, J., & Das, S. 2008, Science, 320, 909

Sarazin, C. L. 2002, Merging Processes in Galaxy Clusters, 272, 1

Segalovitz, A., Shane, W. W., & de Bruyn, A. G. 1976, Nature, 264, 222

Skillman, S. W., Xu, H., Hallman, E. J., et al. 2013, ApJ, 765, 21

Sofue, Y., Fujimoto, M., & Wielebinski, R. 1986, ARA&A, 24, 459

Sokoloff, D. D., Bykov, A. A., Shukurov, A., et al. 1998, MNRAS, 299, 189

Stroe, A., Shimwell, T., Rumsey, C., et al. 2015, arXiv:1510.06739

Sun, M., Murray, S. S., Markevitch, M., & Vikhlinin, A. 2002, ApJ, 565, 867

Takizawa, M., & Naito, T. 2000, ApJ, 535, 586

Tamura, T., Hayashida, K., Ueda, S., & Nagai, M. 2011, PASJ, 63, 1009

Taylor, A. R., Stil, J. M., & Sunstrum, C. 2009, ApJ, 702, 1230

Taylor, G. B., Carilli, C. L., & Perley, R. A, 1999, SYNTHESIS IMAGING IN RADIO ASTRONOMY II, ISBN 1-58381-005-6

Thompson, A. R., Moran, J. M., & Swenson, G. W., Jr. 2001, Interferometry and Synthesis in Radio Astronomy, 2nd Edition, ISBN 978-0-471-25492-8

Trasatti, M., Akamatsu, H., Lovisari, L., et al. 2015, A&A, 575, A45

Tribble, P. C. 1991, MNRAS, 250, 726

Vacca, V., Feretti, L., Giovannini, G., et al. 2014, A&A, 561, A52

van Weeren, R. J., Röttgering, H. J. A., Intema, H. T., et al. 2012, A&A, 546, A124

van Weeren, R. J., Röttgering, H. J. A., Rafferty, D. A., et al. 2012, A&A, 543, A43

van Weeren, R. J., Röttgering, H. J. A., Brüggen, M., & Hoeft, M. 2010, Science, 330, 347

van Weeren, R. J., Brüggen, M., Röttgering, H. J. A., & Hoeft, M. 2011, MNRAS, 418, 230

van Weeren, R. J., Intema, H. T., Oonk, J. B. R., Röttgering, H. J. A., & Clarke, T. E. 2009, A&A, 508, 1269

Vazza, F., Brunetti, G., & Gheller, C. 2009, MNRAS, 395, 1333

Widrow, L. M. 2002, Reviews of Modern Physics, 74, 775

Willson, M. A. G. 1970, MNRAS, 151, 1

Xu, H., Li, H., Collins, D. C., Li, S., & Norman, M. L. 2009, ApJL, 698, L14

Xu, H., Li, H., Collins, D. C., Li, S., & Norman, M. L. 2010, ApJ, 725, 2152

Acknowledgements

鹿児島大学では３年間に渡り研究を行い多くの方に助けられました。以前所属していた明星大学には宇宙専門のコースというものはなかったため、これほど周りに天文学を行っている学生やスタッフがいるということは私にとって新鮮かつ非常に有意義なものでした。また SKA-JP 科学検討班宇宙磁場グループでは日本 SKA サイエンス会議「宇宙磁場」２０１５の会議の設営等多くの事を経験させていただきました。

指導教員の中西裕之准教授には深く感謝致します。今研究を続けることができているのも受け入れてくださったおかげです。研究のみならず多くのアドバイスを頂きました。また多くの迷惑をお掛けしたことをお詫び申し上げます。本研究と論文制作にあたり赤堀卓也特任准教授と山形大学の滝沢元和准教授、東京大学の祖父江義明名誉教授、明星大学の小野寺幸子准教授には多くの助力をいただきました。論文の出版が遅くなってしまったことをお詫びします。研究に関し半田利弘教授、今井宏准教授、新永浩子准教授からも多くの助言をいただきました。安楽健大様には AIPS の使い方やデータ解析のいろはを教えていただきました。SKA-JP のメンバーには観測提案提出に際し多くの助言をいただきました。同研究室の学生には暖かく接していただき、また解析マニュアル作成等を手伝っていただきました。関わった方全ての方に深く感謝致します。